



LAWRENCE
LIVERMORE
NATIONAL
LABORATORY

Neutron Interactions in the CUORE Neutrinoless Double Beta Decay Experiment

M. J. Dolinski

October 22, 2008

Disclaimer

This document was prepared as an account of work sponsored by an agency of the United States government. Neither the United States government nor Lawrence Livermore National Security, LLC, nor any of their employees makes any warranty, expressed or implied, or assumes any legal liability or responsibility for the accuracy, completeness, or usefulness of any information, apparatus, product, or process disclosed, or represents that its use would not infringe privately owned rights. Reference herein to any specific commercial product, process, or service by trade name, trademark, manufacturer, or otherwise does not necessarily constitute or imply its endorsement, recommendation, or favoring by the United States government or Lawrence Livermore National Security, LLC. The views and opinions of authors expressed herein do not necessarily state or reflect those of the United States government or Lawrence Livermore National Security, LLC, and shall not be used for advertising or product endorsement purposes.

This work performed under the auspices of the U.S. Department of Energy by Lawrence Livermore National Laboratory under Contract DE-AC52-07NA27344.

**Neutron Interactions in the CUORE Neutrinoless Double Beta Decay
Experiment**

by

Michelle Jean Dolinski

A.B. (Harvard University) 2003

A.M. (Harvard University) 2003

A dissertation submitted in partial satisfaction
of the requirements for the degree of

Doctor of Philosophy

in

Physics

in the

GRADUATE DIVISION

of the

UNIVERSITY OF CALIFORNIA, BERKELEY

Committee in charge:

Professor Eric Norman, Co-chair
Professor George Smoot, Co-chair
Professor Stuart Freedman
Professor Stanley Prussin

Fall 2008

This work was performed under the auspices of the U.S. Department of Energy by Lawrence Livermore National Laboratory in part under Contract W-7405-Eng-48 and in part under Contract DE-AC52-07NA27344.

This document was prepared as an account of work sponsored by an agency of the United States government. Neither the United States government nor Lawrence Livermore National Security, LLC, nor any of their employees makes any warranty, expressed or implied, or assumes any legal liability or responsibility for the accuracy, completeness, or usefulness of any information, apparatus, product, or process disclosed, or represents that its use would not infringe privately owned rights. Reference herein to any specific commercial product, process, or service by trade name, trademark, manufacturer, or otherwise does not necessarily constitute or imply its endorsement, recommendation, or favoring by the United States government or Lawrence Livermore National Security, LLC. The views and opinions of authors expressed herein do not necessarily state or reflect those of the United States government or Lawrence Livermore National Security, LLC, and shall not be used for advertising or product endorsement purposes.

Neutron Interactions in the CUORE Neutrinoless Double Beta Decay Experiment

Copyright © 2008

by

Michelle Jean Dolinski

Abstract

Neutron Interactions in the CUORE Neutrinoless Double Beta Decay Experiment

by

Michelle Jean Dolinski

Doctor of Philosophy in Physics

University of California, Berkeley

Professor Eric Norman, Co-chair

Professor George Smoot, Co-chair

Neutrinoless double beta decay ($0\nu\text{DBD}$) is a lepton-number violating process that can occur only for a massive Majorana neutrino. The search for $0\nu\text{DBD}$ is currently the only practical experimental way to determine whether neutrinos are identical to their own antiparticles (Majorana neutrinos) or have distinct particle and anti-particle states (Dirac neutrinos). In addition, the observation of $0\nu\text{DBD}$ can provide information about the absolute mass scale of the neutrino.

The Cuoricino experiment was a sensitive search for $0\nu\text{DBD}$, as well as a proof of principle for the next generation experiment, CUORE. CUORE will search for $0\nu\text{DBD}$ of ^{130}Te with a ton-scale array of unenriched TeO_2 bolometers. By increasing mass and decreasing the background for $0\nu\text{DBD}$, the half-life sensitivity of CUORE will be a factor of twenty better than that of Cuoricino. The site for both of these experiments is the Laboratori Nazionali del Gran Sasso, an underground laboratory with 3300 meters water equivalent rock overburden and a cosmic ray muon attenuation factor of 10^{-6} . Because of the extreme low background requirements for CUORE, it is important that all potential sources of background in the $0\nu\text{DBD}$ peak region at 2530 keV are well understood.

One potential source of background for CUORE comes from neutrons, which can be produced underground both by (α, n) reactions and by fast cosmic ray muon interactions. Preliminary simulations by the CUORE collaboration indicate that these backgrounds will be negligible for CUORE. However, in order to accurately simulate the expected neutron background, it is important to understand the cross sections for neutron interactions with detector materials. In order to help refine these simulations, I have measured the gamma-ray production cross sections for interactions of neutrons on the abundant stable isotopes of Te using the GEANIE detector array at the Los Alamos Neutron Science Center. In addition, I have used the GEANIE data to set an upper limit for the production of a 2529 keV gamma-ray from the $^{126}\text{Te}(n, n'\gamma)$ reaction. This gamma-ray is a potential source of interference for the $0\nu\text{DBD}$ peak. Based on this measurement, the contribution of this line to the background is expected to be negligible.

Professor Eric Norman
Dissertation Committee Co-chair

Professor George Smoot
Dissertation Committee Co-chair

To my parents

Contents

Contents	ii
List of Figures	iv
List of Tables	vii
Acknowledgements	viii
1 Introduction	1
2 Foundations of neutrino mass	4
2.1 Historical development of neutrino mass	4
2.2 Neutrino Oscillations	5
2.3 Majorana vs. Dirac	8
2.4 Double beta decay	9
3 The bolometric technique and the Cuoricino experiment	19
3.1 The bolometric approach	20
3.2 Choice of isotope	22
3.3 Cuoricino	23
4 The next-generation experiment: CUORE	32
4.1 Improving on the Cuoricino design	32
4.2 Background characterization	40
5 Measurement of neutron-induced backgrounds	44
5.1 Neutron-induced backgrounds underground	45
5.2 The Los Alamos Neutron Science Center	49

5.3	The GEANIE detector	50
5.4	The ^{130}Te and ^{nat}Te experiments	52
6	Analysis of GEANIE data	58
6.1	Raw data sorting	59
6.2	Analysis of the γ -ray spectra	59
6.3	The time-of-flight technique	61
6.4	Beam monitoring	64
6.5	Detector efficiencies and uncertainties	67
6.6	Cross sections	69
7	Conclusions	76
7.1	Cuoricino backgrounds	76
7.2	Implications for CUORE background	78
7.3	CUORE outlook	80
	Bibliography	81
A	The XGAM software package	88
A.1	Fitting functions	88
A.2	Extracting cross sections	90
B	Additional γ-ray production cross sections	104
B.1	^{130}Te excitations	104
B.2	^{128}Te excitations	104
B.3	^{126}Te excitations	111

List of Figures

2.1	The neutrino mass hierarchy.	7
2.2	Bottom of $A = 130$ mass parabolas.	9
2.3	2ν DBD.	10
2.4	0ν DBD through exchange of light Majorana neutrino.	11
2.5	Illustration from Schechter and Valle.	12
2.6	0ν DBD effective mass parameter space.	13
2.7	Summary of QRPA calculations of nuclear matrix elements.	14
2.8	Two-electron sum energy spectrum for double beta decay.	15
2.9	KKDC claim.	16
3.1	The Laboratori Nazionali del Gran Sasso.	19
3.2	Bolometer schematic.	21
3.3	A single Cuoricino pulse.	22
3.4	The most recent Cuoricino limit.	24
3.5	The Cuoricino tower.	25
3.6	NTD Ge thermistor T_0 vs. measured neutron fluence.	28
3.7	Cuoricino gain stabilization plot.	30
4.1	The CUORE detector.	33
4.2	The CUORE cryostat and shielding.	35
4.3	Electrical properties of NTD series NTD 33-38 and NTD 33B-35B.	36
4.4	Spectrum from the March 2008 NTD Ge NAA.	39
4.5	The half-life sensitivity of the CUORE experiment as a function of time for different background scenarios.	40
4.6	Spectrum from PTFE NAA.	42

5.1	Depth-sensitivity-relation for a Majorana-like experiment.	45
5.2	Simulated neutron flux.	46
5.3	CUORE geometry implemented for FLUKA.	48
5.4	Layout of the Los Alamos Neutron Science Center.	49
5.5	LANSCE neutron spectrum for the 60R beamline.	50
5.6	The GEANIE detector.	51
5.7	Angles and positions of the Ge detectors in GEANIE. Figure courtesy of the GEANIE collaboration.	53
5.8	Timing electronics for the GEANIE detector. Figure courtesy of the GEANIE collaboration.	54
5.9	Photographic plate images of beamspot.	56
5.10	Comparison of energy resolutions for different size beam spots.	57
6.1	GEANIE coax spectrum with Be target.	60
6.2	Fits to coaxial sum spectra for the Be and $^{130}\text{Te} + \text{Fe}$ runs.	62
6.3	Fits to coaxial sum spectra for the ^{130}Te and ^{nat}Te runs.	63
6.4	Time of flight spectrum for coax detectors.	64
6.5	γ -ray spectra for different neutron energies.	65
6.6	Fission chamber energy spectrum and time of flight spectra.	66
6.7	Measured total detector efficiencies.	68
6.8	$^{130}\text{Te}(n,2n)^{129}\text{Te}$ γ -ray production cross sections.	72
6.9	$^{130}\text{Te}(n,xn)$ cross sections.	72
6.10	$^{nat}\text{Te}(n,xn)$ cross sections.	73
6.11	2607 keV $^{130}\text{Te}(n,n'\gamma)$ γ -ray production cross section.	73
6.12	646.1 keV $^{130}\text{Te}(n,\alpha)^{127}\text{Sn}$ γ -ray production cross section.	74
6.13	Search for $^{126}\text{Te}(n,n'\gamma)$ line at 2529 keV.	75
7.1	Search for evidence of inelastic neutron scattering in Cuoricino Run I data.	77
7.2	Search for coincident events in Cuoricino data.	78
A.1	^{nat}Te coaxial sum spectrum with fit.	91
A.2	^{nat}Te coaxial sum spectrum with fit.	92
A.3	^{nat}Te coaxial sum spectrum with fit.	93
A.4	^{nat}Te coaxial sum spectrum with fit.	94
A.5	^{nat}Te coaxial sum spectrum with fit.	95

A.6	^{nat}Te coaxial sum spectrum with fit.	96
A.7	^{nat}Te coaxial sum spectrum with fit.	97
A.8	^{nat}Te coaxial sum spectrum with fit.	98
A.9	^{nat}Te coaxial sum spectrum with fit.	99
A.10	^{nat}Te coaxial sum spectrum with fit.	100
A.11	^{nat}Te coaxial sum spectrum with fit.	101
A.12	^{nat}Te coaxial sum spectrum with fit.	102
B.1	Cross section for the 468 keV transition in ^{130}Te	105
B.2	Cross section for the 550 keV transition in ^{130}Te	105
B.3	Cross section for the 748 keV transition in ^{130}Te	106
B.4	Cross section for the 793 keV transition in ^{130}Te	106
B.5	Cross section for the 942 keV transition in ^{130}Te	107
B.6	Cross section for the 1046 keV transition in ^{130}Te	107
B.7	Cross section for the 1142 keV transition in ^{130}Te	108
B.8	Cross section for the 1299 keV transition in ^{130}Te	108
B.9	Cross section for the 1443 keV transition in ^{130}Te	109
B.10	Cross section for the 776 keV transition in ^{128}Te	109
B.11	Cross section for the 1225 keV transition in ^{128}Te	110
B.12	Cross section for the 1284 keV transition in ^{128}Te	110
B.13	Cross section for the 651 keV transition in ^{126}Te	111
B.14	Cross section for the 1346 keV transition in ^{126}Te	112

List of Tables

2.1	Properties of several commonly studied 0ν DBD candidate isotopes.	10
2.2	Summary of next generation 0ν DBD experiments.	18
3.1	Calculation of $m_{\beta\beta}$ for $T_{1/2}^{0\nu\beta\beta}(^{130}\text{Te}) > 3.0 \times 10^{24}$ years (90% confidence level) using selected nuclear matrix elements.	24
4.1	Technical specifications for cooling power of pulse tube refrigerators and dilution unit as a function of temperature.	34
4.2	Summary of sample properties and results from the December 2007 NAA.	39
4.3	Summary of sample properties and results from March 2008 NAA.	39
4.4	CUORE 5-year sensitivity to the 0ν DBD half-life of ^{130}Te	40
5.1	Transitions in Te at the 0ν DBD region of interest.	47
5.2	Experimental details for the ^{130}Te target.	55
5.3	Natural isotopic abundance of Te.	55
5.4	Experimental details for the unenriched Te target.	57
6.1	Inelastic scattering peaks on the stable Ge isotopes.	61
6.2	Photon attenuation factors.	69
6.3	Q-values and thresholds for some $^{130}\text{Te} + n$ products.	70
6.4	Q-values and thresholds for some $^{128}\text{Te} + n$ products.	71
6.5	Q-values and thresholds for some $^{126}\text{Te} + n$ products.	71
6.6	2529 keV peak area limit.	74
A.1	Peakshape parameters for ^{130}Te fit.	90
A.2	Peakshape parameters for ^{nat}Te fit.	103

Acknowledgements

First and foremost I have to thank my research advisor, Professor Eric B. Norman, for all of his guidance and support during my graduate career. I feel extremely lucky and privileged to have worked with such a wonderful advisor. My thanks to the Lawrence Livermore National Laboratory for the SEGRF/LSP fellowship program, which allowed me to continue working with Professor Norman on CUORE.

My graduate career has been enriched further through the involvement of my academic advisor, Professor George Smoot. He has always been there to offer advice and encouragement. I would also like to thank Professor Stan Prussin and Professor Stuart Freedman for giving their valuable time to be on my thesis committee.

I would like to acknowledge my many collaborators, without whom I would have very little to show for myself. I would like to thank the members of the Cuoricino and CUORE collaborations, and in particular Professor Ettore Fiorini. My sincerest thanks to Carlo Bucci, Paolo Gorla, and Stefano Pirro at LNGS, for putting up with my frequent visits. I would also like to thank Iulian Bandac for always helping me out when I found myself stranded in Italy without a place to sleep. My thanks to Fabio Bellini and Silvia Capelli for sharing their work on neutron simulations. My warmest regards to all of my Cuoricino and CUORE collaborators, who have made my time in Italy and in the collaboration an absolute pleasure.

Closer to home, my deepest thanks to Al Smith for teaching me about low background counting, among many other things. I have to thank Thomas Gutierrez and Reina Maruyama for being excellent postdocs (and examples). I would also like to acknowledge my fellow Berkeley graduate students in the neutrino office, Lindley Winslow, Tommy O'Donnell, Laura Kogler, and Adam Bryant. Thank you for making my time at LBL so enjoyable.

I have also had many collaborators on the experiments at GEANIE. I would like to thank Ron Nelson, Nick Fotiades, and Matt Devlin for their collaboration and support, both at LANSCE and afterward. I would also like to acknowledge the work of the staff

of LANSCE for making my experiment at GEANIE possible. My thanks to Dugarsuren Dashdorj, who walked this path before me and who offered guidance along the way. Finally, I would like to recognize the wisdom and infinite patience of Walid Younes, without whose assistance my graduate career could easily have extended into the next decade.

At Berkeley, I would like to thank the rest of the excellent physics faculty, my graduate student colleagues, SWPS, and our wonderful support staff (especially Anne Takizawa and Donna Sakima) for making my graduate school experience everything I hoped it would be.

Finally, I would like to thank my family for their love and understanding during my long years of schooling. Mom, you were always there for me, showing me the way to work hard for what I wanted, and to enjoy myself along the way. I know that my father would be prouder than anyone if he could see me now. Finally, my thanks to Kenneth Jensen, for his presence in my life and for his love, but most certainly not for his help.

Chapter 1

Introduction

Today, more than fifty years after the discovery of the neutrino at Savannah River by Reines and Cowan [1], we are entering the era of precision neutrino physics. Neutrino oscillations have given us a powerful tool for extracting neutrino mixing parameters, but questions remain. Neutrino oscillation experiments cannot determine the absolute masses of the neutrinos, nor can they distinguish between Majorana neutrinos, identical to their own anti-particles, and Dirac neutrinos with distinct particle and anti-particle states. However, neutrinoless double beta decay ($0\nu\text{DBD}$) can address both of these issues. The search for $0\nu\text{DBD}$ is an important experimental technique for understanding the inclusion of the massive neutrino in the Standard Model of Particle Physics.

Double beta decay is a rare nuclear process that can occur in certain even-even nuclei. It is the dominant decay mode when the single beta decay is energetically forbidden. Two-neutrino double beta decay ($2\nu\text{DBD}$) is allowed by the Standard Model and has been observed in the laboratory for several isotopes. In the Standard Model, which does not include a neutrino mass term, $0\nu\text{DBD}$ is a forbidden decay. However, for a massive Majorana neutrino, the decay is allowed. The observation of neutrino oscillations has proven that neutrinos are, in fact, massive particles with mass eigenstates distinct from the weak interaction eigenstates. The existence of neutrino mass has renewed interest in the search for $0\nu\text{DBD}$ over the last twenty years. The observation of $0\nu\text{DBD}$ would prove that neutrinos

are Majorana particles as well as provide valuable information about the absolute scale of neutrino mass.

The double beta decay signal lies in the 2-electron summed energy spectrum. For 2ν DBD, the neutrinos carry away some of the energy, so the 2-electron spectrum is a continuum from 0 to the Q-value of the decay. However, for 0ν DBD the electrons must carry the full energy, giving a peak located at the Q-value, also referred to as the 0ν DBD region of interest. For a detector with poor energy resolution, the 2ν DBD gives an irreducible contribution to the background for observation of 0ν DBD.

The Cuoricino experiment, which searched for the 0ν DBD of ^{130}Te using an array of unenriched TeO_2 bolometers, took data at the underground Laboratori Nazionali del Gran Sasso (LNGS) from 2003 to 2008. The Cuoricino experiment achieved a background in the 0ν DBD region of interest at 2530 keV of 0.18 ± 0.01 counts/keV/kg/yr. The current published limit on the half-life of 0ν DBD of ^{130}Te from this experiment is $T_{1/2}^{0\nu\beta\beta} > 3.0 \times 10^{24}$ yr [2]. The CUORE experiment, one of the next generation of 0ν DBD experiments, is the next step in the evolution of bolometric 0ν DBD detectors. With larger mass and improved background, the half-life sensitivity of the CUORE experiment will be a factor of twenty better than Cuoricino. Other next generation experiments include searches for the 0ν DBD of ^{76}Ge (GERDA, Majorana) and ^{136}Xe (XMASS, EXO), among others.

For the next generation of 0ν DBD experiments, background characterization and reduction present significant challenges. As next generation searches for 0ν DBD push the boundaries of low background techniques, increasingly rare processes become important sources of background. A combination of approaches is necessary to make these stringent background goals a reality. Primary methods include siting experiments in deep underground laboratories, shielding active detector components from environmental radioactivity, screening materials to achieve low radioactive contamination, careful prevention of recontamination with Rn daughters, and active rejection of background events. In order to create a suitably low background with limited resources, it is important to be able to make models that can accurately predict the contributions to the background from different sources.

One area in which the contribution to the background has a great deal of uncertainty is background events caused by neutrons. Low energy neutrons can be produced through radioactive decays occurring locally in the laboratory, while higher energy neutrons can result from interactions of fast through-going cosmic ray muons. The contribution of neutron-induced backgrounds for next generation $0\nu\text{DBD}$ has been studied by members of the Majorana collaboration [3], leading to the conclusion that muon-induced neutrons can be a significant source of background for Ge-based next generation $0\nu\text{DBD}$ experiments. This is an important question that should be addressed on a detector by detector basis, in order to properly account for different aspects of detector shielding and anti-coincidence capabilities. One major problem with these studies is the uncertainty in the high energy neutron flux at underground laboratories. In addition, the gamma-ray production cross sections for high energy neutrons on the relevant materials are not well known. My work on the measurement of neutron-induced cross sections on Te isotopes for the CUORE experiment will help to refine the simulation codes used to predict the expected background for the CUORE detector.

Using the Germanium Array for Neutron Induced Excitations (GEANIE) at Los Alamos Neutron Science Center (LANSCE), my collaborators and I were able to measure the cross-sections for $\text{Te} + \text{n}$ reactions for neutron energies in the range of 1 - 200 MeV. In particular, we searched for gamma-rays produced by these neutron reactions which could give a false signal in the ^{130}Te $0\nu\text{DBD}$ region of interest at 2530 keV. The cross sections, which were measured at these energies for the first time for many of the transitions studied, can be included in the Monte Carlo codes to better predict backgrounds in the CUORE detector. My analysis shows that neutron-induced background peaks in the $0\nu\text{DBD}$ region of interest are not expected to be a significant source of background for $0\nu\text{DBD}$ in the CUORE detector.

Chapter 2

Foundations of neutrino mass

In the Standard Model of particle physics, neutrinos are massless particles. However, with the observation of neutrino oscillations, we now know that neutrinos have mass, and furthermore that the mass eigenstates and weak interaction flavor states are not identical. It is this misalignment of flavor and mass that causes neutrino oscillations. Neutrino mass has implications for other phenomena as well, including $0\nu\text{DBD}$, a process which is forbidden for a massless neutrino. In this chapter, I will discuss the historical development and theory of neutrino mass, leading up to the current experimental program in $0\nu\text{DBD}$.

2.1 Historical development of neutrino mass

Prior to 1930, the observed β -decay spectrum was causing a crisis in nuclear physics. Unlike the discrete α -decay and γ -ray emission spectra, the β -decay spectrum was known to be a continuum, seeming to violate the law of conservation of energy. In a letter dated December 1, 1930, Wolfgang Pauli proposed an elegant solution to the problem. He introduced a particle, which he called the “neutron,” which was invisible in the detectors of the day but which could carry away some of the beta decay energy. He suggested that the mass of this particle “in any case could not be greater than 0.01 proton masses” [4]. Later, Enrico Fermi developed the theory of β -decay and renamed this particle the neutrino.

The neutrino was not observed experimentally until 1956, when Reines and Cowan detected the first electron antineutrinos at Savannah River [1]. The muon neutrino was discovered in 1962 by a group at Columbia University using the first neutrino beam [5]. The tau neutrino was not discovered until 2000, when the DONUT collaboration confirmed the observation of four tau neutrino events using photographic emulsions to observe the 1 mm long tracks of the τ leptons produced [6]. In the Standard Model, all three flavors of neutrinos are defined to be massless particles. The discovery of neutrino oscillations has shown that neutrinos are, in fact, massive particles, opening up a rich field of research into physics extending beyond the Standard Model.

2.2 Neutrino Oscillations

The first indication of neutrino oscillations came from the chlorine solar neutrino experiment conducted by Raymond Davis, Jr., in the Homestake mine in South Dakota [7]. This experiment observed only one third of the flux of neutrinos from the sun predicted by the Standard Solar Model (SSM). The “solar neutrino problem,” as it came to be known, was bolstered by the findings of the gallium experiments, GALLEX [8] and SAGE [9], which also observed a deficit of neutrinos from the sun with a lower energy threshold. Finally, the SNO experiment confirmed that electron neutrinos were being converted into other neutrino flavors through the comparison of charged current reactions (sensitive only to ν_e) to neutral current reactions (sensitive to all three neutrino flavors) [10].

In addition to solar neutrinos, an anomaly in the atmospheric neutrino flux was observed by Super-Kamiokande [11]. In this experiment, designed to search for proton decay in a large volume of water, atmospheric neutrinos could be observed by the Čerenkov light produced through scattering in the detector. The observations were observed as the difference between the flux of downward-going and upward-going ν_μ events. The explanation for this observation is that the ν_μ s were oscillating into ν_τ s. Neutrino oscillations (as opposed to other mechanisms such as neutrino decay) seemed to explain all of the observed phenomena.

Finally, in 2002, the KamLAND collaboration published the first observation of the

oscillation effect [12]. In combination with the other experimental data, the KamLAND data clearly favored the large mixing angle MSW solution to the solar neutrino problem. In this scenario, the solar mixing angle is large, and interactions between solar neutrinos and the matter in the sun (the Mikheyev-Smirnov-Wolfenstein effect) play an important role. The most recent publication from KamLAND clearly shows the expected oscillatory behavior for the $\bar{\nu}_e$ flux [13].

Neutrino oscillations occur because the neutrino weak flavor eigenstates (ν_e , ν_μ , and ν_τ) are not aligned with the neutrino mass eigenstates (m_1 , m_2 , and m_3). The flavor eigenstates are described as superpositions of the mass eigenstates by equation 2.1 [14].

$$|\nu_\alpha\rangle = \sum_j U_{\alpha j}^* |\nu_j\rangle. \quad (2.1)$$

The neutrino mixing matrix $U_{\alpha j}$ is given by equation 2.2 [14].

$$U_{\alpha j} = \begin{pmatrix} c_{12}c_{13} & s_{12}c_{13} & s_{13}e^{-i\delta} \\ -s_{12}c_{23} - c_{12}s_{23}s_{13}e^{i\delta} & c_{12}c_{23} - s_{12}s_{23}s_{13}e^{i\delta} & s_{23}c_{13} \\ s_{12}s_{23} - c_{12}c_{23}s_{13}e^{i\delta} & -c_{12}s_{23} - s_{12}c_{23}s_{13}e^{i\delta} & c_{23}c_{13} \end{pmatrix} \times \begin{pmatrix} e^{i\alpha_1/2} & 0 & 0 \\ 0 & e^{i\alpha_2/2} & 0 \\ 0 & 0 & 1 \end{pmatrix}, \quad (2.2)$$

where s_{12} and c_{12} indicate $\sin\theta_{12}$ and $\cos\theta_{12}$, for example. The angles θ_{12} , θ_{23} , and θ_{13} are known as the mixing angles, and the parameter δ is a phase which can violate charge conjugation and parity (CP) symmetries. In addition, the parameters ξ_1 and ξ_2 are Majorana phases. These phases can also violate CP, but they are not observable in neutrino oscillations.

Considering two-neutrino mixing only (a good approximation when the charged lepton interaction under study couples significantly to only two neutrino mass eigenstates), we arrive at the equation for oscillation probability in vacuum [14]:

$$P(\nu_\alpha \rightarrow \nu_\beta) = \sin^2 2\theta \sin^2 \left(1.27 \times \Delta m^2 \frac{L}{E} \right), \quad (2.3)$$

when $\alpha \neq \beta$, and:

$$P(\nu_\alpha \rightarrow \nu_\alpha) = 1 - \sin^2 2\theta \sin^2 \left(1.27 \times \Delta m^2 \frac{L}{E} \right), \quad (2.4)$$

where Δm^2 is the mass-squared difference in the neutrino mass eigenstates measured in eV^2 , L is the distance measured in km, and E is the neutrino energy measured in GeV. As

this equation clearly shows, neutrino oscillation experiments can extract the Δm^2 , but not the absolute masses of the neutrino mass eigenstates.

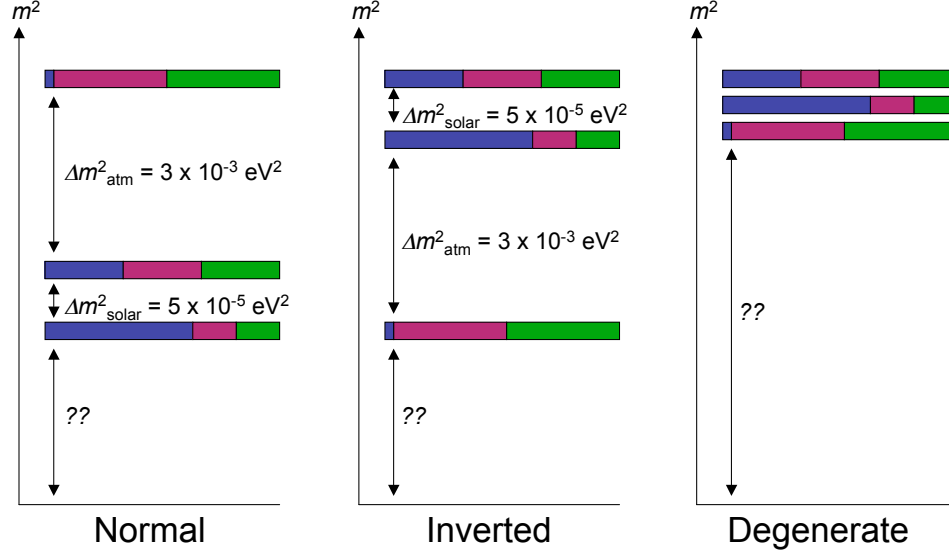


Figure 2.1. Illustration of the current state of neutrino mass and mixing measurements, where the colors represent the flavor eigenstates (blue = ν_e , magenta = ν_μ , and green = ν_τ). Δm^2_{atm} and $\Delta m^2_{\text{solar}}$ are the mass-squared differences extracted from measurements of atmospheric neutrino oscillations and solar/reactor neutrino oscillations, respectively. The three versions of the neutrino hierarchy, normal, inverted, and degenerate, are shown.

Although we have been able to measure the neutrino mass-squared difference and two out of three mixing angles, many questions remain unanswered. The status of neutrino mass measurements is summarized in figure 2.1. There exists only an upper bound on the third mixing angle, θ_{13} . We still do not know the absolute values of the three neutrino masses. In addition, we do not know the ordering of the masses. The neutrino mass hierarchy could be normal, following the pattern of the charged leptons, or it could be inverted, in which case the solar pair is much heavier than the third mass state. Finally, we have a degenerate case, in which the absolute mass scale is large compared to the mass splittings. In addition, the quantum nature of the neutrino is an experimentally open question. I will explore these questions further in the following sections.

There are two major experimental efforts to determine the neutrino mass. One method

is a careful study of the endpoint of the beta decay spectrum, where the finite mass of the neutrino modifies the shape of the spectrum. Traditionally, the isotope of choice for these studies is tritium (^3H), with a Q-value of 18.59 keV and a half-life of 12.33 years. The upcoming KATRIN experiment is at the forefront of this field. KATRIN is a large magnetic spectrometer, and the projected three year neutrino mass sensitivity is 0.2 eV [15]. The MARE collaboration is also investigating a bolometric experiment to study the endpoint of the ^{187}Re beta decay spectrum, at 2.47 keV, with sensitivity comparable to KATRIN [16]. The other method is the search for neutrinoless double beta decay ($0\nu\text{DBD}$), which will be discussed in section 2.4.

2.3 Majorana vs. Dirac

For a massless neutrino, the question of whether the particle is a Dirac particle with distinct particle and antiparticle states or a Majorana particle is irrelevant. Once it was determined that the neutrino has mass, the question of the quantum nature of the neutrino became an open experimental question. This answer determines how the neutrino mass is included in the Standard Model. The mass can be included as a Dirac mass term, given in equation 2.5 [14]:

$$\mathcal{L}_{Dirac} = -m_D \bar{\nu}_L \nu_R + h.c., \quad (2.5)$$

where m_D is a constant, the Dirac mass. The Dirac mass term couples the left-handed and right-handed neutrino. However, once the right-handed neutrino is introduced, there is no reason not to include a Majorana mass term as well, where the neutrino is coupled to its charge conjugate:

$$\mathcal{L}_{Majorana} = -m_R \bar{\nu}_R^c \nu_R + h.c., \quad (2.6)$$

where m_R is the Majorana mass and ν_R^c is the charge conjugate of ν_R . While both Majorana and Dirac mass terms are not excluded by any symmetry arguments, it is natural to ask the question of why the neutrino is so much lighter than the other fermions in the Standard Model.

It is an open experimental question whether neutrinos are Majorana particles or Dirac

particles. However, the fact that neutrino masses are orders of magnitude smaller than the charged leptons suggests that a different mechanism may be responsible for generating neutrino mass. The Seesaw mechanism, which results in a Majorana mass term, provides a compelling mechanism for generating matter-antimatter asymmetry [17]. In the Seesaw mechanism, a heavy right-handed partner of the neutrino suppresses neutrino mass. With CP and B-L (baryon number minus lepton number) violation, heavy partners can decay in such a way as to produce a lepton number asymmetry, which is then converted into a baryon asymmetry. Currently, the only practical experimental method for determining the quantum nature of the neutrino is the search for $0\nu\text{DBD}$.

2.4 Double beta decay

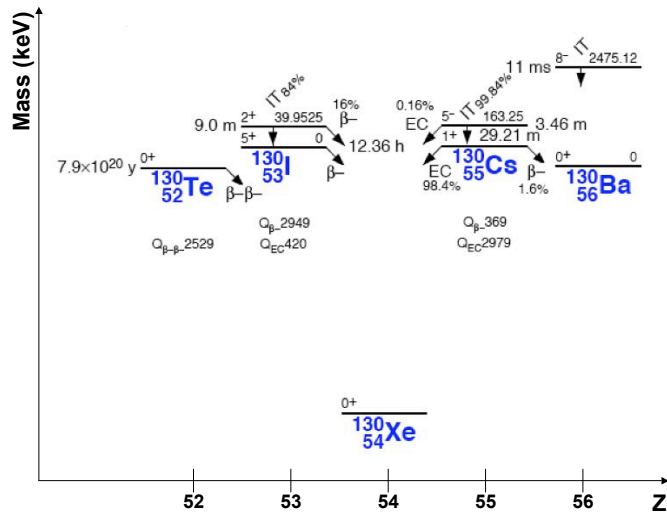


Figure 2.2. $A = 130$ mass parabolas, illustrating the forbidden β^- decay of ^{130}Te to ^{130}I .

Double beta decay is a second-order weak process. It occurs for some even-even nuclei for which the single beta decay is energetically forbidden, or suppressed by large change in angular momentum (see figure 2.2). Double beta decay accompanied by two neutrinos ($2\nu\text{DBD}$) - see figure 2.3 - is allowed in the Standard Model, and was first observed in ^{82}Se in 1987 [18]. $2\nu\text{DBD}$ is a rare process, with half-lives typically on the order of $> 10^{18}$ years.

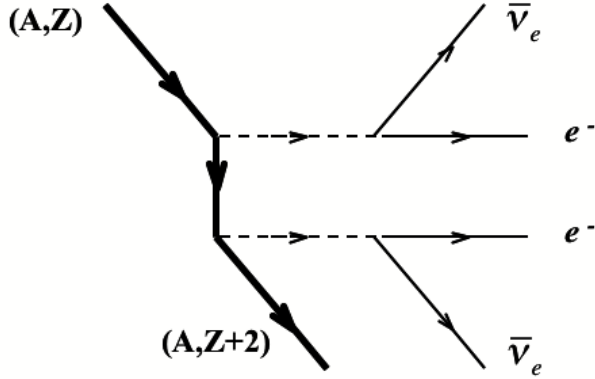


Figure 2.3. Double beta decay with the emission of 2 neutrinos.

Table 2.1. Properties of several commonly studied 0ν DBD candidate isotopes. Except where noted, values were obtained from the National Nuclear Data Center at Brookhaven National Laboratory [20]. The claim for ^{76}Ge 0ν DBD will be discussed further in section 2.4.2.

Isotope	Iso. abund.	Q-value (keV)	$T_{1/2}^{2\nu\beta\beta}$ (yr)	$T_{1/2}^{0\nu\beta\beta}$ (yr)
^{48}Ca	0.187%	4273.60	$(4.3 \pm 2.3) \times 10^{19}$	$> 1.4 \times 10^{22}$ [21]
^{76}Ge	7.83%	2039.00	$(1.3 \pm 0.4) \times 10^{21}$	1.19×10^{25} [22]
^{82}Se	8.73%	2995.50	$(9.2 \pm 0.8) \times 10^{19}$	$> 1 \times 10^{23}$ [23]
^{96}Zr	2.80%	3347.70	$(2.0 \pm 0.4) \times 10^{19}$	$> 1.0 \times 10^{21}$ [24]
^{100}Mo	9.63%	3034.68	$(7.0 \pm 0.4) \times 10^{18}$	$> 4.6 \times 10^{23}$ [23]
^{116}Cd	7.49%	2808.71	$(3.0 \pm 0.3) \times 10^{19}$	$> 1.7 \times 10^{23}$ [25]
^{130}Te	33.80% [26]	2530.30	$(6.1 \pm 4.8) \times 10^{20}$	$> 3.0 \times 10^{24}$ [2]
^{136}Xe	8.857%	2461.80	$> 1.0 \times 10^{22}$ [27]	$> 1.2 \times 10^{24}$ [27]
^{150}Nd	5.6%	3367.68	$(7.9 \pm 0.7) \times 10^{18}$	$> 1.7 \times 10^{21}$ [28]

The rate for 2ν DBD is given in equation 2.7 [19]:

$$[T_{1/2}^{2\nu\beta\beta}]^{-1} = G^{2\nu} |M^{2\nu}|^2, \quad (2.7)$$

where $G^{2\nu}$ is an exactly calculable phase space factor proportional to the reaction Q-value raised to the eleventh power and $M^{2\nu}$ is the nuclear matrix element for 2ν DBD. Some commonly studied DBD isotopes, along with their natural isotopic abundances, Q-values, and measured half-lives, are shown in table 2.1.

0ν DBD is a lepton-number violating decay forbidden in the Standard Model. One possible mechanism for 0ν DBD is the exchange of a massive Majorana neutrino, shown in figure 2.4. The exchange of a massive Majorana neutrino is not the only mechanism that will produce a lepton violating double beta decay. However, the observation of neutrinoless

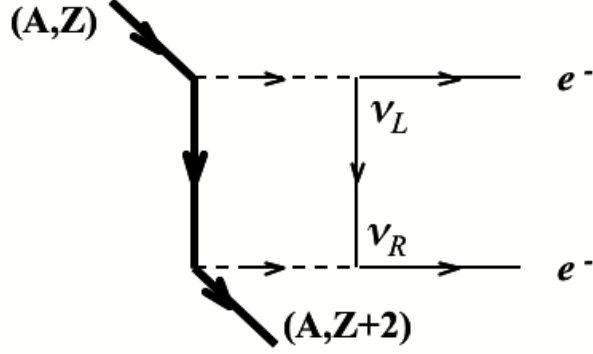


Figure 2.4. $0\nu\text{DBD}$ through exchange of light Majorana neutrino.

double beta decay does imply the existence of a Majorana mass term. The argument, set forth by Schechter and Valle [29], is shown in figure 2.5. As the figure shows, the $0\nu\text{DBD}$ reaction can be inverted to produce a $\bar{\nu}_e$ going into a ν_e , or in other words, a Majorana mass term. Without knowing the actual mechanism for $0\nu\text{DBD}$, it is impossible to extract the neutrino mass from the measurement of the $0\nu\text{DBD}$ rate. Exotic mechanisms include the exchange of a heavy neutrino, right handed weak interaction currents, or even the exchange of supersymmetric particles.

The mechanism which provides the most direct measurement of the effective Majorana mass is the exchange of a light Majorana neutrino. In this case, the rate of $0\nu\text{DBD}$ is given by equation 2.8 [19]:

$$[T_{1/2}^{0\nu\beta\beta}]^{-1} = G^{0\nu} |M^{0\nu}|^2 \langle m_{\beta\beta} \rangle^2, \quad (2.8)$$

where $G^{0\nu}$ is an exactly calculable phase space factor proportional to the Q-value raised to the fifth power, $M^{0\nu}$ is the nuclear matrix element for $0\nu\text{DBD}$, discussed further in section 2.4.1, and $\langle m_{\beta\beta} \rangle$ is the effective Majorana neutrino mass, given in equation 2.9 [19]:

$$|\langle m_{\beta\beta} \rangle| \equiv \left| \sum_i m_i U_{ei}^2 \right|, \quad (2.9)$$

where the m_i are the three neutrino masses and the U_{ei} are the elements of the mixing matrix U coupling the mass states to the ν_e flavor eigenstate. Inserting the measured neutrino mass and mixing parameters obtained from oscillation measurements, we obtain the allowed parameter space for $m_{\beta\beta}$ as a function of the minimum neutrino mass, shown

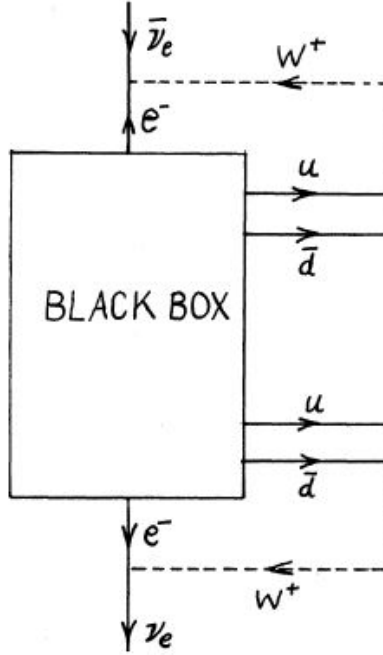


Figure 2.5. Illustration from Schechter and Valle [29], showing the conversion of $\bar{\nu}_e$ to ν_e by a $0\nu\text{DBD}$ interaction. The existence of this diagram proves that $0\nu\text{DBD}$ implies a Majorana mass for the neutrino, even if light neutrino exchange is not the dominant mechanism.

in figure 2.6. Assuming that neutrinos have a Majorana mass, and that light Majorana neutrino exchange is the dominant mechanism, searches for $0\nu\text{DBD}$ are complementary to other efforts to measure the neutrino mass.

2.4.1 Nuclear matrix elements

In equation 2.8, the rate for the $0\nu\text{DBD}$ is shown to be proportional to the square of the nuclear matrix element for $0\nu\text{DBD}$. The matrix elements are relevant only for the $0\nu\text{DBD}$ process, and therefore cannot be independently determined by experiment. Instead, they must be calculated from nuclear theory in order to extract a measurement of $m_{\beta\beta}$ from the observed half-life for $0\nu\text{DBD}$. The matrix elements depend on the nuclear structure of the parent and daughter nuclei, as well as the intermediate nucleus (^{130}I in the case of ^{130}Te DBD). There are several different methods for calculating nuclear matrix elements. For

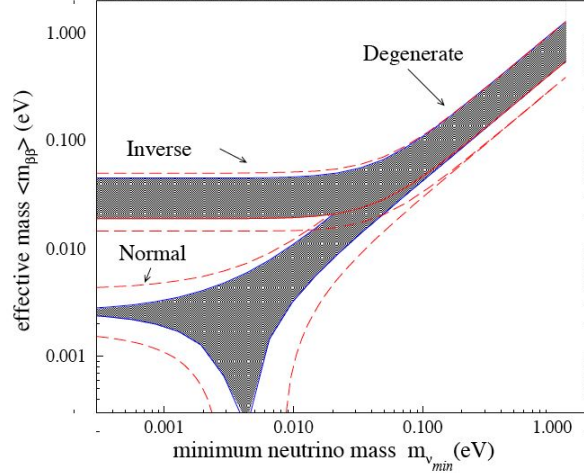


Figure 2.6. The parameter space for $m_{\beta\beta}$ as a function of the minimum neutrino mass. The shaded area is for central values for neutrino mixing parameters (including $\theta_{13} = 0$). The dashed lines indicate 1σ errors on neutrino mixing parameters [30].

a more extensive discussion of nuclear matrix element calculations, see the 2002 review of double beta decay by Elliott and Vogel [31].

One method for calculating nuclear matrix elements is the nuclear shell model (NSM). In this model, interactions are described by an effective Hamiltonian. The effective Hamiltonian is then diagonalized over all configurations of a chosen subset of valence single-particle states. NSM calculations are computationally intensive, which places a practical limit on the number of single-particle states that can be considered.

Another method for calculating nuclear matrix elements is the quasi-random phase approximation (QRPA). In this method, modeled on calculations done in solid state physics, a large valence space is used to do computations, but the interactions are parametrized. This method is good for predicting collective excitations in nuclei. Recently, a group has been using 2ν DBD nuclear matrix elements to fix some parameters for the 0ν DBD matrix element calculations [32]. This method has led to a stabilization of the matrix elements $M^{0\nu}$, and now the shell model calculations and QRPA calculations lie within a factor of two of each other. Figure 2.7 shows the dependence of nuclear matrix element calculations for various 0ν DBD isotopes on the QRPA calculation parameters. See section 3.3 for a

summary of how nuclear matrix elements impact the calculation of $m_{\beta\beta}$ from the $0\nu\text{DBD}$ half-life limit of ^{130}Te .

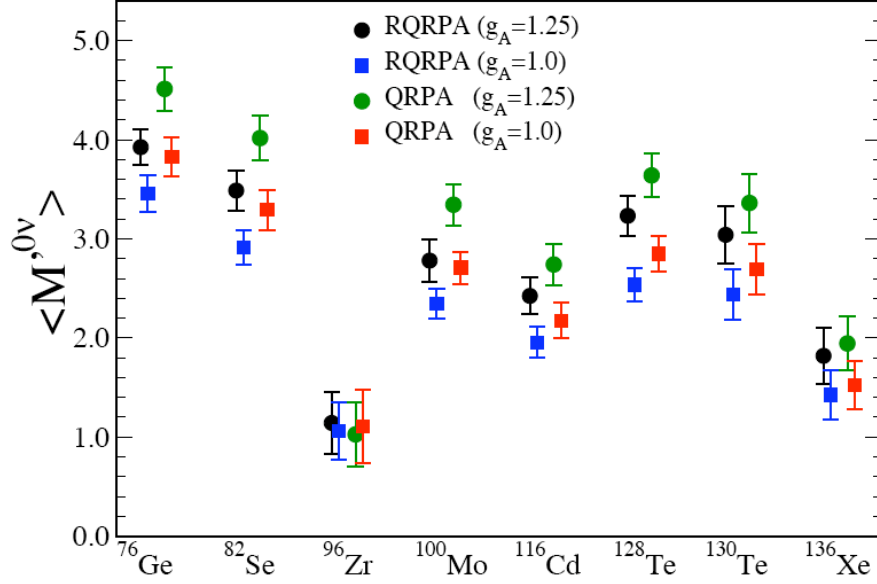


Figure 2.7. Nuclear matrix element calculations for several $0\nu\text{DBD}$ candidate isotopes using QRPA. From Rodin, et. al. [32].

2.4.2 Experimental searches for $0\nu\text{DBD}$

In general, $0\nu\text{DBD}$ can be identified as a peak in the total energy spectrum in the detector. In $2\nu\text{DBD}$, the two neutrinos carry away part of the energy, and the total energy of the two β particles is a continuum extending to the Q-value of the decay. For $0\nu\text{DBD}$, the total energy of the two β -particles is simply a peak at the Q-value (see figure 2.8). In order to achieve the minimum background possible, many $0\nu\text{DBD}$ experiments adopt the “source equals detector” approach, in which a significant fraction of the detector material is made up of the isotope of interest. For detectors that exploit the source equals detector configuration, the sensitivity to the $0\nu\text{DBD}$ half-life in years is given by the figure of merit F_D [33]:

$$F_D = 4.17 \times 10^{26} \left(\frac{f}{A} \right) \sqrt{\frac{Mt}{B\Gamma}} \epsilon \quad (2.10)$$

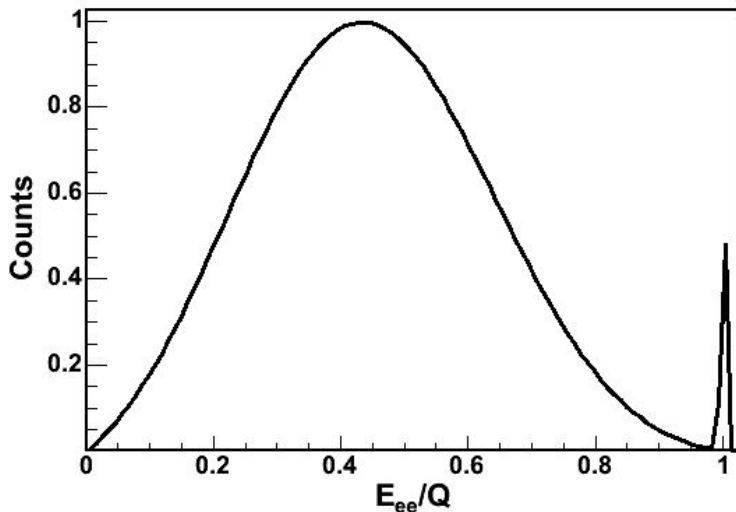


Figure 2.8. Cartoon illustration of the relationship between 2ν DBD (continuum) and 0ν DBD (peak) spectra. The relative rate of 0ν DBD to 2ν DBD is highly exaggerated.

where f is the fractional abundance of the source isotope, A is the atomic mass in kg, M is the total mass of source isotope in kg, t is the counting time in years, B is the background rate in counts/keV/kg/yr, Γ is the detector resolution in keV, and ϵ is the efficiency of the detector for detection of double beta decay. Some examples of this type of detector include enriched ^{76}Ge diodes (IGEX, Heidelberg-Moscow, Majorana, GERDA), an enriched liquid ^{136}Xe time projection chamber (EXO), and the TeO_2 bolometers used in CUORE.

A partial list of existing 0ν DBD limits is shown in table 2.1. The most sensitive existing limits on 0ν DBD are from the ^{76}Ge searches IGEX and Heidelberg-Moscow and the search for 0ν DBD of ^{130}Te with Cuoricino. The IGEX experiment consisted of two phases. In the first phase, three small detectors were operated at three sites. In the second phase, three large enriched detectors were operated in the Canfranc underground laboratory in Spain. The limit on the half-life for 0ν DBD of ^{76}Ge from IGEX was 1.57×10^{25} yr (90% C.L.) [34].

The Heidelberg-Moscow (HM) experiment was a ^{76}Ge based 0ν DBD experiment at the Laboratori Nazionali del Gran Sasso. The limit on the 0ν DBD half-life set by the collaboration was 7.4×10^{24} yr (90 % C.L.) [35]. However, a small subset of the collaboration (KKDC) broke away and published a claim of discovery of 0ν DBD, with a half-life of (0.8 –

$18.3) \times 10^{25}$ yr (95 % C.L.) [36]. The confidence of the claim has since been improved through sophisticated pulse shape analysis techniques to remove multi-site background events (see figure 2.9) [22]. This claim is intriguing, but not widely accepted, as it is not supported by the full collaboration. It will be addressed by the next-generation experiments.

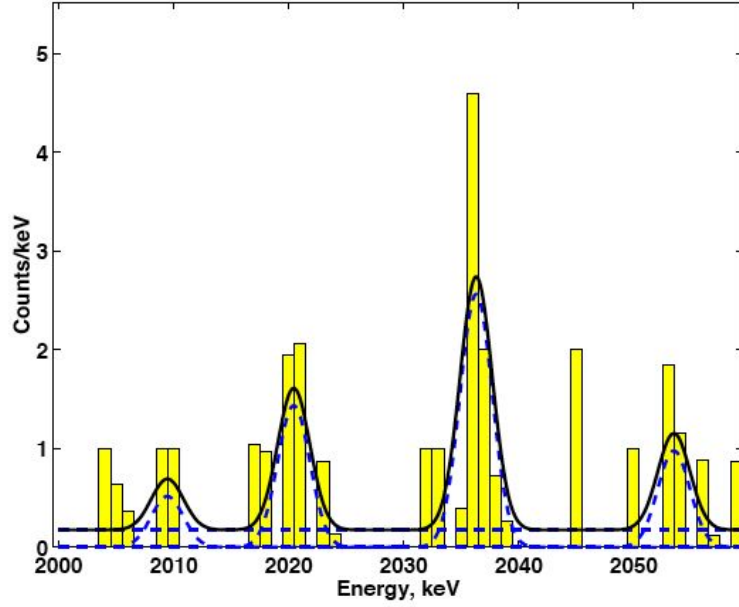


Figure 2.9. The KKDC claim of evidence for $0\nu\text{DBD}$ of ^{76}Ge in the Heidelberg-Moscow experiment. The expected $0\nu\text{DBD}$ peak in ^{76}Ge is at 2039 keV. The spectrum is shown after pulse shape selection for single site events, where the dashed lines are the individual fits to the background and the peaks, and the solid line is the sum of these fits [22].

In addition to the ^{76}Ge experiments, there are a number of experiments that searched for $0\nu\text{DBD}$ in other candidate isotopes. One example of a DBD experiment that does not use the source equals detector approach is NEMO. In fact, the NEMO collaboration has conducted a series of experiments, the latest incarnation of which is NEMO-3. In this experiment, thin foils of source isotope are mounted in a wire ionization chamber with plastic scintillator calorimeters [37]. This geometry allows track reconstruction. In addition to reducing background by identifying $\beta\beta$ events, this setup allows the measurement of the individual β -particle spectra, as well as measurement of the angle between the tracks of the two β -particles. These measurements can be used to distinguish between some $0\nu\text{DBD}$ mechanisms. While the NEMO-3 experiment has had great success in measuring the $2\nu\text{DBD}$

of several isotopes (including ^{100}Mo , ^{82}Se , ^{130}Te , ^{48}Ca , ^{116}Cd , ^{96}Zr , and ^{150}Nd), the energy resolution, small source mass, and background limit the sensitivity to $0\nu\text{DBD}$. An upgraded detector, called SuperNEMO, is planned for the future.

There are also a number of “next generation” $0\nu\text{DBD}$ experiments that will search for $0\nu\text{DBD}$ in detectors with hundreds of kilograms of source isotope mass. These include the EXO, GERDA, Majorana, and CUORE experiments, among others. These next generation experiments are summarized in table 2.2. The EXO experiment will search for $0\nu\text{DBD}$ of ^{136}Xe using a Xe time projection chamber (TPC) [38]. The first stage of this experiment, EXO-200, will contain 200 kg of liquid Xe and will be sited at the WIPP underground laboratory facility in New Mexico. A full one ton EXO is planned for the future. The group plans to identify possible double beta decay events in real time, trap the Ba^+ ions that result from the decay, and identify them using atomic spectroscopy. If this Ba tagging is successful, this will result in an experiment in which the only background is the tail of the $2\nu\text{DBD}$ spectrum.

GERDA [39] and Majorana [40] are two next generation ^{76}Ge $0\nu\text{DBD}$ experiments. The first phase of the GERDA experiment will consist of 18 kg of high purity Ge diode detectors, enriched in ^{76}Ge . The detectors will be submerged in a liquid argon bath, which will be instrumented to provide active shielding. In the second phase, an additional 20 kg of segmented detectors enriched in ^{76}Ge will be introduced. These electronically segmented detectors will provide precision position information, which will help in the identification of $0\nu\text{DBD}$ candidate events. The Majorana detector scheme consists of electronically segmented Ge diode detectors in a more traditional cryostat arrangement. Eventually, the Majorana and GERDA collaborations may merge to produce a 1-ton scale ^{76}Ge $0\nu\text{DBD}$ experiment.

CUORE is an upgrade of the Cuoricino experiment, the latest in a series of bolometric experiments to search for $0\nu\text{DBD}$. These experiments use TeO_2 bolometers to search for the $0\nu\text{DBD}$ of ^{130}Te . The Cuoricino and CUORE detectors will be discussed in detail in chapters 3 and 4.

Table 2.2. Summary of the four next generation $0\nu\text{DBD}$ experiments that are discussed in the text.

Experiment	Isotope	Enrichment	Technique	Reference
CUORE	^{130}Te	34% unenriched	Bolometric	[33]
EXO	^{76}Ge	80% enriched	Tracking	[38]
GERDA	^{76}Ge	86% enriched	Ionization	[39]
Majorana	^{136}Xe	86% enriched	Ionization	[40]

Chapter 3

The bolometric technique and the Cuoricino experiment

The site for both Cuoricino and CUORE is the Laboratori Nazionali del Gran Sasso (LNGS) in Assergi, Italy. The laboratory is located off a highway tunnel through the Gran Sasso d'Italia mountain (see figure 3.1). This location provides a 1400 m rock overburden (3100 m water equivalent (m.w.e.) [3]), which reduces the flux of cosmic ray muons by a factor of 10^6 . CUORE will be located in Experimental Hall A, next to Cuoricino.

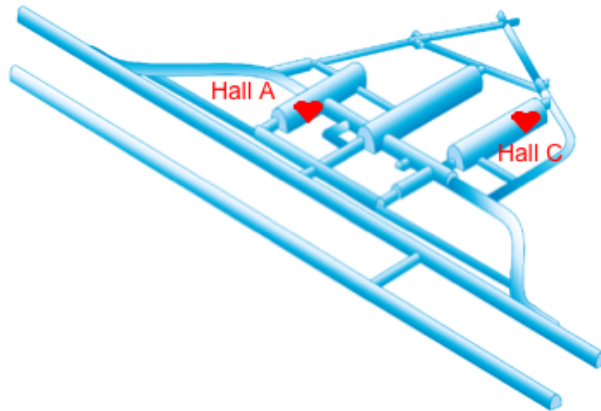


Figure 3.1. Overview of laboratory space at the Laboratori Nazionali del Gran Sasso (LNGS). The laboratory is located to the side of a highway tunnel in Italy. CUORE will occupy the space next to Cuoricino in Hall A. A second cryostat used for R&D is located in Hall C.

3.1 The bolometric approach

Both Cuoricino and CUORE are bolometric detectors. A bolometer measures deposited energy by acting as a phonon calorimeter. The basic design consists of an energy absorber weakly coupled to a cold reservoir and a sensitive thermometer (see figure 3.2). In order to function as a sensitive bolometer, the absorber crystal should be dielectric and have a low heat capacity at the operating temperature [41]. In this case, the heat capacity of the absorber at low temperatures ($T < T_D$) is given by the Debye Law:

$$C(T) \propto \left(\frac{T}{T_D}\right)^3, \quad (3.1)$$

where T_D is the Debye temperature. Radiation incident on the absorber crystal is converted into phonons, raising the temperature of the crystal. This temperature increase is then read out by the thermometer, in this case a neutron transmutation doped germanium (NTD Ge) thermistor.

Unlike detectors that rely on ionization or scintillation light, bolometers measure the full energy deposited in the absorber crystal. As a result, bolometers have extremely good energy resolution at low temperatures. The theoretical energy resolution of a bolometer is given by equation 3.2 [33]:

$$\sigma_E \propto \sqrt{kC(T)T^2}, \quad (3.2)$$

where k is the Boltzman constant. Note that this does not depend on the energy deposition. This theoretical limit is on the order of 20 eV for a 1 kg TeO_2 crystal operated at 10 mK [33]. In practice, the resolution achieved with these devices never reaches the theoretical limit. However, bolometers are still competitive with Ge detectors for energy resolution at MeV energy scales. Microbolometers are commonly used in astrophysical measurements. In addition, the MARE experiment will use bolometers to make a direct measurement of neutrino mass through the measurement of the endpoint of the ^{187}Re endpoint spectrum [16].

The use of bolometers to search for $0\nu\text{DBD}$ was first suggested by Fiorini and Niinikoski in 1983 [43]. The attractive aspects are the availability of the source equals detector ap-

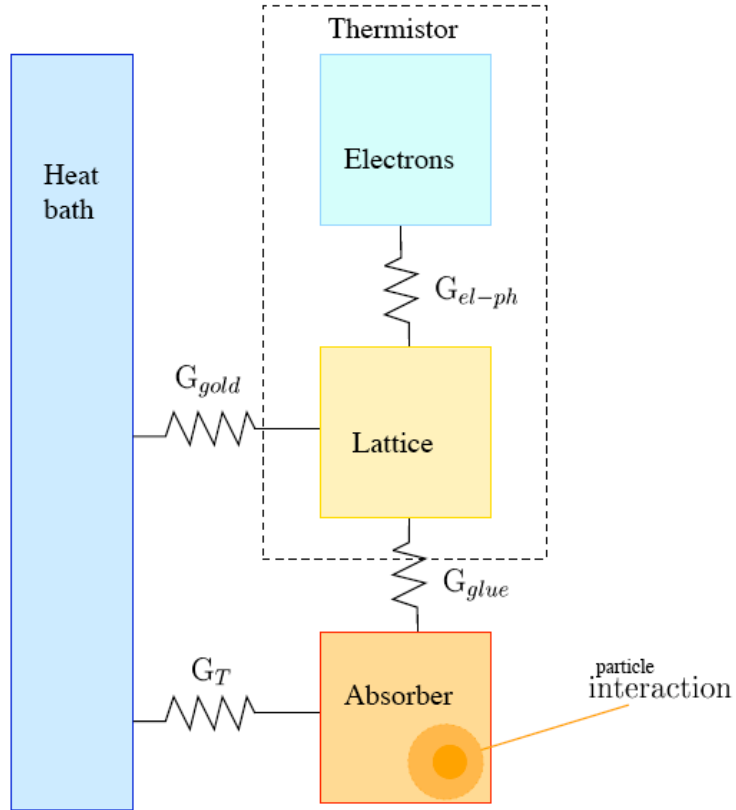


Figure 3.2. A schematic representation of a Cuoricino bolometer [42]. The absorber is coupled to the thermistor through thermal conductance G_{glue} . The thermistor system is made up of both a lattice component and an electron component, connected through the electron-phonon coupling G_{el-ph} . Both the absorber and the thermistor system are connected to a heat bath by weak thermal couplings G_T (Teflon mechanical supports) and G_{gold} (thermalized gold wires to provide the electrical connections). The heat bath is provided by copper frames, maintained at ~ 10 mK.

proach and the excellent energy resolution. The bolometric approach works for many different types of crystals, including many of the most commonly studied DBD isotopes. This allows a choice of the source isotope under study. For Cuoricino and CUORE, the isotope of interest is ^{130}Te .

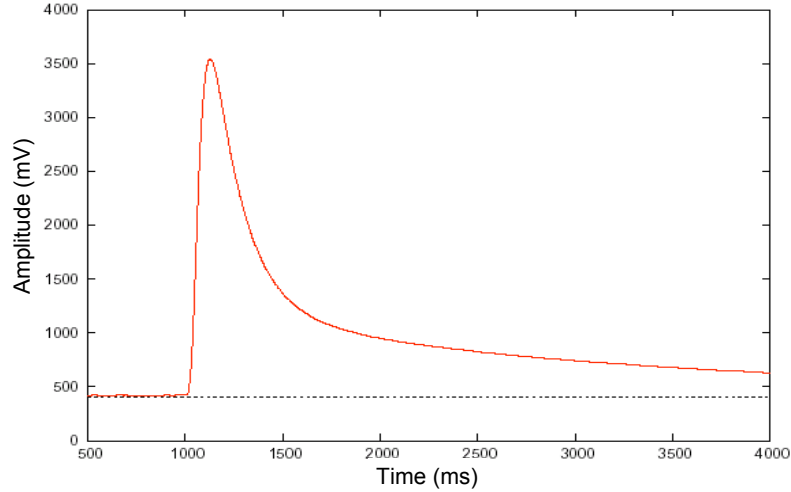


Figure 3.3. A Cuoricino pulse, showing the 4 s long event window. After 4s, the pulse has still not returned to the baseline level.

One drawback of the bolometric approach is that the signals are very slow. A typical pulse from the Cuoricino detector is shown in figure 3.3. Notice that the total length of the event window is four seconds. However, this is not a limitation in the search for rare nuclear processes with low background. The highest rate that the individual detectors can tolerate is around 100 mHz. After this point, pile-up, in which multiple pulses arrive during a single event window, begins to impact the live-time of the detectors.

3.2 Choice of isotope

Table 2.1 contains a list of candidate isotopes for $0\nu\text{DBD}$ searches. From equation 2.8, we see that the rate of the $0\nu\text{DBD}$ increases with the fifth power of the Q-value. ^{48}Ca has the highest Q-value at 4.3 MeV. Unfortunately, the other consideration in $0\nu\text{DBD}$ searches is total available source mass. Table 2.1 also shows the natural isotopic abundances of

the candidate isotopes. In this case, ^{48}Ca does not fare as well, with a natural isotopic abundance of 0.2%. ^{130}Te , on the other hand, has a natural isotopic abundance of 34%. Because ^{130}Te is so abundant, it is possible to carry out the $0\nu\text{DBD}$ search without the costly and time-consuming process of enrichment.

Another important consideration in the choice of isotope is the expected background in the $0\nu\text{DBD}$ region of interest. The Q-value of the DBD of ^{130}Te is 2530.30 ± 1.99 keV [44], above most of the naturally occurring γ -ray background. In fact, the $0\nu\text{DBD}$ region of interest lies between the last major naturally occurring γ background peak, the 2615 keV line from ^{208}Tl decay, and its Compton edge at 2360 keV, providing a region of particularly low background.

3.3 Cuoricino

The Cuoricino experiment was a bolometric $0\nu\text{DBD}$ experiment that ran from 2003 to 2008 at LNGS. Cuoricino was a proof of principle for the CUORE detector, as well as a sensitive $0\nu\text{DBD}$ experiment in its own right. The tower had a total source mass of 11.83 kg ^{130}Te , and a background in the region of interest of 0.18 ± 0.01 counts/keV/kg/year. The Cuoricino background spectrum in the region of the $0\nu\text{DBD}$ is shown in figure 3.4.

The data taken through March 2008 have been analyzed using a maximum likelihood analysis. Assuming a constant background and a Q-value of 2530 keV, the most recently published limit on the half-life for $0\nu\text{DBD}$ of ^{130}Te is $T_{1/2}^{0\nu\beta\beta}(^{130}\text{Te}) > 3.0 \times 10^{24}$ years at 90% confidence level [2]. However, the limit depends on both the background model used and the exact choice of Q-value. To extract a limit on the effective Majorana mass of the neutrino from the limit, it is necessary to choose a nuclear matrix element calculation. Table 3.1 contains calculations of $m_{\beta\beta}$ for a selection of nuclear matrix element calculations [2]. Details of the detector will be discussed in the following sections.

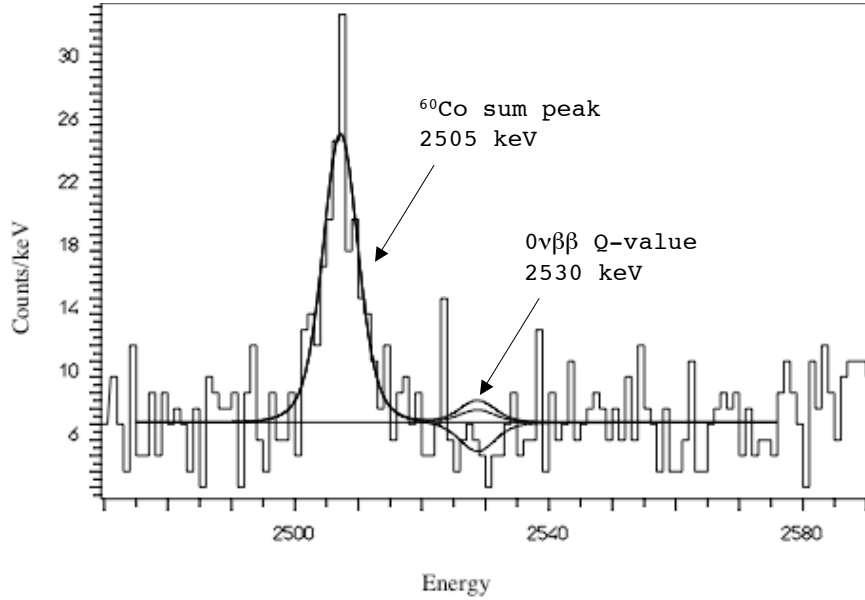


Figure 3.4. The most recent Cuoricino limit [2]. The large peak at 2505 keV comes from the decay of ^{60}Co . The $0\nu\text{DBD}$ Q-value lies to the right of this line at 2530 keV. The solid lines represent the best fit (which is negative with respect to the flat background), as well as the 68% and 95% confidence level bounds on the $0\nu\text{DBD}$ peak.

Table 3.1. Calculation of $m_{\beta\beta}$ for $T_{1/2}^{0\nu\beta\beta}(^{130}\text{Te}) > 3.0 \times 10^{24}$ years (90% confidence level) using selected nuclear matrix elements [2].

Reference	Method	$m_{\beta\beta}$ (eV)
Rodin 2007 [32]	using $2\nu\text{DBD}$ to fix g_{pp}	0.46
Staudt 1992 [45]	pairing (Bohm)	0.19
Pantis 1996 [46]	no p-n pairing	0.52
Vogel 1986 [47]		0.47
Civitarese 2005 [48]		0.42
Tomoda 1991 [49]		0.42
Barbero 1999 [50]		0.33
Simkovic 1999 [51]	pn - RQRPA	0.68
Suhonen 1992 [52]		0.64
Muto 1989 [53]		0.39
Stoica 2001 [54]		0.60
Faessler 1998 [55]		0.55
Engel 1989 [56]	seniority	0.29
Aunola 1998 [57]		0.41
Caurier 2008 [58]	Nuclear Shell Model	0.58

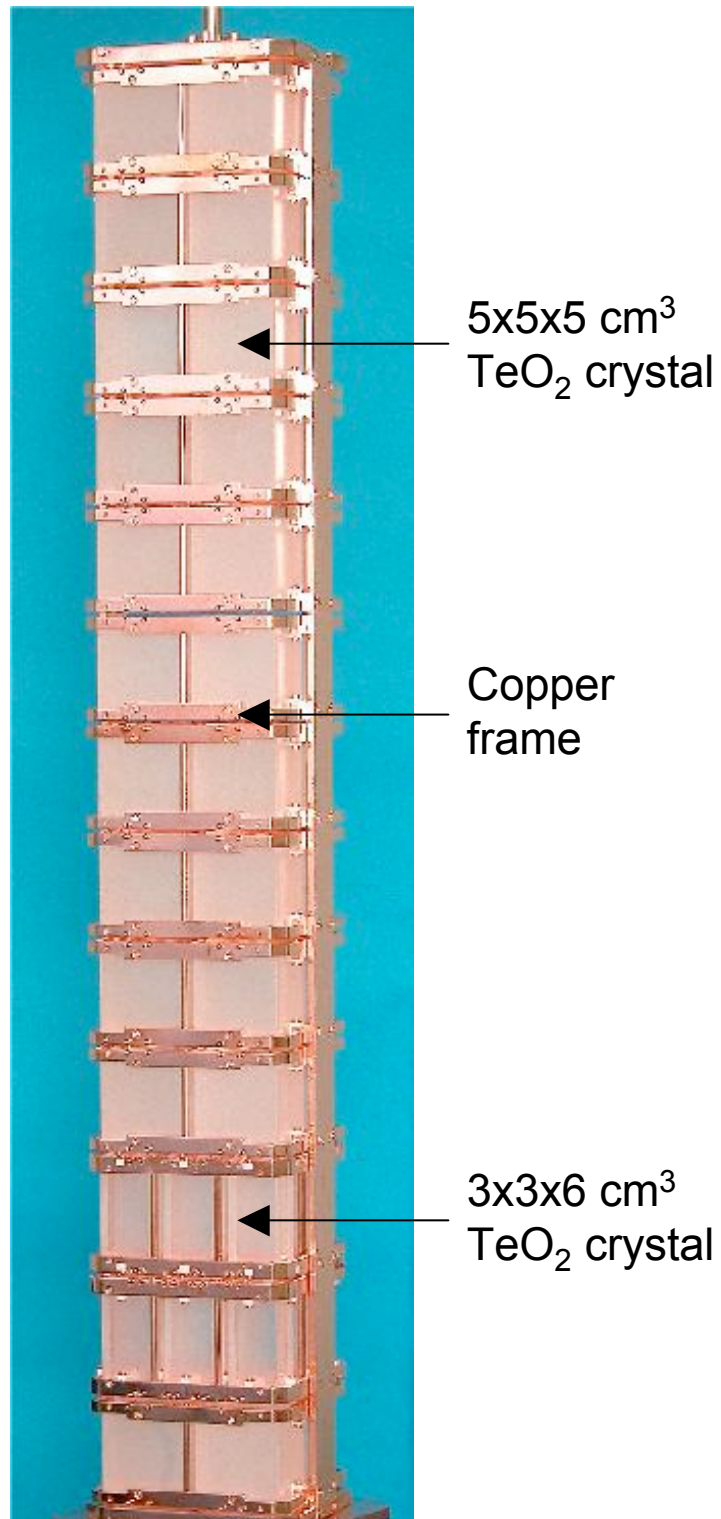


Figure 3.5. The Cuoricino tower, without copper shielding, showing the eleven planes of four crystals and two planes of nine crystals.

3.3.1 The tower

The Cuoricino tower is shown in figure 3.5. Cuoricino consisted of thirteen layers of TeO_2 bolometers. Eleven of the layers were made up of $5 \times 5 \times 5 \text{ cm}^3$ unenriched crystals. The remaining two layers contained crystals from the previous Milano $0\nu\text{DBD}$ experiment, MiDBD. Each of these layers contained nine $3 \times 3 \times 6 \text{ cm}^3$ crystals. Two of these smaller crystals were enriched in ^{130}Te , and two were enriched in ^{128}Te . The enriched crystals were designed to measure the $2\nu\text{DBD}$ spectrum of ^{130}Te by subtracting away the background seen in the crystals enriched in ^{128}Te . The result of this analysis was a measurement of the $2\nu\text{DBD}$ half-life of 6.1×10^{20} years [59].

The crystals for Cuoricino were grown at the Shanghai Institute of Ceramics (SICCAS) through the Bridgeman growth method. Te metal was first refined and then converted into TeO_2 powder. In order to grow a TeO_2 crystal, TeO_2 powder was placed into a platinum crucible with a seed crystal, and the crucible was then passed through a heating element at high temperature. At SICCAS, each crystal was crushed and reprocessed after a first growth and regrown to produce a final crystal for Cuoricino. With each crystal growth, impurities in the TeO_2 powder were rejected by the crystal lattice. However, other impurities such as platinum may have been preferentially included.

Each crystal received surface treatment to reduce radioactive backgrounds and to prepare the crystal for thermistor bonding. This treatment involved an acid etch step to remove surface contaminations and a lapping and polishing step to further remove surface material and prepare the surface for thermistor bonding.

The crystals were mounted in copper frames with Teflon standoffs. The copper, with good thermal conductivity, was maintained between 8 and 10 mK and provided the heat bath for the detectors. The Teflon provided both mechanical support for the individual crystals as well as a weak thermal link to the heat bath. Each crystal was mounted with a silicon heater and a thermistor. The gold wires that provided the electrical connections for these components were another weak thermal link to the heat bath.

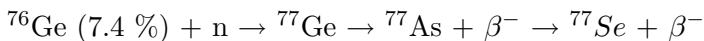
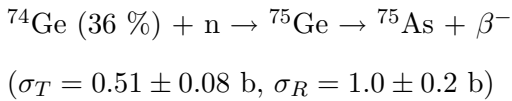
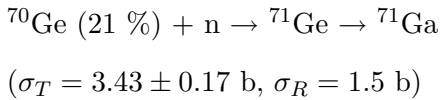
3.3.2 Cryogenics

Cuoricino was cooled by a ^3He - ^4He dilution refrigerator made by Oxford Cryogenics. The refrigerator was installed in 1989 and operated almost continuously since Cuoricino came online in 2003. It previously housed the MiDBD $0\nu\text{DBD}$ experiment. Cuoricino was able to reach a working temperature as low as 8 mK. The temperature of the tower was stabilized through a heater with a feedback mechanism.

The cryostat was cooled to a temperature of 4 K by filling the main bath with liquid He (LHe). During the first half of the Cuoricino experiment, the LHe level was maintained by a He liquefier module mounted next to the cryostat. However, problems with the liquefier limited the live time of the experiment. As a result, the liquefier was disconnected, and the main bath was refilled manually every two days. The LHe boil-off was connected to an external reliquefaction system to recover the He.

3.3.3 Thermistors

The thermistors for Cuoricino had to be uniform and relatively large to preserve good energy resolution for the large absorber crystals. In order to achieve this, the thermistors were made of neutron transmutation doped germanium (NTD Ge). The NTD Ge was made by placing Ge wafers of normal isotopic composition into a reactor. The neutron capture reactions on the stable Ge isotopes produced the desired doping level. The reactions and cross sections of interest are:



($\sigma_T = 0.16 \pm 0.014$ b, $\sigma_R = 2.0 \pm 0.35$ b)

The resistance as a function of temperature is given by equation 3.3:

$$R = R_0 \exp T_0/T^\gamma, \quad (3.3)$$

where $\gamma = 1/2$ and R_0 and T_0 are experimentally determined parameters. Because R_0 does not vary much, T_0 can be used to characterize the NTD Ge material. Figure 3.6 shows how T_0 varies with the measured neutron fluence for a series of Ge irradiations.

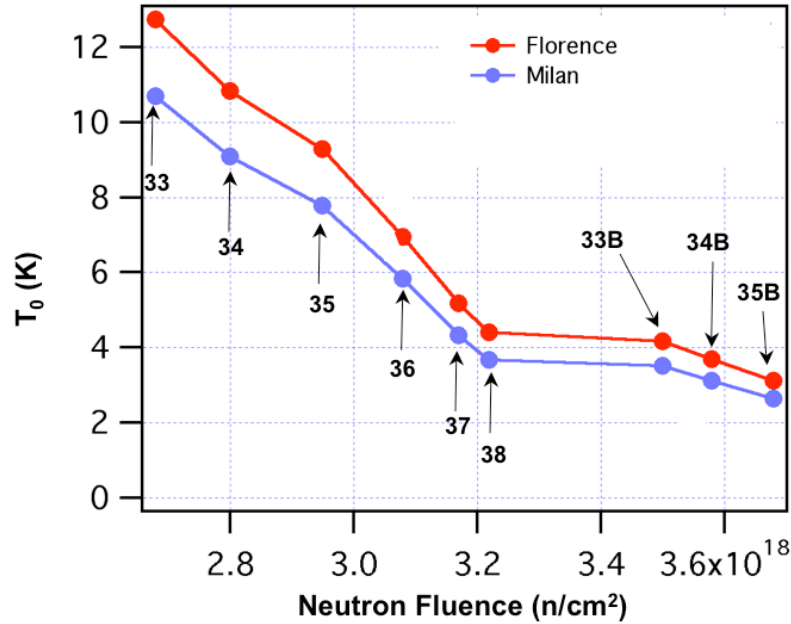


Figure 3.6. NTD Ge thermistor T_0 vs. measured neutron fluence for a series of Ge irradiations. The two curves represent measurements carried out at two different facilities, one in Milan and one in Florence. There is a systematic variation in the T_0 measured in the two facilities. Figure courtesy R. Maruyama.

Cuoricino thermistors were made by a “shotgun” approach, in which several batches of Ge wafers were irradiated for different periods of time. After the radioactivity produced in the Ge by the irradiation decayed away to an acceptable level, the electrical properties of each batch were measured and used to select the best material for the application. For Cuoricino, the thermistor material was designated NTD-31.

3.3.4 Calibration and stabilization

The detectors were calibrated with two thoriated wires inserted along the outside of the cryostat. The wires provided uniform illumination of the tower with γ -rays up to 2615 keV. Each calibration run lasted approximately 3 days, and was done once a month, or as needed. For analysis purposes, a Cuoricino data “run” is defined as a period between calibrations. In order for a run to be accepted, the initial and final calibrations must be in agreement.

Because the energy of a given pulse depends directly on the temperature of a given detector, it is important to be able to correct for fluctuations in the temperatures of the individual detectors. For this reason, each crystal was equipped with a Si heater that was remotely injected with a known amount of current. This stabilization pulse was sent to each crystal every 300 seconds. The temperature fluctuations of the crystal were expected to happen on a much smaller time scale than this. In order to stabilize the detector gains, the heater pulses are plotted as pulse amplitude vs. detector temperature, which is proportional to the baseline (see figure 3.7). The resulting curve is fitted and used to correct the amplitudes of individual pulses based on the mean baseline immediately preceding the pulse.

3.3.5 Background

The background in the $0\nu\text{DBD}$ signal region is an important component of the sensitivity of a given $0\nu\text{DBD}$ experiment. The major tools for background reduction in Cuoricino were careful screening and cleaning of materials, shielding from environmental radioactivity, and active vetoing of background events.

The copper, Te metal, Teflon, and lead for CUORE were all screened before beginning production of detector components. The lead used for the inner shielding of Cuoricino was ancient Roman lead, retrieved from a sunken ship at the bottom of the Mediterranean. Because this lead was 2,000 years old, it was free from naturally occurring ^{210}Pb contami-

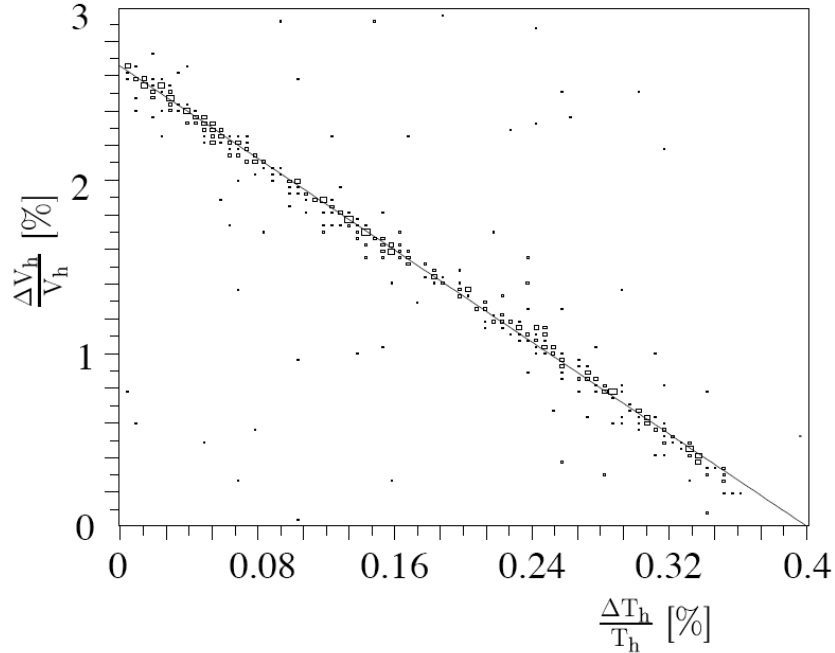


Figure 3.7. Percent change in heater pulse amplitude vs. percent change in detector temperature used for Cuoricino gain stabilization [42].

nation (the half-life of ^{210}Pb is 22 years). In addition, ^{210}Pb could not be produced in the lead through cosmic ray neutron activation because of the water overburden.

In addition to the shielding provided by the LNGS overburden, the Cuoricino cryostat and detectors were surrounded on all sides by several layers of shielding. The outer layers of shielding protected the detector from environmental γ -rays and neutrons. The innermost layers of shielding had to meet strict radioactivity limits, while protecting the detector from gamma radiation produced in the outer shielding.

Background events that reached the detector can be actively rejected in software. The Cuoricino analysis includes two main types of background rejection. The first is pulse shape analysis, in which spurious sources of noise such as vibrations, electrically induced jumps in the baseline, and pile-up events are rejected based on the shape of the pulse. A second layer of analysis is an anti-coincidence veto that allows rejection of events that occur in more than one detector simultaneously. This allows rejection of Compton scattered γ -rays, some surface α particle events, and high-energy cosmic rays.

It is because of the careful effort put into background reduction that Cuoricino achieved the impressive background counting rate of 0.18 ± 0.01 counts/keV/kg/yr. However, in order to achieve the sensitivity goals of the next generation of $0\nu\text{DBD}$ experiments, even more heroic efforts to reduce background must be made.

Chapter 4

The next-generation experiment: CUORE

The CUORE detector (figure 4.1) is essentially nineteen Cuoricino-like towers arranged in a cylindrical shape inside a single cryostat. The goal of the CUORE detector is to achieve sensitivity to the inverted neutrino mass hierarchy. By increasing the mass by a factor of twenty and reducing the background by a similar factor, the CUORE collaboration will improve the sensitivity of the experiment to the ^{130}Te half-life by a factor of twenty. Construction of CUORE is scheduled for completion in 2012. Full details can be found in the CUORE proposal [33].

4.1 Improving on the Cuoricino design

In order to achieve the physics goals of CUORE, the collaboration will have to improve the average energy resolution of the individual detectors. The goal is an improvement from the current average resolution of Cuoricino at 2615 keV of 7.9 keV to 5 keV in CUORE. This improvement will be realized by a more uniform and reproducible crystal mounting. The new detector structure, known as the “Gorla” configuration, includes an increased amount

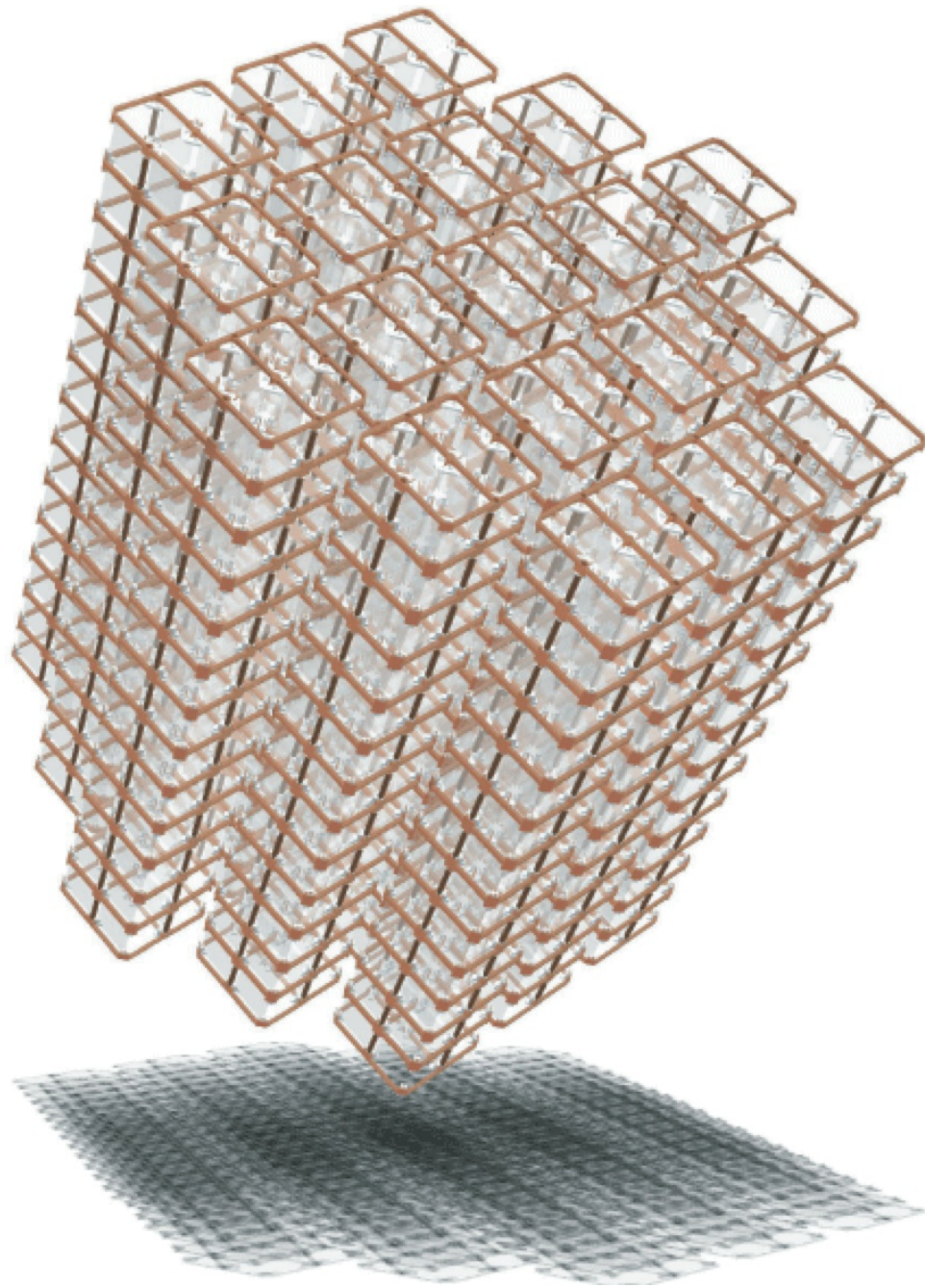


Figure 4.1. Rendering of the future CUORE detector, showing nineteen close packed towers in a cylindrical arrangement. Each tower will have thirteen planes of four crystals, for a total of 988 individual detectors.

Table 4.1. Technical specifications for cooling power of pulse tube refrigerators and dilution unit as a function of temperature.

Temperature	Cooling power
4.2 K	1.5 W
120 mK	> 1.5 mW
20 mK	30 μ W
12 mK	5 μ W

of Teflon, along with reduced copper. The crystal size tolerances are also much tighter than they were for the Cuoricino tower.

In CUORE, unlike Cuoricino, data will be acquired continuously. This will improve the ability to understand complex events that take place over multiple channels, to reject backgrounds that generate low-energy events in neighboring crystals, and to examine low energy phenomena (such as axion and dark matter searches) which occur very close to the energy threshold of the detectors.

4.1.1 Cryogenics and shielding

Unlike Cuoricino, CUORE will be cooled by a He-free pulse tube system. The system will be built by Leiden Cryogenics, headed by Giorgio Frossati. The cooling power at various temperatures is shown in table 4.1. The design of the cryostat and cryogenic apparatus, including the cold lead shielding, can be seen in figure 4.2.

One problem with the mechanical cooling and dilution refrigeration unit is the amount of vibrational noise. This can generate false events in the crystals. The CUORE tower will be mechanically decoupled from the dilution unit.

In addition to the ton of detector materials that must be cooled by the CUORE dilution refrigerator, there will also be cold shielding, including ancient Roman lead (see figure 4.2). Because it is very difficult to move the detectors once assembled, the shielding for CUORE will be lifted up around the detector. The detector will be assembled in a clean room on the second floor of the hut, below the dilution refrigerator.

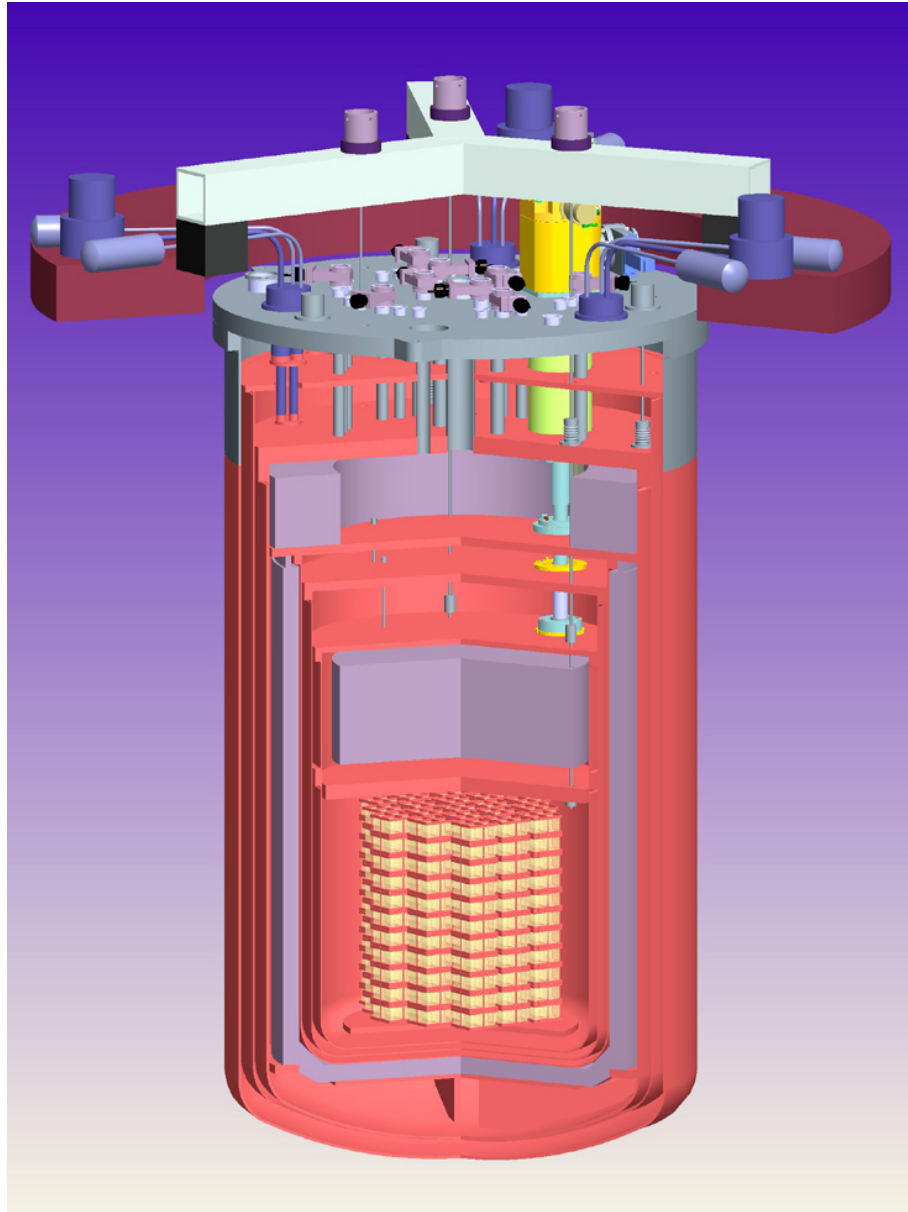


Figure 4.2. Rendering of the future CUORE cryostat, showing the copper cryostat (orange), three pulse tube refrigerators (dark purple) mounted to the top flange (gray), the dilution unit (green), and the cold lead shielding (light purple).

4.1.2 Thermistors

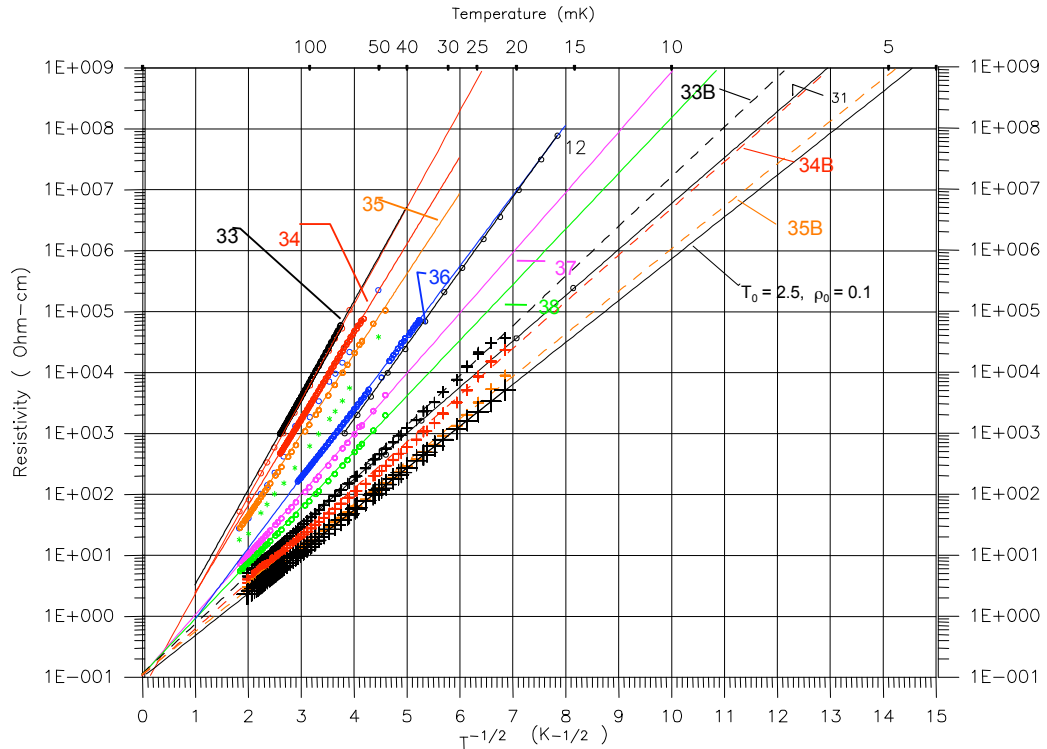


Figure 4.3. Results of cold testing thermistor series 33-38 and 33B-35B. Doping levels increase from left to right. The fit to the NTD 31 cold test data is also included. It is in good agreement with the data for NTD 34B. Figure courtesy J.W. Beeman.

For the CUORE experiment, we will produce 1,250 NTD Ge thermistors. The material for these thermistors should have electrical properties very similar to NTD-31, the material used for Cuoricino thermistors. A study of the electrical properties of NTD material as a function of neutron dose was made. For NTD series 33 through 39, monitor foils accompanied the Ge wafers during irradiation. This allowed the total neutron fluence to be extracted. In addition, NTD 33-35 received a second dose, along with monitor foils, in order to achieve electrical properties similar to Cuoricino Ge (these NTD series are designated B/C). Electrical testing at low temperatures showed that NTD-34B/C was the most similar to NTD-31 (see figure 4.3). In order to achieve the correct doping level, the NTD Ge material should be identical to NTD-34B/C within 1%. Production of NTD Ge thermistors is one of the projects I have collaborated on as part of the CUORE collaboration.

There are several difficulties to overcome in the production of precisely doped NTD Ge. One problem is reactor stability. The neutron flux and energy spectrum of the reactor change over the course of the reactor fuel cycle. Because the dopants have very different cross-sections for thermal neutron capture and epithermal neutron capture, the reactor spectrum can change the ratios of Ga, As, and Se in the Ge wafer. Another problem is the non-uniformity of the neutron flux in the reactor irradiation facility.

Two batches of Ge wafers were doped at the MIT Nuclear Reactor Laboratory (MIT NRL). MIT NRL solves the problem of flux non-uniformity through a special irradiation facility. In this facility, the samples are passed slowly under the core of the reactor and rotated to ensure uniform exposure. NTD-39 finished its final pass in August 2006, and neutron fluence monitors indicate a predicted doping level of 90% of the doping level of NTD-34B/C. NTD-40 received an additional pass, which it completed in early 2007. The target doping for this set of wafers was 100% that of NTD-34B/C. Electrical testing of NTD Ge material requires a waiting period of approximately one year, during which the radioactivity decays to a point where it does not interfere with the measurement. In order to do neutron activation analysis (NAA) of NTD Ge, it is necessary to wait until at least 99% of the activation products have decayed into their final dopants. The longest half-life in this chain is the 11.4 day half-life of ^{71}Ge , which gives a waiting period of only 3 months. I worked on a project to use NAA to determine the relative doping levels of NTD 39 and NTD 40 with respect to NTD 34 B/C.

Neutron Activation Analysis

NAA is a method for identifying and quantifying trace concentrations of elements in small samples. In this method, a sample is exposed to a high neutron flux in a nuclear reactor. In order for the method to work, the element under study must have at least one stable isotope that is converted into a suitable radioactive isotope through neutron capture. A suitable radioactive isotope will have a half-life on the order of days and a characteristic γ -ray energy that is easy to observe with γ -ray spectroscopy. While it can be

difficult to obtain an absolute measurement of trace element concentrations using NAA, it is straightforward to determine the relative concentration between two samples.

In December 2007, we irradiated four germanium samples (an undoped Ge blank, NTD 34C, NTD 35B, and NTD 40) in the silicon irradiation facility at the McClellan Nuclear Radiation Center (MNRC) for 30 minutes. The samples were shipped to the LBL on-site Low Background Facility for gamma counting with high purity Ge (HPGe) detectors. The samples were counted individually at 0 cm from the face of a single HPGe detector.

Because of the large continuum background and numerous γ -rays produced by ^{77}Ge (produced by neutron capture on ^{76}Ge), the best available γ -ray to determine the doping level of the samples was the 835 keV ^{72}Ga peak produced by neutron capture on the ^{71}Ga dopant. However, ^{72}Ga can also be produced by fast neutrons through the reaction $^{72}\text{Ge}(n,p)^{72}\text{Ga}$. The inclusion of the undoped sample allowed us to correct for the ^{72}Ga produced through the (n,p) reaction.

The other dopant that can be identified through NAA is ^{75}As , which produces ^{76}As through neutron capture. The strongest γ -ray transition in ^{76}As is at 559 keV (45% branching ratio) [26]. However, there is a γ -ray produced by ^{77}Ge at 558 keV (16.1% branching ratio) which makes the As impossible to resolve using this peak. The next strongest γ -ray transition in ^{76}As is at 657 keV (6.2% branching ratio). This peak was not visible above the continuum background at the time of counting, and it will be too small to acquire sufficient statistics as it emerges from the background. The sample properties and the results of the December 2007 NAA are summarized in table 4.2. Errors shown are statistical only, although there is also some systematic uncertainty from the deadtime correction and the small differences in counting geometry.

Because we did not achieve the desired statistics in the December run, we irradiated another batch of samples in March 2008. This time, we also included a sample of NTD 39. The samples were irradiated for 1 hour in the silicon facility at MNRC and shipped back to the LBL low background counting facility. The samples were counted at 2.4 cm from the face of a single HPGe detector. The results of the second run are summarized in table

Table 4.2. Summary of sample properties and results from the December 2007 NAA.

	Undoped Ge	NTD 34C	NTD 40
Mass (g)	0.7936	1.1253	1.6558
Start time delay (s)	73380	23100	0
Count time (s)	93100	43662	22692
Live time fraction	0.9860	0.9620	0.9254
835 keV counts	1728 ± 143	24517 ± 319	27052 ± 460
Relative doping level	-	-	$0.953 \pm .023$

Table 4.3. Summary of sample properties and results from March 2008 NAA.

	Undoped Ge	NTD 34C	NTD 39	NTD 40
Mass (g)	1.562	0.789	1.572	1.549
Start time delay (s)	25260	0	68700	60360
Count time (s)	34921	25048	13087	7827
Live time fraction	0.9450	0.9581	0.9628	0.9582
835 keV counts	4770 ± 146	17381 ± 249	6430 ± 117	5392 ± 82
Relative doping level	-	-	0.806 ± 0.023	1.035 ± 0.025

4.3. Again, only statistical errors are shown. An effort was made to create a more uniform counting geometry for all four samples. The γ -ray spectrum in the region of the ^{72}Ga peak is shown in figure 4.4.

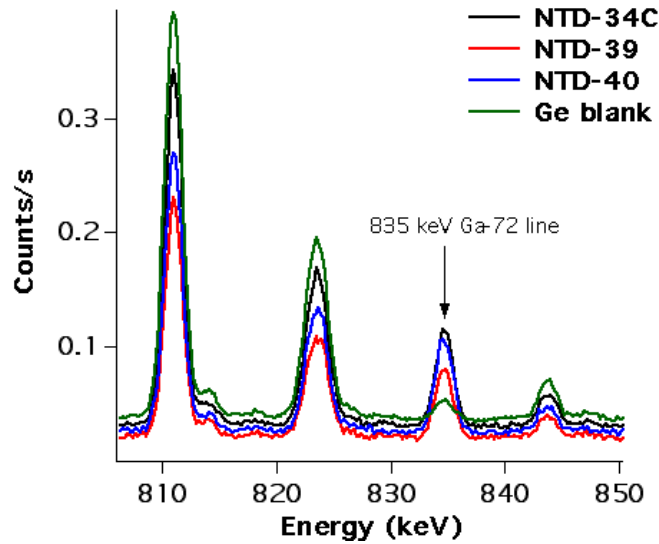


Figure 4.4. Spectrum from the March 2008 NTD Ge NAA. The ^{72}Ga peak at 835 keV can clearly be seen in all samples including the undoped sample, indicating the background due to the (n,p) reaction.

Table 4.4. CUORE 5-year sensitivity to the $0\nu\text{DBD}$ half-life of ^{130}Te , assuming 5 keV resolution at 2530 keV. The spread in $m_{\beta\beta}$ is the result of the spread in the nuclear matrix elements.

Background	Half-life sensitivity	$m_{\beta\beta}$
0.01 counts/keV/kg/yr	$T_{1/2}^{0\nu\beta\beta} > 2.1 \times 10^{26}$ yr	19 - 100 eV
0.001 counts/keV/kg/yr	$T_{1/2}^{0\nu\beta\beta} > 6.5 \times 10^{26}$ yr	11 - 57 eV

4.2 Background characterization

The ultimate sensitivity of the CUORE experiment will be determined by the level of background achieved in the region of the $0\nu\text{DBD}$ peak at 2530 keV. A summary of the 5 year sensitivity of CUORE in different background scenarios is given in table 4.4. The half-life sensitivity of the experiment over 10 years of data acquisition is illustrated in figure 4.5.

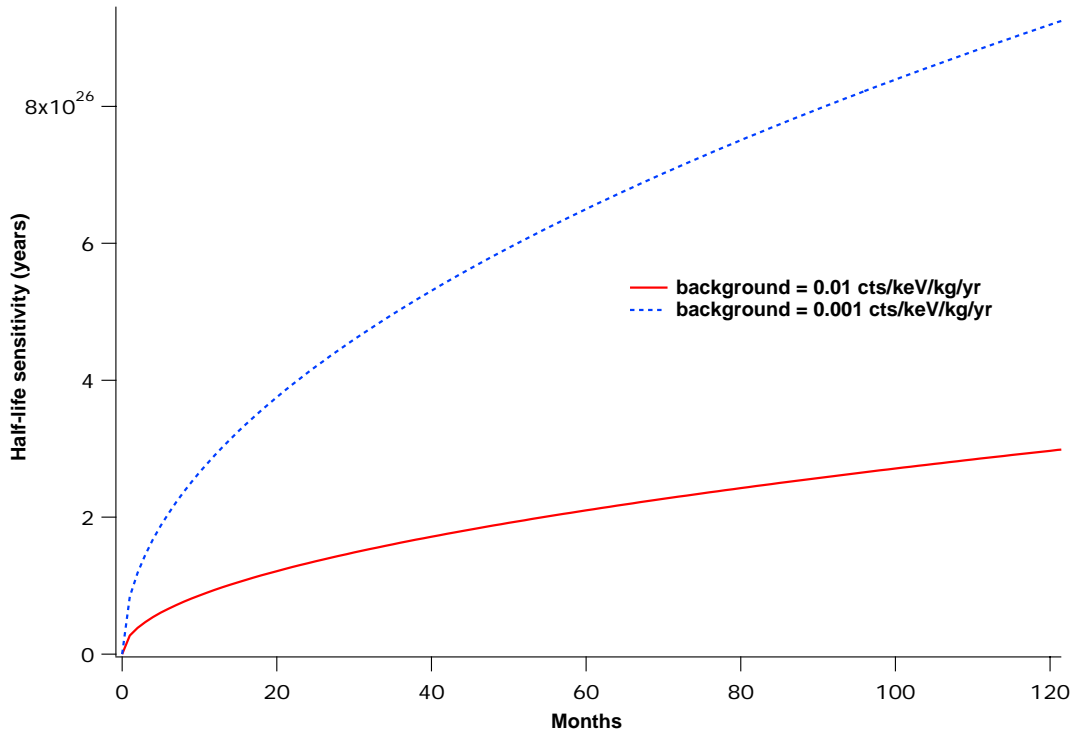


Figure 4.5. The half-life sensitivity of the CUORE experiment as a function of time for different background scenarios.

4.2.1 Radioactive contaminants

Radioactive contaminants can be present in the raw detector materials or introduced later through processing or radon contamination. Contaminants in raw materials can be reduced through careful screening. The CUORE collaboration uses three main techniques for screening materials: direct γ -ray and α -particle spectroscopy, inductively coupled plasma mass spectroscopy (ICP-MS), and neutron activation analysis (NAA). One example of the use of NAA to measure contaminants in detector materials is the analysis of Cuoricino Teflon carried out in 2004. This was one of the first projects that I participated in as a CUORE collaborator.

Neutron activation analysis of Teflon

While the Cuoricino Teflon (polytetrafluoroethylene, or PTFE) was known to be clean enough for that experiment, the sensitivity with which it had previously been measured was not good enough for the radiopurity standards of CUORE. We carried out NAA on a sample of Cuoricino PTFE in order to test the concentrations of uranium and thorium contaminants in the material. During the irradiation, neutrons are captured by ^{238}U to produce ^{239}U , which quickly β -decays to ^{239}Np . The strongest γ -ray transitions in ^{239}Np are at 106 keV (27% branching ratio) and 278 keV (14% branching ratio) [26]. Because the half-life of ^{239}Np is only 2.4 days, it is important to count the sample as quickly as possible after the irradiation in order to observe the U contamination. The thorium in the sample undergoes the $^{232}\text{Th}(n,\gamma)^{233}\text{Th}$ reaction. ^{233}Th then β -decays to ^{233}Pa , which has a half-life of 27 days. The strongest γ -ray transition in ^{233}Pa is at 312 keV (39% branching ratio).

The NAA sample consisted of six 6.4 g pieces of PTFE, machined using steel tools from the same stock as the PTFE for Cuoricino. Each piece was a cylinder, 1.6 cm in diameter, and 1.6 cm high. We packaged the sample in a 10 cm long tube with a Standard Pottery monitor at either end. The Asaro-Perlman Standard Pottery is a powder standard developed at Lawrence Berkeley National Laboratory (LBNL) with well known concentrations of a variety of elements, including uranium and thorium [60].

The sample was irradiated in the in-core “rabbit” irradiation facility at the McClellan Nuclear Radiation Center for 33 minutes at 1.8 MW reactor power. After a two day waiting period, the sample was shipped back to LBNL for γ -ray counting with high purity Ge detectors at the Low Background Facility. We cleaned the individual PTFE pieces with hydrofluoric acid before counting to remove surface contamination. Later, the top and bottom surfaces were machined off in order to further observe surface effects. No difference in the counting rate was observed, indicating that the measured contamination was present in the bulk of the material, rather than on the surface. A portion of the spectrum from one counting run can be seen in figure 4.6, including the peaks that indicate the presence of uranium and thorium.

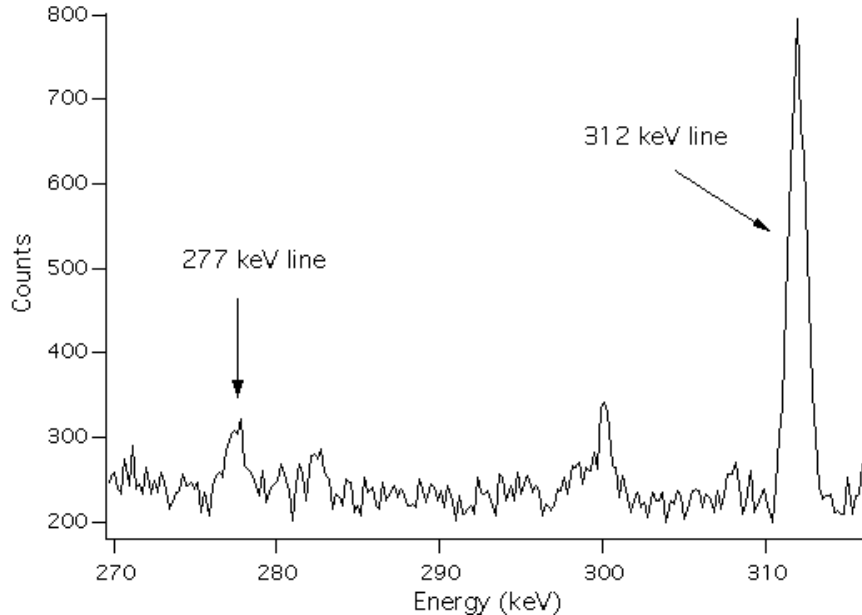


Figure 4.6. Spectrum from the 2004 NAA of Cuoricino PTFE. The ^{239}Np line at 277 keV indicates the presence of uranium, and the ^{233}Pa line at 312 keV indicates the presence of thorium. This spectrum represents 22 hours of counting time and was taken 11 days after the irradiation.

By comparing the 277 keV peak and 312 keV peak counting rates in the samples with those in the Standard Pottery monitors, we have measured concentrations of 200 ppt of uranium ($\sigma = 10 - 20\%$) and 300 ppt of thorium ($\sigma < 10\%$) in Cuoricino PTFE. It is unknown whether the parent nuclei are in equilibrium with their daughter nuclei. While

this level of contamination provides a negligible contribution to the Cuoricino background, it is above the radiopurity tolerances for CUORE. As a result, a new PTFE supplier was found, with measured upper limits on the uranium and thorium concentrations that are a factor of 100 lower than in the Cuoricino PTFE.

4.2.2 Cosmic ray induced radioactivity

In addition to radioactive contamination, detector materials can also be activated by cosmic ray interactions during their time on the Earth's surface. One of the most dangerous types of activity that can be created by cosmic rays on Te is ^{60}Co . ^{60}Co decays by β -emission, in coincidence with a cascade of γ -rays at 1173 keV and 1333 keV. The sum of these γ -rays gives a peak at 2505 keV, which can be seen in figure 3.4. When this decay happens inside the absorber crystal, the β -particle deposits up to 318 keV of energy in coincidence with the two γ -rays, which creates a continuum background in the $0\nu\text{DBD}$ region of interest.

In order to protect detector materials from cosmic ray activation, the TeO_2 crystals, copper, and lead for CUORE should have the minimum possible exposure to surface-level cosmic rays. Detector materials will be stored underground at LNGS as much as possible. In addition, TeO_2 crystals will be transported from SICCAS to Italy by ship rather than by air in order to avoid exposure to the increased cosmic ray flux at high altitude.

4.2.3 Prompt cosmic ray backgrounds

Although the cosmic ray muon flux in the underground laboratory at LNGS is reduced by a factor of 10^{-6} with respect to the surface, cosmic ray muons can still have a measurable impact on the CUORE detector. Muons that interact in the detector or produce a hadronic shower very close to the detector can be vetoed by anti-coincidence cuts on the CUORE data. However, muons may also produce spallation neutrons by interacting with the rock in the cavern walls or the detector's outer lead shielding. The background produced by neutrons in the CUORE detector will be discussed in chapter 5.

Chapter 5

Measurement of neutron-induced backgrounds

Neutrons are emerging as an important source of background for next generation $0\nu\text{DBD}$ experiments. They present much greater difficulties for dark matter experiments, for which the nuclear recoil produced by a neutron is identical to the WIMP-induced nuclear recoil of interest. For $0\nu\text{DBD}$ experiments, the neutron-induced backgrounds of interest are those that can deposit energy in the region of the $0\nu\text{DBD}$ peak. In addition to elastic scattering, which can increase the background continuum level, there are also inelastic reactions which can produce γ -ray peaks close to the Q-value of $0\nu\text{DBD}$.

The main sources of neutrons in underground laboratories are naturally occurring radioactivity and high-energy cosmic rays. First, α -particles from the uranium and thorium decay chains are produced in the laboratory rock and concrete, as well as detector and shielding materials. Then, (α, n) reactions can produce neutrons with energies up to about 8 MeV. In addition, high-energy cosmic ray muons can produce spallation neutrons through interactions in the nearby rock overburden or in shielding materials. In general, these neutrons have a much harder energy spectrum.

5.1 Neutron-induced backgrounds underground

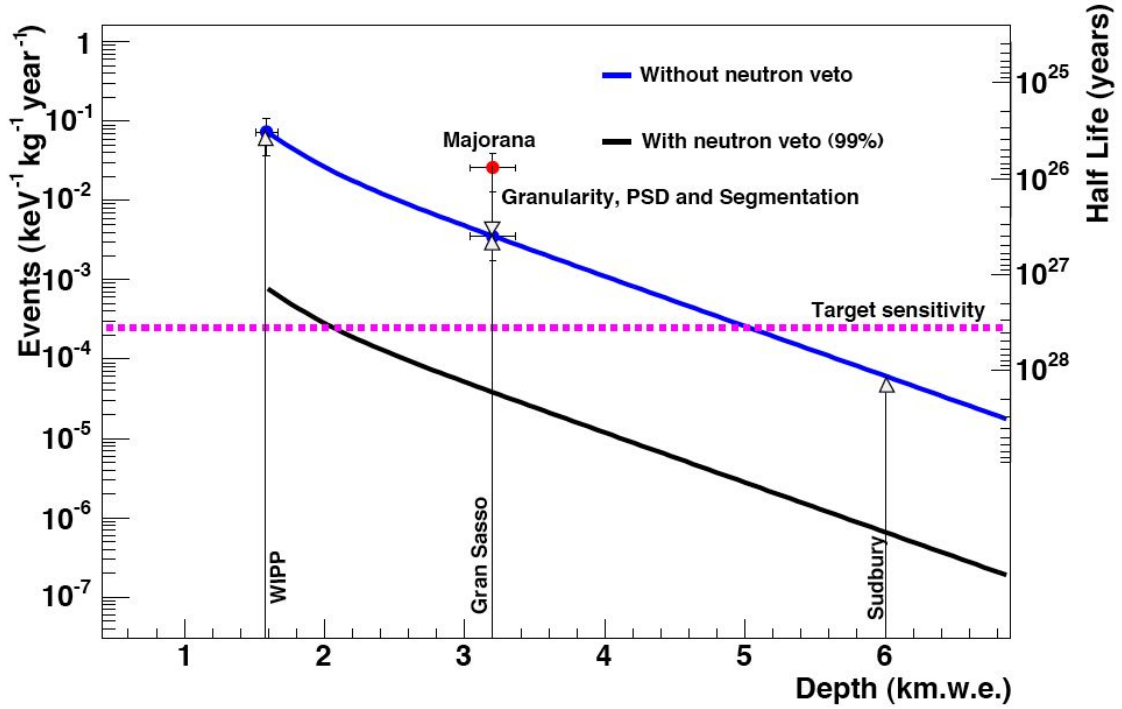


Figure 5.1. Depth-sensitivity-relation for a Majorana-like $0\nu\text{DBD}$ experiment, from Mei and Hime, 2005 [3].

In 2005, Mei and Hime released a Monte Carlo study of depth requirements for $0\nu\text{DBD}$ and dark matter experiments [3]. In this report, they stated that the overburden alone at LNGS is not sufficient to reduce the background induced by fast muons below target levels for a Majorana-like $0\nu\text{DBD}$ experiment (see figure 5.1). These backgrounds originated mainly from neutrons produced by muon interactions in rock and shielding materials.

Before the neutrons reach the detector, they must pass through the detector shielding and other passive components, which modifies the neutron spectrum by thermalizing high energy neutrons. In addition to modifying the neutron spectrum, this can also produce secondary radiation, including γ -rays and charged particles, which can directly affect the background in the detectors. In addition, the neutrons that reach the detector can directly produce background events.

5.1.1 Simulations for CUORE

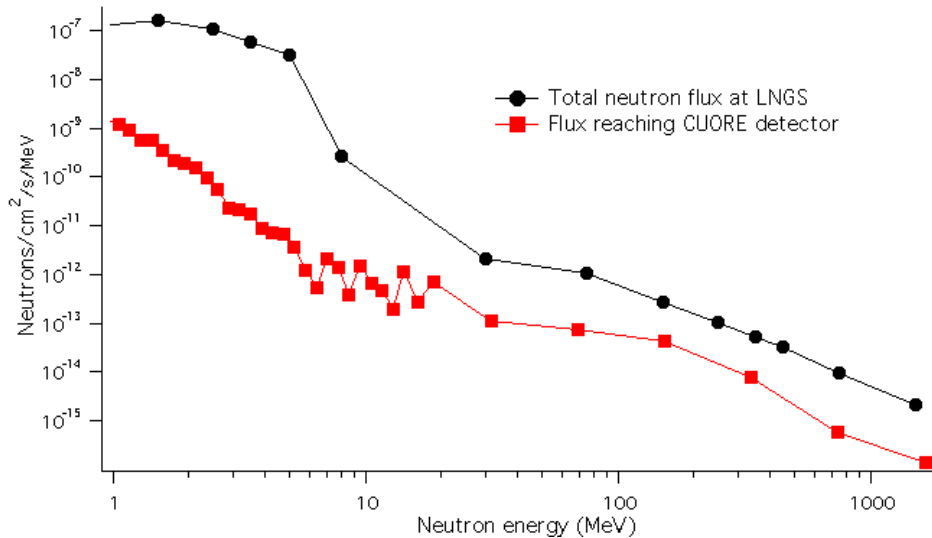


Figure 5.2. Black: The neutron flux as a function of energy at LNGS, used as an input to CUORE neutron simulations. Red: The FLUKA simulated neutron flux that reaches the CUORE detector, after propagation through CUORE shielding materials (including 17 cm polyethylene plus 3 cm borated (5%) polyethylene neutron shielding).

A combination FLUKA + GEANT4 simulation has been carried out in Rome and Milan for the CUORE detector [61]. FLUKA was used to propagate the neutrons through the shielding materials, while GEANT4 was used for modeling the detector itself. Unfortunately, the approach does not preserve the correlations between particles and γ -rays generated in a single event. These correlations would help to reject such background events through the application of an anti-coincidence cut, which rejects events in which multiple channels trigger simultaneously. It is likely that the simulations underestimate the effectiveness of the anticoincidence cut.

The spectrum used for these simulations was compiled from both low energy measurements [62, 63] and simulations [3, 64] made for LNGS. To be conservative, the higher value was always used. The LNGS neutron spectrum used in the CUORE simulations is shown in figure 5.2. The total neutron flux is $(3.7 \pm 0.2) \times 10^{-6}$ n/cm²/s.

The FLUKA simulations used a simplified detector geometry, shown in figure 5.3. The geometry included 20 cm of octagonal neutron shielding, 25 cm of octagonal lead shielding

Table 5.1. Transitions in Te at the 0ν DBD region of interest [65, 66].

Isotope	J^π	E_x (keV)	E_γ (keV)	E_f (keV)	BR (%)
^{122}Te	2^+	3094.60(6)	2530.3(12)	564	5.6(5)
^{126}Te	3	3195.17(7)	2528.85(7)	666	100

plus top ring, the 37 cm top and 6 cm cylindrical internal lead shields, and the copper cryostat structure. Different neutron shielding materials were tested. The neutron flux was generated with an isotropic distribution on a cylindrical surface surrounding the detector and shielding materials.

After propagation through the shielding material, the total neutron flux incident on the CUORE detector was reduced (see figure 5.2). The simulated background spectrum indicates that the background in the 0ν DBD region due to neutrons will be negligible. For the case discussed here, with 17 cm of polyethylene plus 3 cm borated (5%) polyethylene, the total simulated background in the 0ν DBD region of interest is only $(2.1 \pm 0.2) \times 10^{-5}$ counts/keV/kg/year, after the anti-coincidence cut is made. However, these simulations include cross sections for neutron reactions at energies that have never been measured in the laboratory. In order to trust the output of the Monte Carlo simulations, it is important to measure the cross sections for the reactions of interest.

5.1.2 Backgrounds from Te + n reactions

The question that we are trying to answer is what kinds of backgrounds we can expect to produce when neutrons interact directly with the crystals. For this reason, we wanted to measure the neutron cross sections on Te isotopes over a broad range of neutron energies. In particular, we are concerned with reactions that could deposit energy in the 2530 keV region, which is the Q-value of ^{130}Te decay and the location of the 0ν DBD peak. Transitions at this energy have been observed in $(n,n'\gamma)$ reactions on both ^{122}Te and ^{126}Te (see table 5.1), but the γ -ray production cross sections have never been measured for these transitions [65, 66].

If a peak were observed at the 0ν DBD energy, it is essential that other possible sources of a peak at that energy could be excluded. As a result, it is imperative that we know the

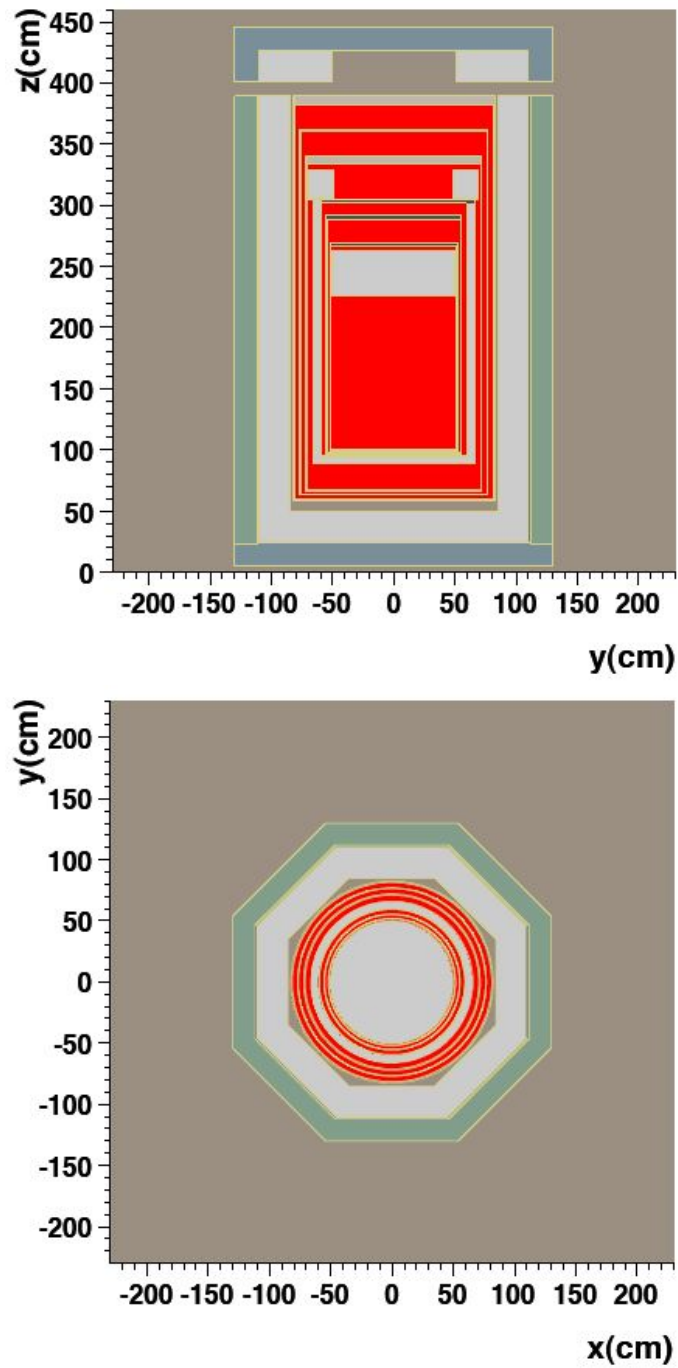


Figure 5.3. Side and top view of CUORE geometry implemented for FLUKA. The materials are indicated by color: dark gray = air, green = polyethylene, blue - borated polyethylene, light gray = lead, yellow = copper, and red = vacuum.

production cross sections for these γ -rays for inclusion in CUORE simulation codes. The Germanium Array for Neutron Induced Excitations (GEANIE) at the Los Alamos Neutron Science Center (LANSCE) is an ideal facility to carry out a study of neutron interactions on the stable isotopes of Te over a broad energy range.

5.2 The Los Alamos Neutron Science Center

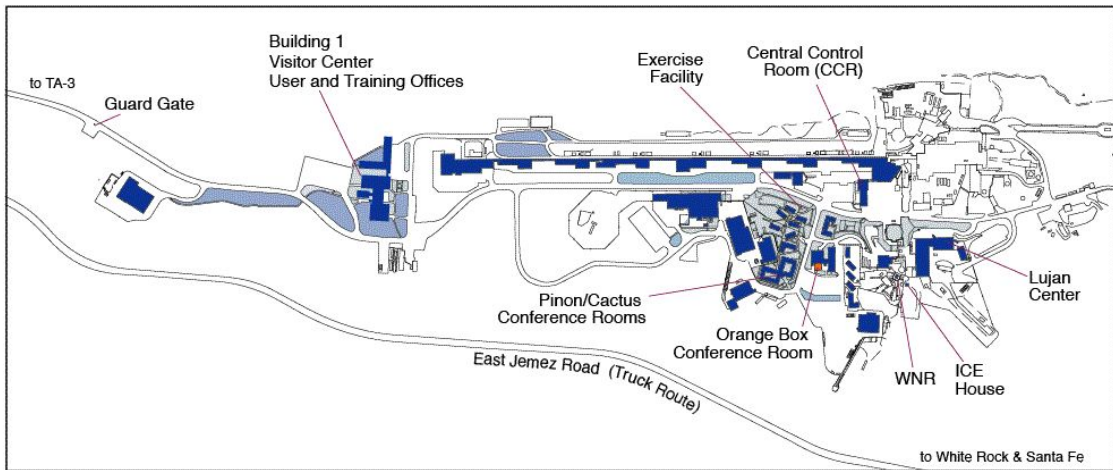


Figure 5.4. Layout of the Los Alamos Neutron Science Center. The GEANIE detector is located in the Weapons Neutron Research facility (WNR).

LANSCE is a user facility at Los Alamos National Laboratory. The layout of the facility is shown in figure 5.4. The LANSCE neutron source consists of a pulsed 800 MeV proton beam incident on a water-cooled tungsten target. The resulting spallation neutrons are collimated and sent to several different experimental areas, with neutron energy spectrum varying depending on the angle of the neutron beamline with respect to the proton beam. The beam timing structure consists of micropulses spaced $1.8 \mu\text{s}$ apart and grouped into macropulses $625 \mu\text{s}$ long. The neutron energy is determined by time of flight. The neutron flux as a function of energy on the 60R beamline (60° to the right of the proton beam) can be seen in figure 5.5.

LANSCE hosts a variety of detectors for basic and applied nuclear science. The DANCE array is the newest addition, a 4π array of barium fluoride crystals designed to study neutron

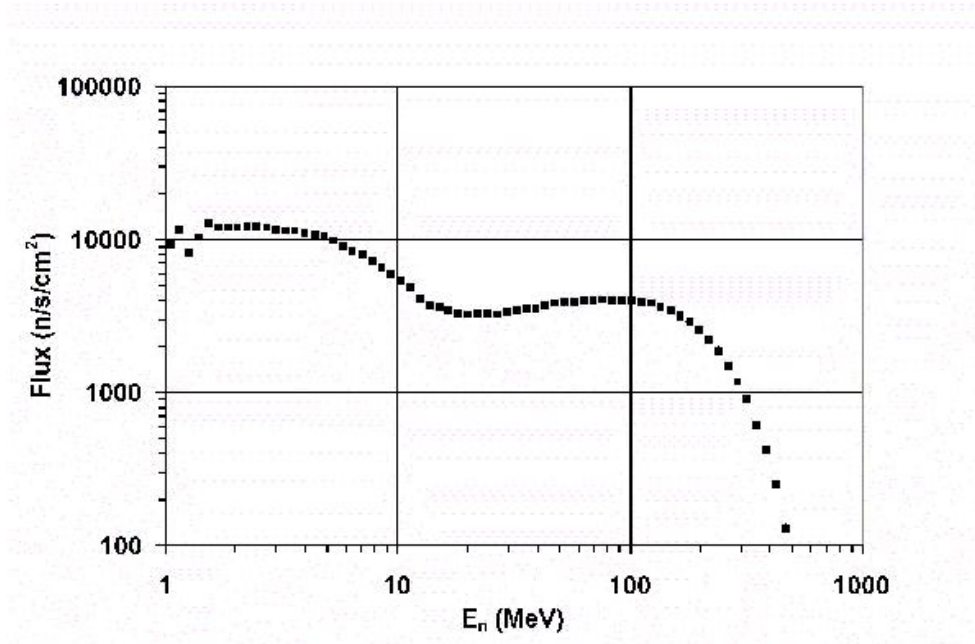


Figure 5.5. Neutron flux per 10% energy bin for the 60R beamline at LANSCE. Figure courtesy of the GEANIE collaboration.

capture reactions on small targets [67]. The FIGARO facility combines neutron and γ -ray detectors to studying neutron-induced reactions that produce both neutrons and γ -rays, such as fission [68]. In addition, the intense neutron flux in the “Blue Room” is used for studies of the target for the Spallation Neutron Source [69]. There is also a facility called the “Ice House,” in which the shape of the neutron spectrum is very similar to that of cosmic ray neutrons, and which is used by the semiconductor industry to test neutron-induced failures of devices due to single event upsets [70]. Finally, the GEANIE array is used for studies of neutron induced cross sections and nuclear structure.

5.3 The GEANIE detector

The Germanium Array for Neutron Induced Excitations (GEANIE) is located in the Weapons Neutron Research (WNR) facility at LANSCE. The detector is capable of acquiring high resolution prompt γ -ray spectra [71]. GEANIE was formerly the High Energy Resolution Array (HERA) [72], located at Lawrence Berkeley National Laboratory. The

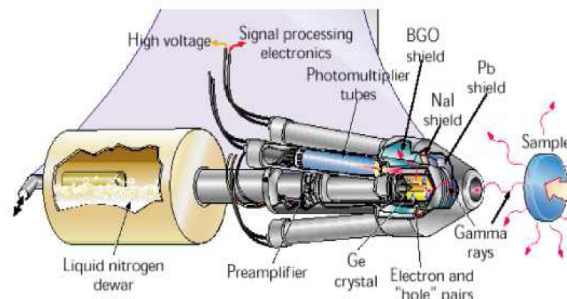


Figure 5.6. Top: Illustration of a single Compton suppressed HPGe detector. Bottom: Photograph of the GEANIE detector, with no target in place. The detector is a spherical arrangement of 26 individual HPGe detectors on the 60R beamline at LANSCE. Figures courtesy of the GEANIE collaboration.

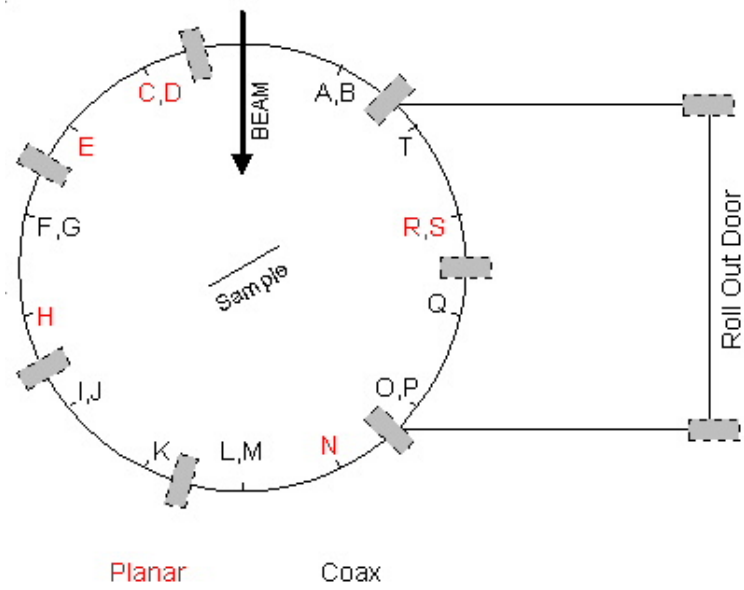
GEANIE detector is now located 20.34 m from the target on the 60R beamline at LANSCE. GEANIE consists of 26 high purity germanium (HPGe) ionization detectors. Eleven are planar detectors with good energy resolution at low γ -ray energies, but poor efficiency at higher energies. There are also fifteen coaxial detectors with better efficiency for higher γ -ray energies. The detectors are equipped with bismuth germinate (BGO) annular detectors to reject the Compton-scattering background (see figure 5.6). The angular positions of the detectors are shown in figure 5.7. The beam is monitored with a ^{235}U fission chamber and a ^{238}U fission chamber located upstream from the detector.

Because GEANIE is operated on a beamline with high neutron flux, the trigger rate in the array is high. The detector triggers are gated on the beam pulses. Detector and fission chamber livetimes are calculated by comparing the event rate at the ADC with the rate of a scaler. GEANIE allows the simultaneous measurement of neutron-induced cross sections over a wide range of neutron energies, from about 1 to 200 MeV, with a spectral shape similar to that expected underground. The neutron energies are calculated by time of flight. The timing electronics are shown in figure 5.8.

5.4 The ^{130}Te and ^{nat}Te experiments

In order to evaluate the neutron background for CUORE, we have used the GEANIE detector at WNR to observe the effects of neutrons over a wide range of energies on an unenriched Te (^{nat}Te) target. In addition, an isotopically enriched ^{130}Te target was run previously for studies of the (n,2n) reaction channel. The ^{130}Te target was run at GEANIE in January 2004, and I have analyzed the data from that experiment for the first time as part of this work. The details of the run are summarized in table 5.2.

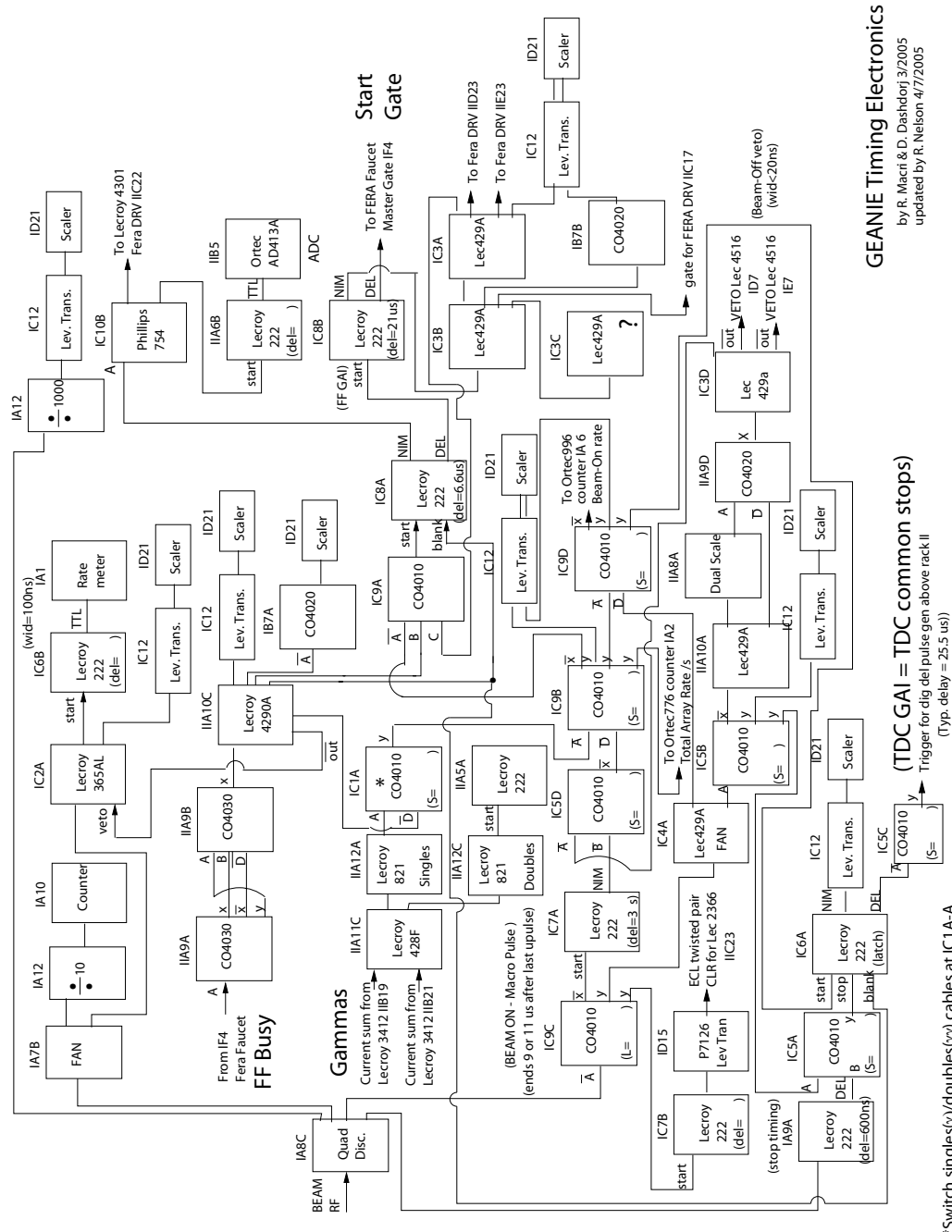
The targets for the ^{nat}Te experiment were discs of unenriched tellurium metal. The primary target was 0.25" thick and 1" in diameter, and a thin target (0.125" thick and 1.25" in diameter) was also used. We chose to use a target of natural isotopic composition to mimic the Te in the CUORE experiment. The measurement is made slightly more difficult by the presence of numerous stable Te isotopes (see table 5.3). The most significant



Detector	Φ	θ
A	28.0	154.3
B	-28.0	154.3
C	28.0	-154.3
D	-28.0	-154.3
E	0.0	-128.6
F	28.0	-102.9
G	-28.0	-102.9
H	0.0	-77.1
I	28.0	-51.4
J	-28.0	-51.4
K	0.0	-25.7
L	28.0	0.0
M	-28.0	0.0
N	0.0	25.7
O	28.0	51.4
P	-28.0	51.4
Q	0.0	77.1
R	28.0	102.9
S	-28.0	102.9
T	0.0	128.6

Φ + on top θ + Beam Left
 - underneath - Beam Right

Figure 5.7. Angles and positions of the Ge detectors in GEANIE. Figure courtesy of the GEANIE collaboration.



GEANIE Timing Electronics
 by R. Macri & D. Dashdorj 3/2005
 updated by R. Nelson 4/7/2005

Figure 5.8. Timing electronics for the GEANIE detector. Figure courtesy of the GEANIE collaboration.

Table 5.2. Experimental details for the ^{130}Te target.

Dates of experiment	January 9 - 15, 2004
Target	^{130}Te metal powder
Geometry	1" diameter holder
Mass	1.3002 g
Enrichment	$99.40 \pm 0.056\%$
Sample orientation	90°
Beam rep. rate	100 Hz
Micropulse spacing	$1.8 \mu\text{s}$
Beam gate length	$625 \mu\text{s}$
Typical proton current	4300 nA
Planar deadtime (sum)	0.87545 ± 0.00010
Coax deadtime (sum)	0.84759 ± 0.00013
^{238}U f.c. deadtime	0.82249 ± 0.00238
Fe foil run	January 15 - 20, 2004

Table 5.3. Natural isotopic abundance of Te [26].

Isotope	Natural isotopic abundance
^{120}Te	0.096(2) %
^{122}Te	2.603(4) %
^{123}Te	0.908(2) %
^{124}Te	4.816(6) %
^{125}Te	7.139(6) %
^{126}Te	18.95(1) %
^{128}Te	31.69(1) %
^{130}Te	33.80(1) %

backgrounds for neutrinoless double beta decay are expected to come from one of the three most abundant Te isotopes, ^{126}Te (18.95%), ^{128}Te (31.69%), and ^{130}Te (33.80%), which make up most of the active material in the CUORE detector. The data from the ^{130}Te run can be used to disentangle the more complicated natural Te data.

We took data with the ^{nat}Te target from 31 October to 6 November 2006 with a 0.75" beam spot and again from 15 to 23 December 2006 with a 0.5" beam spot. We measured the beam spot size using a photographic plate placed in the beamline (see figure 5.9). The smaller beam spot reduced the overall rate in the detector, which increased the live time and resulted in a spectrum with improved resolution (figure 5.10). As a result, only the data from the December run was used in the calculation of the cross sections. The experimental

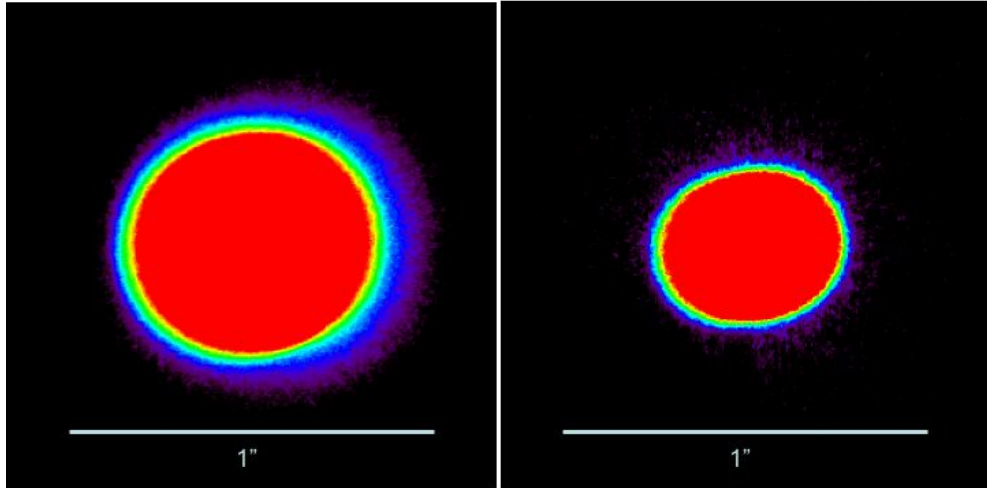


Figure 5.9. Left: Photographic plate image of beamspot from November 2006, with 0.75" collimation. Right: Image of beamspot from December 2006, with 0.5" collimation. The scale is 150 pixels/inch.

details of the December run are summarized in table 5.4. Details of the data analysis as well as the extracted γ -ray production cross sections will be discussed in chapter 6.

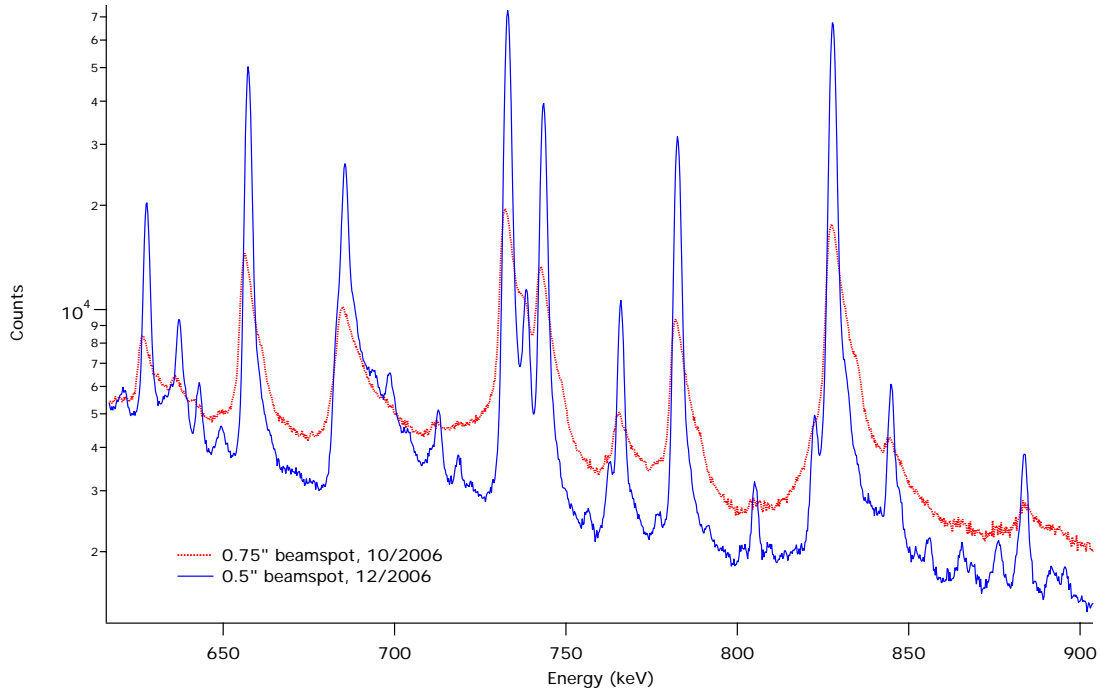


Figure 5.10. The summed coax spectra for neutrons with energies 3 - 10 MeV for the October 2006 run with 0.75" beam spot (red) and for the December 2006 run with 0.5" beam spot (blue). The smaller beam spot produces a better energy resolution because of the lower deadtime (and therefore reduced pileup). The region shown contains the first excited state (n,n' γ) transitions in ^{126}Te (666 keV), ^{128}Te (743 keV), and ^{130}Te (839 keV).

Table 5.4. Experimental details for the unenriched Te target.

Dates of experiment	December 15 - 23, 2006
Target	^{nat}Te pressed metal (95% normal density)
Mass	20.1419 g
Diameter	2.548 cm
Thickness	0.678 cm
Sample orientation	90°
Beam rep. rate	40 Hz
Micropulse spacing	1.8 μs
Beam gate length	625 μs
Typical proton current	1563 nA
Planar deadtime (sum)	0.83553 ± 0.00007
Coax deadtime (sum)	0.80690 ± 0.00005
^{238}U f.c. deadtime	0.689881 ± 0.00207
Fe foil run	none

Chapter 6

Analysis of GEANIE data

Analysis of GEANIE data requires combining energy and timing information from multiple germanium detectors, as well as the fission chambers that monitor the neutron flux. In addition, corrections must be made for detector dead times and efficiencies. I analyzed the data for the ^{130}Te and ^{nat}Te experiments using the XGAM software suite, which was developed by Walid Younes specifically for use with GEANIE data [73].

The analysis package includes the sorting algorithms, calibration program, and spectrum fitting program used to extract cross sections from GEANIE data. Data sorting involves correcting gain drift during data acquisition and gain and timing alignment of the individual detectors. The result is a spectrum summed over coaxial detectors and a spectrum summed over planar detectors. The summed spectra are fit with a complicated gamma ray spectrum and background model, calibrated, and sliced into neutron energy bins to generate the yield curves. Two uranium fission chambers in the beam provide a measurement of the neutron flux for the extraction of cross sections.

The partial γ -ray production cross sections are computed using equation 6.1 [74].

$$\sigma_{\gamma}(E_n) = \frac{\epsilon_{fc}}{\epsilon_{Ge}} \times \frac{LT_{fc}}{LT_{Ge}} \times \frac{1}{a_s} \frac{A_{\gamma}}{N_n}, \quad (6.1)$$

where ϵ_{fc} and ϵ_{Ge} are the fission chamber and Ge efficiencies, LT_{fc} and LT_{Ge} are the live-times, a_s is the areal number density of the target, A_{γ} is the γ -ray peak area, and N_n is the

number of neutron counts in the fission chamber. In this chapter I will describe the process of obtaining these cross sections from the raw data.

6.1 Raw data sorting

The data were sorted using the TSCAN program, along with a user subroutine written specifically to process GEANIE data [75]. The sort occurs in four steps, or “passes.” During pass 0, individual detector ADC and TDC spectra are generated with no gain correction. This allows inspection for manual alignment. Energy alignment was done by hand, using a two-point linear gain correction (although the software also has an automatic alignment function). The timing alignment is a simple offset correction used to align the individual detector timing spectra, and the program allows this to be done either manually or automatically. These corrections are applied during pass 1.

During pass 2, a dynamical gain correction algorithm is applied to correct for slow drift during the run. For the ^{nat}Te analysis, the dynamic gain correction algorithm had negligible effect on the energy resolution of the detectors, indicating that the gain did not drift over the course of the run. As a result, this step was omitted from the final analysis. Finally, pass 3 is the production sort, in which the parameters are checked for consistency and the final matrix is generated for analysis.

6.2 Analysis of the γ -ray spectra

The γ -ray spectra were fitted using the XGAM program. This program fits the entire selected range of the spectrum simultaneously, ensuring a continuous fit to the background. The fit combines a polynomial background with global peak fitting parameters. It can accommodate an unlimited number of peaks. The peak shape is a combination of a Gaussian, with Gaussian asymmetry, a step function, and high energy tails. The entire fit to the ^{nat}Te coaxial spectrum can be seen in appendix A, along with a detailed explanation of the

fitting functions used. The energy calibration was done using known peaks in the beam-on spectrum.

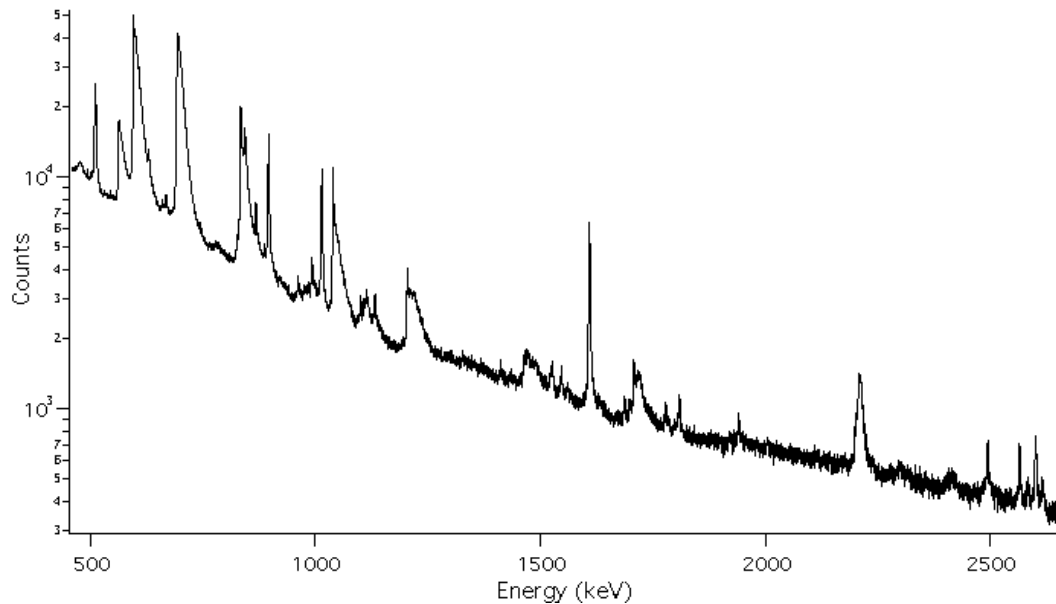


Figure 6.1. GEANIE coax spectrum with Be target. The Be target scatters neutrons into the Ge detectors, producing a spectrum which can be used to model neutron scattering peaks cleanly. In addition to the neutron inelastic scattering on Ge, other visible lines include the 511 keV annihilation peak, neutron inelastic scattering on ^{27}Al in the detector structure (1014 keV), and many peaks from neutron inelastic scattering on ^{209}Bi in the BGO detectors (896 keV and 1608 keV, for example).

A large source of background in the GEANIE detector is inelastic scattering of neutrons on the stable isotopes of Ge. Because these reactions contribute the energy of the γ -ray transition as well as the nuclear recoil in the detector, they result in large, asymmetric peaks with high-energy tails. In order to properly fit these peaks, I used a neutron scattering run, in which a beryllium target was run at GEANIE. The Be spectrum is shown in figure 6.1. The energies of the largest Ge inelastic scattering peaks are listed in table 6.1. In addition, other beam-related backgrounds are also visible in the Be data, including γ -rays from inelastic scattering on ^{27}Al , which encases the HP Ge detectors and makes up the GEANIE support structure, and ^{209}Bi , which is found in the BGO shields.

Figures 6.2 and 6.3 show the final fits to the region of 800 keV to 1000 keV for the coaxial detectors in four different runs. These runs are the beryllium neutron scattering

Table 6.1. Inelastic scattering peaks on the stable Ge isotopes. These produce background peaks from neutron reactions within the Ge detectors. The asymmetric shape of these background peaks is caused by nuclear recoils in the detectors, producing a high energy tail.

Reaction	E_γ
$^{70}\text{Ge}(n,n'\gamma)$	1039 keV
$^{72}\text{Ge}(n,n'\gamma)$	690 keV
$^{72}\text{Ge}(n,n'\gamma)$	834 keV
$^{74}\text{Ge}(n,n'\gamma)$	596 keV
$^{74}\text{Ge}(n,n'\gamma)$	1204 keV
$^{76}\text{Ge}(n,n'\gamma)$	563 keV

run, the $^{130}\text{Te} + \text{Fe}$ normalization run, and the ^{130}Te and ^{nat}Te production runs. The fit to the beryllium data is used to set the peak shape parameters for inelastic scattering on Ge isotopes and to identify beam related backgrounds. The fit to the $^{130}\text{Te} + \text{Fe}$ data is used to normalize the ^{130}Te cross sections. The fits to the four spectra are in good agreement, although the individual fits do vary according to the dead times and detector configurations of the different runs, which can change the peak shape parameters.

6.3 The time-of-flight technique

The neutron energies are calculated by time of flight. When the proton beam impacts on the spallation target, a large number of photons are produced, called the γ -flash. For a given neutron energy E_n , the arrival of the neutron-induced signal (t_{signal}) after the γ -flash (t_γ) is given by equation 6.2 [73].

$$t_{signal} - t_\gamma = \frac{d}{c} \left(\frac{E_n + m_n}{\sqrt{E_n^2 + 2m_n E_n}} - 1 \right), \quad (6.2)$$

where $d = 20.34$ m, times are measured in ns, and energies are measured in MeV. The time of flight spectrum for the ^{130}Te coax detectors is shown in figure 6.4.

Using the time of flight, matrices are sliced into neutron energy bins in order to extract excitation functions. For each neutron energy bin, the γ -ray spectrum is re-fit. The background and peak heights are allowed to vary, while the peak centroids and global peak shape parameters remain fixed. The fits to the ^{nat}Te coaxial detector sum spectra in the 839 keV region at six different neutron energies are shown in figure 6.5.

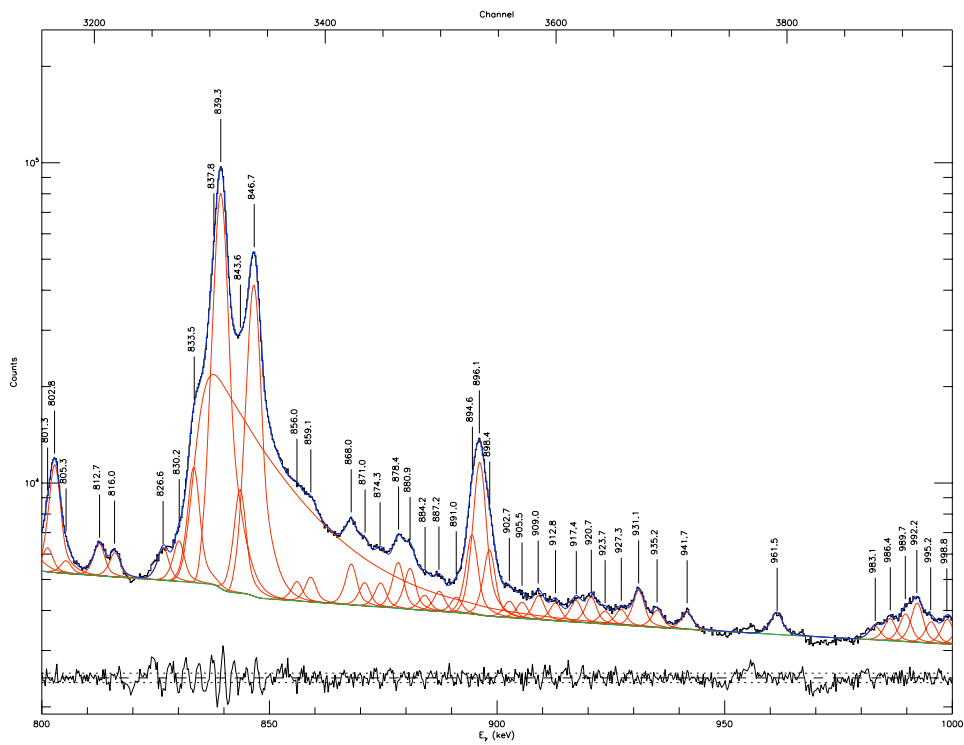
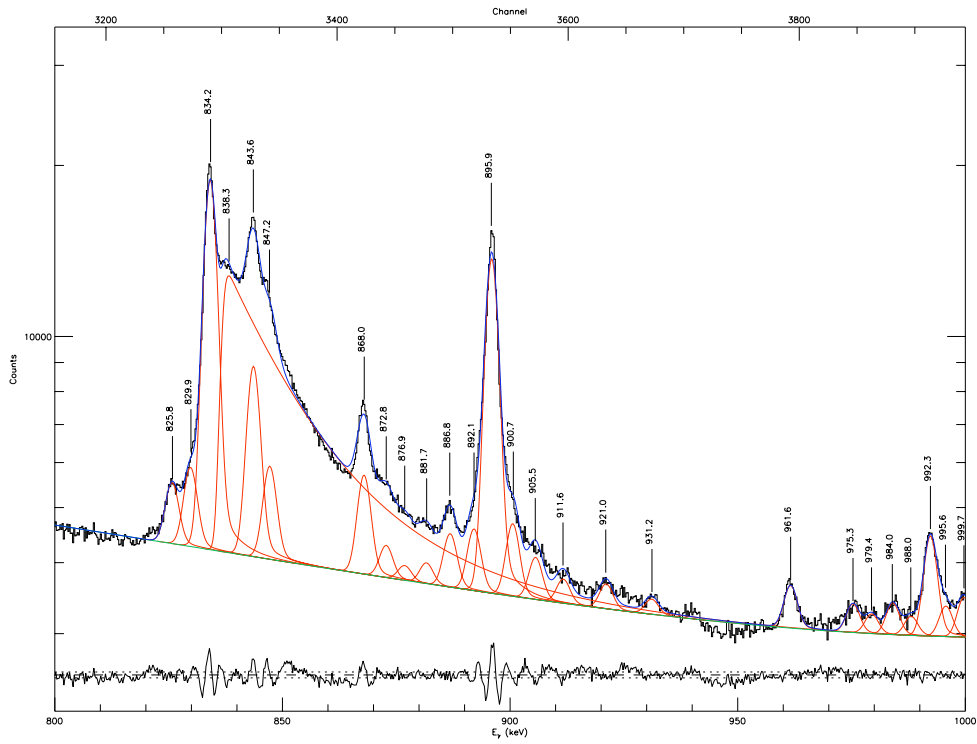


Figure 6.2. Fits to coaxial sum spectra for the beryllium neutron scattering run (top) and $^{130}\text{Te} + \text{Fe}$ run (bottom). Both spectra are summed over neutron energies in the range 1 MeV to 250 MeV.

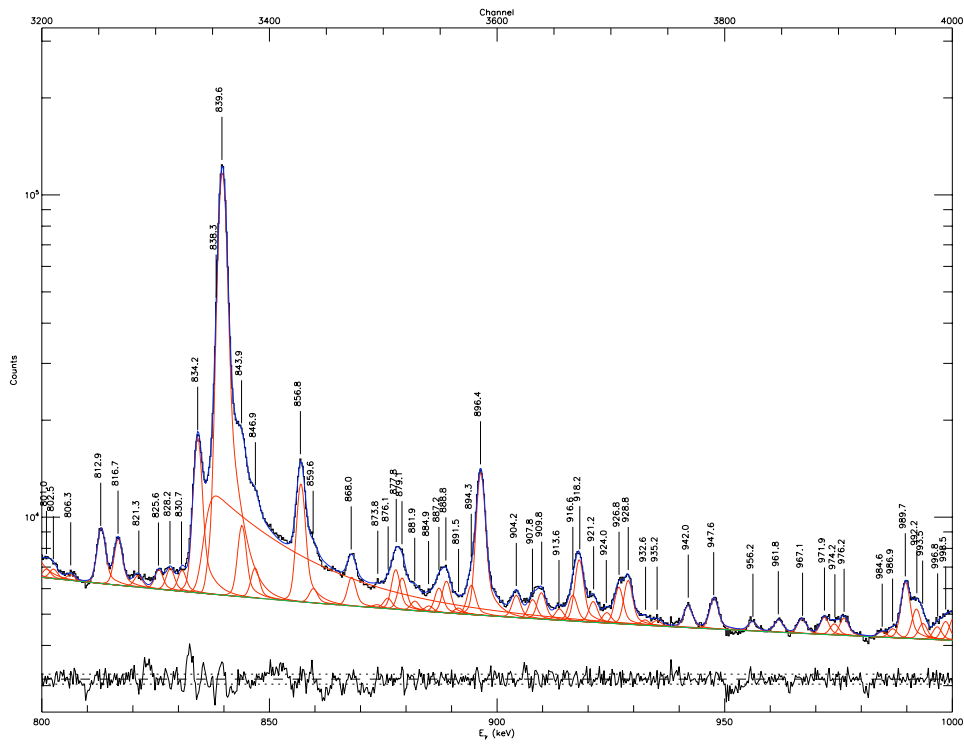
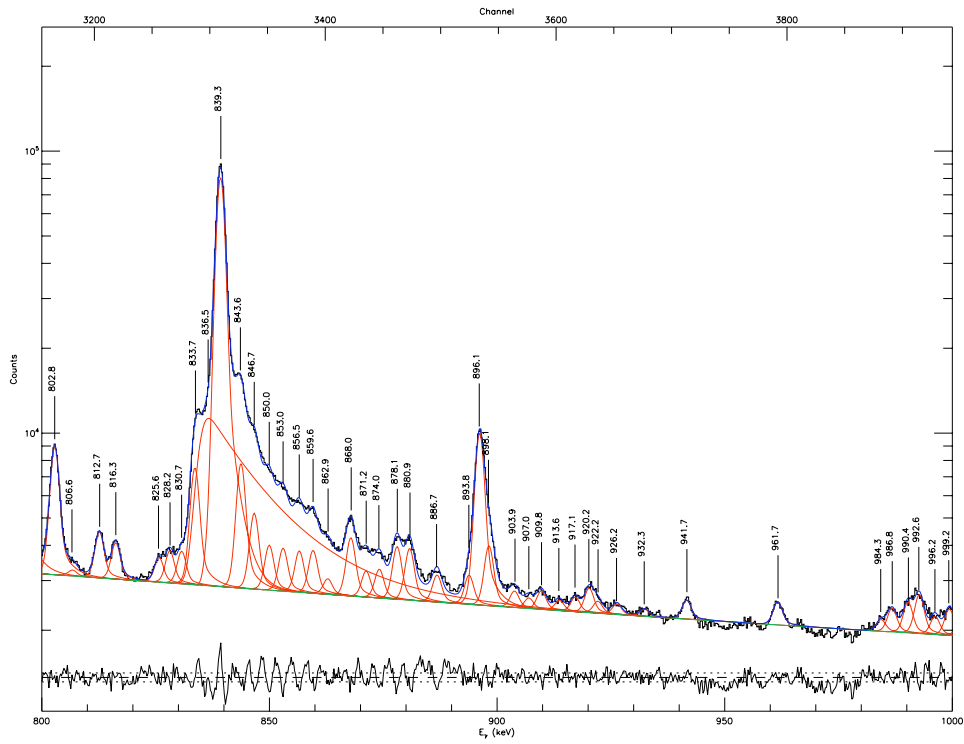


Figure 6.3. Fits to coaxial sum spectra for the ^{130}Te run (top) and ^{nat}Te run (bottom). Both spectra are summed over neutron energies in the range 1 MeV to 250 MeV.

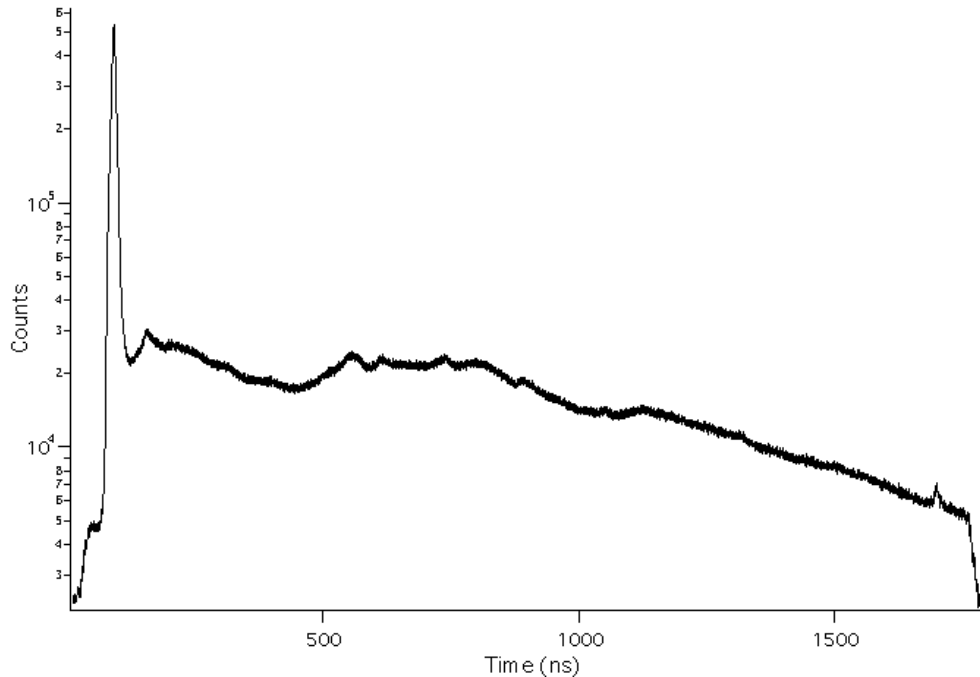


Figure 6.4. Time of flight spectrum for coax detectors during the ^{130}Te measurement. The sharp peak indicates the γ flash. Time of flight is measured relative to the centroid of this peak.

6.4 Beam monitoring

In order to convert excitation functions into partial γ -ray production cross sections, it is necessary to know the neutron beam flux. In order to monitor the neutron beam, a ^{235}U fission chamber and a ^{238}U fission chamber are located upstream from the GEANIE detector. For this analysis, only data from the ^{238}U fission chamber was used. The fission chamber time of flight spectrum is used to calculate the beam current as a function of neutron energy. In the fission chamber energy spectrum, there is a high energy continuum due to the sum of the energies of the two fission fragments. At low energy, there is a large excess of counts due to both the random α -decay events and the large knockout proton background [76]. A cut is made in the fission chamber energy spectrum at the minimum between the two peaks in order to cut out the background from α -decays and protons. The energy spectrum and the time of flight spectra before and after the energy cut are shown in figure 6.6.

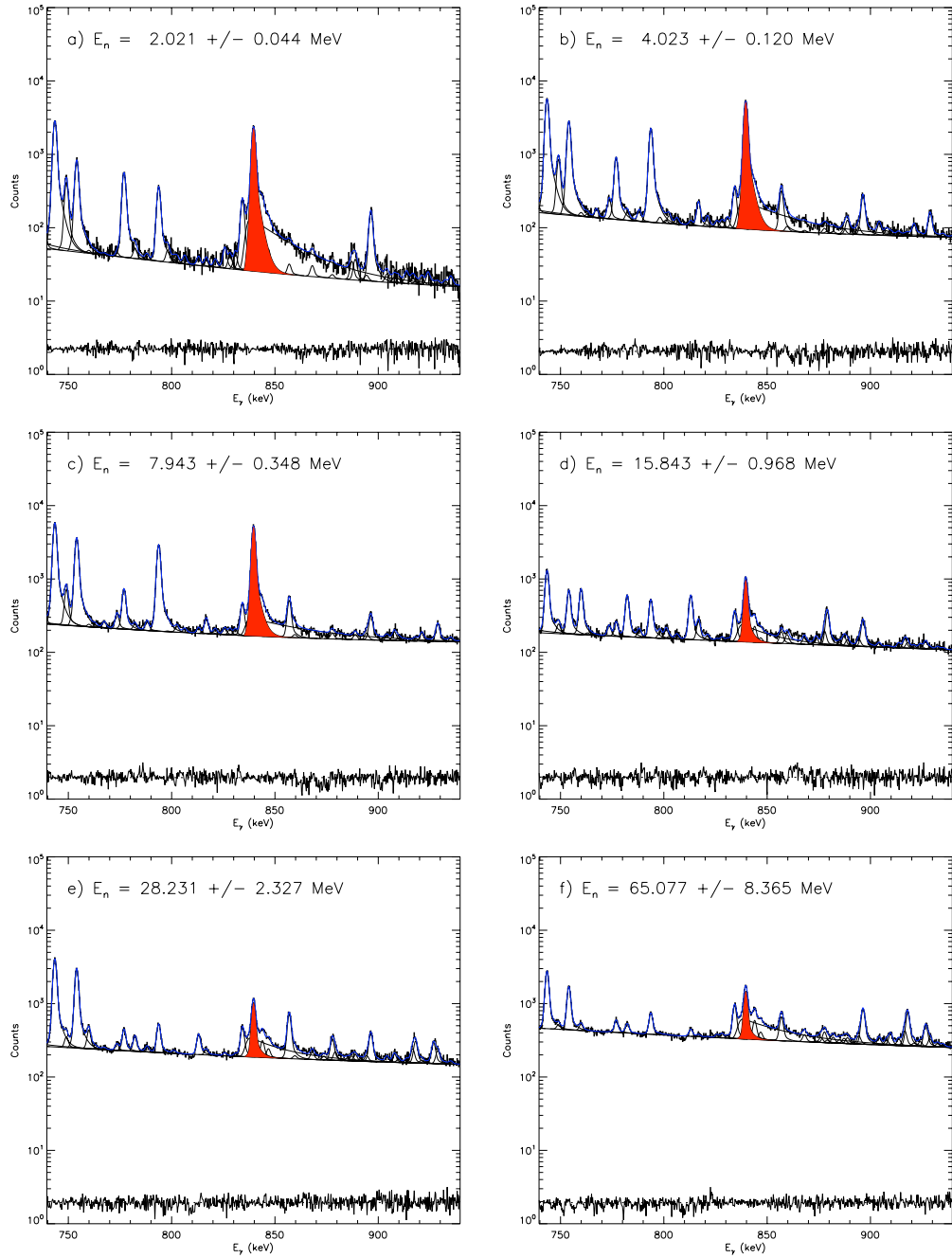


Figure 6.5. The fits to the ^{nat}Te coaxial detector sum spectra in the 839 keV region for six different neutron energy bins. The 839.5 keV transition in ^{130}Te is highlighted.

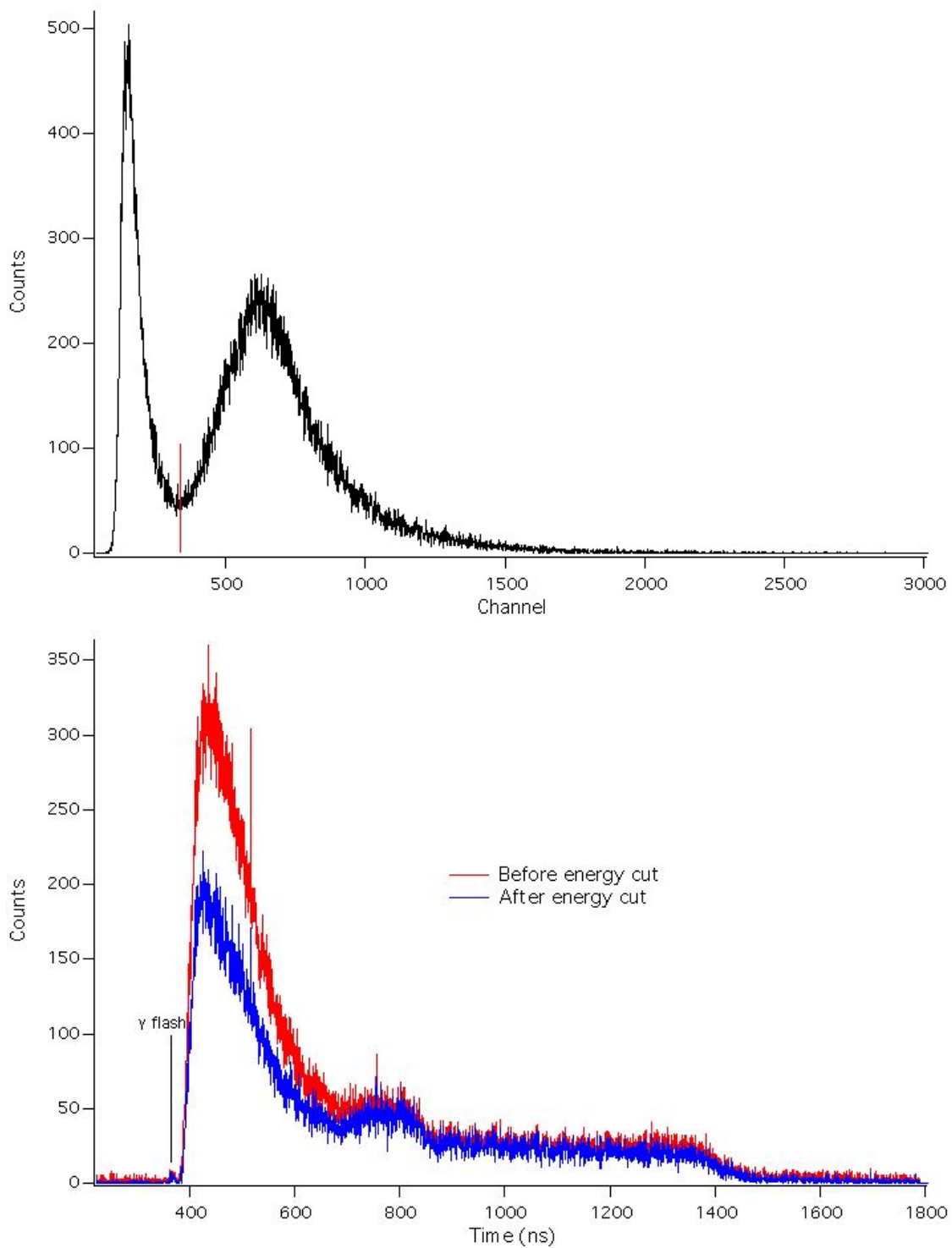


Figure 6.6. Top: Fission chamber energy spectrum. The vertical red line indicates the energy cut that is made to eliminate the α -decay and proton backgrounds. Bottom: fission chamber time of flight spectrum, shown before and after the energy cut is applied. The time of flight is measured from the γ -flash, indicated.

Because the fission spectrum also extends into the energy region that is removed in the cut, there is some reduction in the efficiency of the fission chamber due to the energy cut. The fission chamber efficiency ϵ_{fc} is calculated to be 0.941 ± 0.004 [76]. This includes the effect of the cut on the fission chamber energy spectrum as well as the loss of fission fragments that do not escape the uranium foil.

6.5 Detector efficiencies and uncertainties

In order to measure the Ge detector efficiencies, an external ^{152}Eu calibration source was used. The efficiency curve was then normalized through the analysis of the 847 keV ^{56}Fe line. During part of the ^{130}Te run, two 0.005" thick Fe foils were placed in the beam, immediately upstream from the target. The 847 keV partial γ -ray cross section has been measured at GEANIE to be 705 ± 56 mb at a neutron energy of 14.5 MeV [77]. The ratio of the 847 keV line in the $^{130}\text{Te} + \text{Fe}$ data to the known cross section gives the Ge detector efficiency at 847 keV. For the coaxial detectors, this is found to be $(0.656 \pm 0.053)\%$, and for the planar detectors it is found to be $(0.308 \pm 0.025)\%$. The relative efficiencies measured for the ^{130}Te run are shown in figure 6.7. The corrected 839 keV γ cross section from the ^{130}Te target run was then used to correct the ^{nat}Te efficiency in the same way. In this case, because there were only four coaxial detectors included in the analysis, the efficiency of the coaxial detectors at 839 keV was found to be $(0.260 \pm 0.002)\%$, including only the relative errors.

Because the ^{130}Te target was thin, the correction due to photon absorption in the target is small. For a detector perpendicular to the target surface, assuming that the γ -rays are emitted uniformly throughout the thickness of the target and ignoring the areal distribution of the beam profile, the ratio of the number of γ -rays emitted $N_{\gamma emit}$ to the number of γ -rays that escape the target $N_{\gamma escape}$ is given by equation 6.3 [76].

$$A_{attenuation} = \frac{N_{\gamma emit}}{N_{\gamma escape}} = \frac{\mu a_s}{1 - \exp(-\mu a_s)}, \quad (6.3)$$

where μ is the attenuation coefficient and a_s is the areal density of the target. Table 6.2 summarizes the estimated correction due to photon absorption for both targets at several

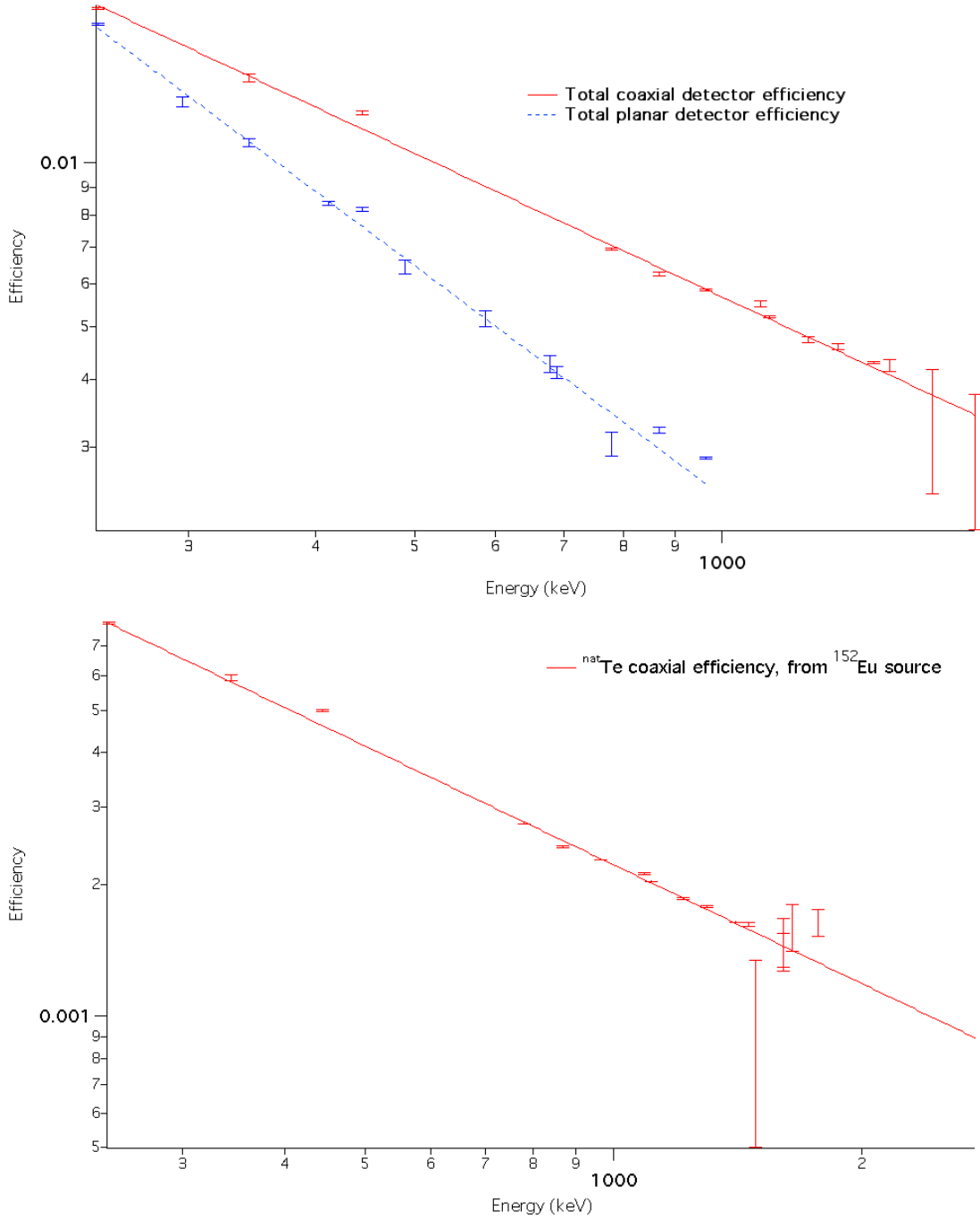


Figure 6.7. Top: Total detector efficiencies measured using a ^{152}Eu source for the planar and coaxial detectors for the ^{130}Te run. The fit is given by the equation: $\epsilon = \exp(a + b \log(E_\gamma))$. The efficiency was normalized at 847 keV using the ^{56}Fe target data. Bottom: The total coaxial detector efficiency curve for the ^{nat}Te run, measured using ^{152}Eu source data and normalized to the ^{130}Te experiment data at 839 keV.

Table 6.2. Photon attenuation factors for both targets at several γ -ray energies. Attenuation coefficients μ are from the NIST Photon Cross Sections Database, XCOM [78].

E_γ (keV)	μ (b/atom)	Attenuation factor	
		^{130}Te attenuation factor $a_s = 0.001189$ atoms/b	^{nat}Te attenuation factor $a_s = 0.01864$ atoms/b
181	82.3	1.05	1.96
468	19.8	1.01	1.20
839	13	1.01	1.13
2607	7.82	1.00	1.07

different γ -ray energies. As the table shows, the photon absorption correction for the ^{nat}Te target, which was significantly thicker, is not small. While an explicit correction is not included in this analysis, the effect is mitigated by the manner in which the efficiency normalization was performed. Because the detector efficiency was normalized at 839 keV for the ^{nat}Te experiment, the photon absorption correction at 839 keV is already taken into account. At lower γ -ray energies, the measured cross sections will be suppressed (by as much as 6% at 500 keV), while at higher energies it will be enhanced (by as much as 5% at 2.6 MeV).

Angular distributions were not taken into account in the evaluation of cross-sections. Angular distribution effects arise from the fact that the incoming neutron beam partially aligns the nuclear spins of the decaying nuclei produced in the target. The corrections due to angular distributions have been explored previously in the case of ^{235}U . Angular distribution effects can be modeled, but even for a fully aligned, stretched transition (for which $\Delta J = L$, where L is the multipole of the transition), the correction is expected to be less than 15% [74]. For neutron energies much above the threshold for the reaction, the alignment will be reduced by the number of decay paths to the final state that proceed through unstretched transitions, and the effect will tend to decrease.

6.6 Cross sections

Some of the open reaction channels for $^{130}\text{Te} + n$, $^{128}\text{Te} + n$, and $^{126}\text{Te} + n$, along with Q-values and thresholds, are shown in tables 6.3, 6.4, and 6.5, respectively. The Q-values and thresholds were calculated with the web-based program QTOOL [79]. In general, the

product nuclei will be produced in an excited state, which will then decay by γ -ray emission. These tables will help to identify the γ -ray peaks, both by the de-excitation energies of the product nuclei and by the neutron energy thresholds for the reactions.

Table 6.3. Q-values and thresholds for some $^{130}\text{Te} + \text{n}$ products [79].

Target	Products	Q-value (MeV)	Threshold (MeV)
^{130}Te	$^{131}\text{Te} + \gamma$	5.92975	0
^{130}Te	$^{127}\text{Sn} + \alpha$	1.80101	0
^{130}Te	$^{130}\text{Te} + \text{n}$	0	0
^{130}Te	$^{126}\text{Sn} + \text{n} + \alpha$	-3.75809	3.78727
^{130}Te	$^{130}\text{Sb} + \text{p}$	-4.17667	4.2091
^{130}Te	$^{123}\text{Cd} + 2 \alpha$	-6.82092	6.87388
^{130}Te	$^{129}\text{Sb} + \text{d}$	-7.79126	7.85176
^{130}Te	$^{129}\text{Te} + 2 \text{n}$	-8.41869	8.48406
^{130}Te	$^{128}\text{Sb} + \text{t}$	-9.6214	9.69611
^{130}Te	$^{129}\text{Sb} + \text{n} + \text{p}$	-10.01585	10.09361
^{130}Te	$^{128}\text{Sn} + ^3\text{He}$	-10.87675	10.96121
^{130}Te	$^{126}\text{In} + \text{p} + \alpha$	-11.1828	11.26963
^{130}Te	$^{125}\text{Sn} + 2 \text{n} + \alpha$	-11.95148	12.04428
^{130}Te	$^{129}\text{Sn} + 2 \text{p}$	-13.22952	13.33224
^{130}Te	$^{125}\text{In} + \text{d} + \alpha$	-14.36259	14.47411
^{130}Te	$^{128}\text{Te} + 3 \text{n}$	-14.50207	14.61467
^{130}Te	$^{126}\text{Te} + 5 \text{n}$	-29.56816	29.79774

Some selected cross sections from the ^{130}Te and ^{nat}Te runs follow. In order to better show the details of the excitation functions, the error bars represent relative errors in the excitation function rather than the error in the absolute cross section measurement, as discussed in section 6.5. For the ^{nat}Te analysis, I have not made the correction for the isotopic abundance, as noted in the figure captions. Additional measured cross sections for (n,n' γ) reactions on the stable Te isotopes can be found in appendix B.

While we were not able to obtain a positive measurement of the gamma production cross section for the 2529 keV transition in ^{126}Te , we can be sure that this cross section is small. The region of the spectrum where we search for this transition is shown in figure 6.13, for neutron energies in the range of 3 MeV to 20 MeV. For this neutron energy range, the main open reaction channel is $^{126}\text{Te}(\text{n},\text{n}'\gamma)$, and I have corrected for the natural isotopic abundance of ^{126}Te . The corresponding upper limit on the 2529 keV average γ -ray production cross section is $\sigma_{2529\text{keV}} < 3.1 \text{ mb}$ at 95% confidence level. The limit on the

Table 6.4. Q-values and thresholds for some $^{128}\text{Te} + \text{n}$ products [79].

Target	Products	Q-value (MeV)	Threshold (MeV)
^{128}Te	$^{129}\text{Te} + \gamma$	6.08337	0
^{128}Te	$^{125}\text{Sn} + \alpha$	2.55058	0
^{128}Te	$^{128}\text{Te} + \text{n}$	0	0
^{128}Te	$^{124}\text{Sn} + \text{n} + \alpha$	-3.18246	3.20756
^{128}Te	$^{128}\text{Sb} + \text{p}$	-3.60123	3.62963
^{128}Te	$^{121}\text{Cd} + 2 \alpha$	-4.71393	4.7511
^{128}Te	$^{127}\text{Sb} + \text{d}$	-7.34956	7.40752
^{128}Te	$^{126}\text{Sb} + \text{t}$	-9.4744	9.54911
^{128}Te	$^{127}\text{Sb} + \text{n} + \text{p}$	-9.57416	9.64966
^{128}Te	$^{124}\text{In} + \text{p} + \alpha$	-9.76016	9.83713
^{128}Te	$^{126}\text{Sn} + {}^3\text{He}$	-9.83382	9.91137
^{128}Te	$^{120}\text{Cd} + \text{n} + 2 \alpha$	-9.87061	9.94845
^{128}Te	$^{123}\text{Sn} + 2 \text{n} + \alpha$	-11.67049	11.76252
^{128}Te	$^{117}\text{Pd} + 3 \alpha$	-11.84776	11.94119
^{128}Te	$^{127}\text{Sn} + 2 \text{p}$	-11.99282	12.0874
^{128}Te	$^{123}\text{In} + \text{d} + \alpha$	-13.05746	13.16044
^{128}Te	$^{122}\text{In} + \text{t} + \alpha$	-14.7208	14.83689
^{128}Te	$^{126}\text{Te} + 3 \text{n}$	-15.06609	15.18491
^{128}Te	$^{124}\text{Te} + 5 \text{n}$	-30.7561	30.99864

 Table 6.5. Q-values and thresholds for some $^{126}\text{Te} + \text{n}$ products [79].

Target	Products	Q-value (MeV)	Threshold (MeV)
^{126}Te	$^{127}\text{Te} + \gamma$	6.29059	0
^{126}Te	$^{123}\text{Sn} + \alpha$	3.3956	0
^{126}Te	$^{126}\text{Te} + \text{n}$	0	0
^{126}Te	$^{122}\text{Sn} + \text{n} + \alpha$	-2.55032	2.57075
^{126}Te	$^{126}\text{Sb} + \text{p}$	-2.89019	2.91334
^{126}Te	$^{119}\text{Cd} + 2 \alpha$	-2.94226	2.96583
^{126}Te	$^{125}\text{Sb} + \text{d}$	-6.87366	6.92873
^{126}Te	$^{122}\text{In} + \text{p} + \alpha$	-8.1366	8.20178
^{126}Te	$^{118}\text{Cd} + \text{n} + 2 \alpha$	-8.21128	8.27707
^{126}Te	$^{124}\text{Sn} + {}^3\text{He}$	-8.69415	8.76381
^{126}Te	$^{115}\text{Pd} + 3 \alpha$	-8.87041	8.94148
^{126}Te	$^{125}\text{Sb} + \text{n} + \text{p}$	-9.09826	9.17115
^{126}Te	$^{124}\text{Sb} + \text{t}$	-9.33023	9.40498
^{126}Te	$^{125}\text{Sn} + 2 \text{p}$	-10.67923	10.76479
^{126}Te	$^{121}\text{Sn} + 2 \text{n} + \alpha$	-11.36385	11.45489
^{126}Te	$^{121}\text{In} + \text{d} + \alpha$	-11.72147	11.81538
^{126}Te	$^{120}\text{In} + \text{t} + \alpha$	-13.6405	13.74977
^{126}Te	$^{114}\text{Pd} + \text{n} + 3 \alpha$	-13.85099	13.96196
^{126}Te	$^{121}\text{In} + \text{n} + \text{p} + \alpha$	-13.94606	14.05779
^{126}Te	$^{124}\text{Te} + 3 \text{n}$	-15.69	15.8157
^{126}Te	$^{122}\text{Te} + 5 \text{n}$	-32.04478	32.30151

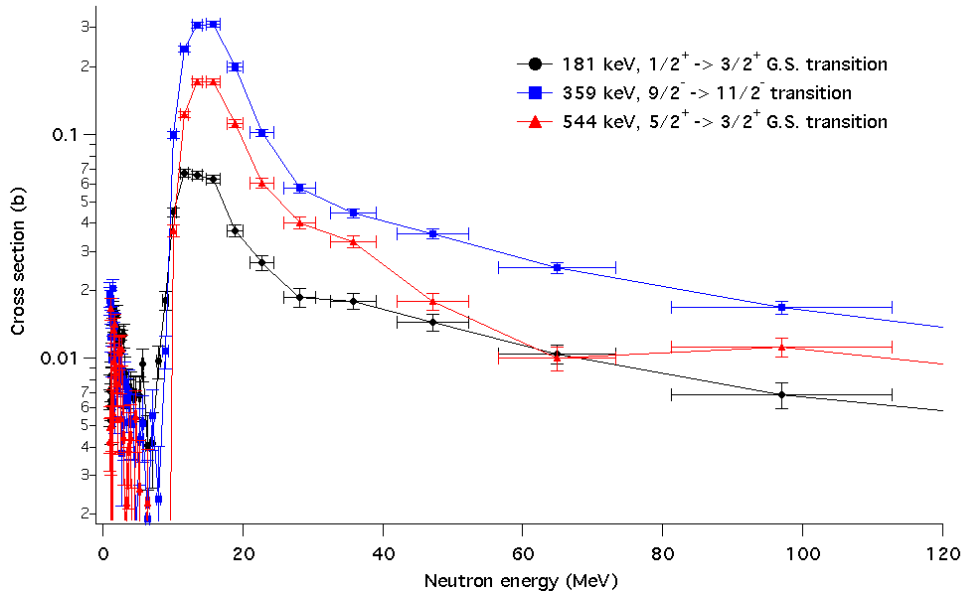


Figure 6.8. $^{130}\text{Te}(n,2n)^{129}\text{Te}$ γ -ray production cross sections for the γ -rays at 180.8 keV, 359.4 keV, and 544.7 keV obtained from the ^{130}Te target experiment. The 180.8 keV and 544.7 keV γ -rays indicate transitions to the ground state of ^{129}Te , while the 359.4 keV γ -ray is a transition to the ^{129m}Te isomer at 105.5 keV, which has a half-life of 33.6 days. (The connecting lines are there only to guide the eye.)

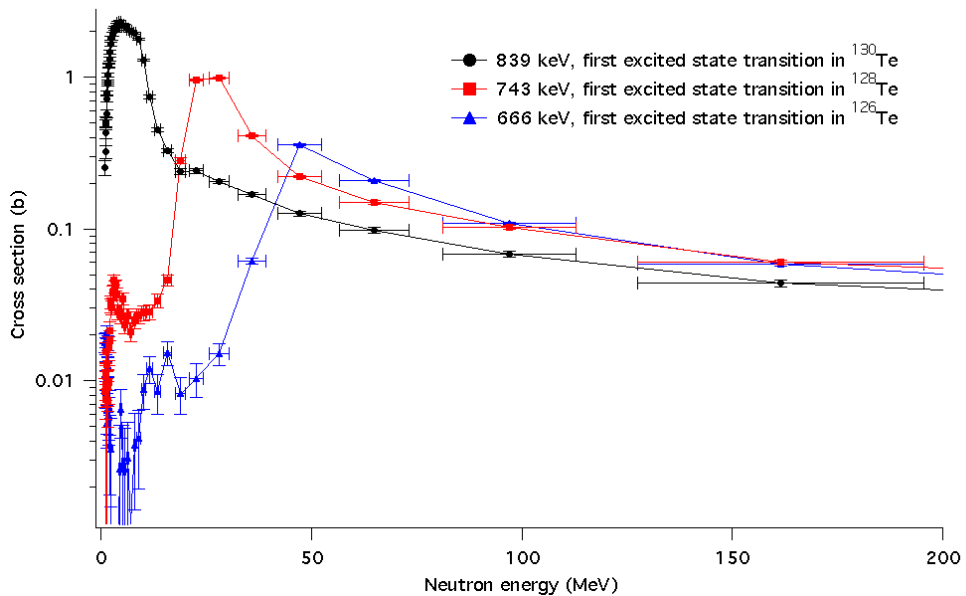


Figure 6.9. $^{130}\text{Te}(n,xn)$ cross sections for the ^{130}Te target experiment. The 839 keV line is produced through $^{130}\text{Te}(n,n'\gamma)^{130}\text{Te}$, the 743 keV line through $^{130}\text{Te}(n,3n)^{128}\text{Te}$, and the 666 keV line through $^{130}\text{Te}(n,5n)^{126}\text{Te}$. (The connecting lines are there only to guide the eye.)

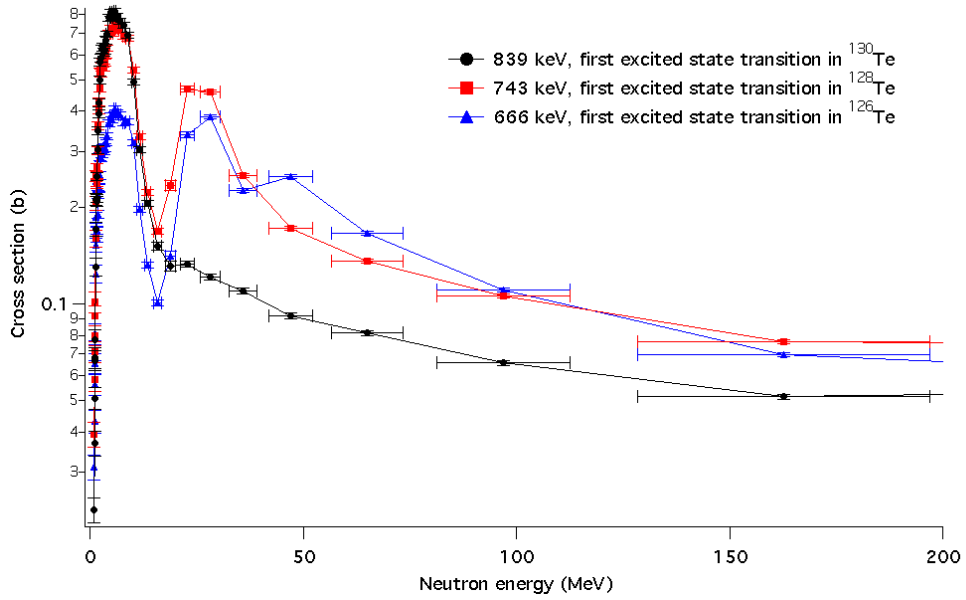


Figure 6.10. $^{nat}\text{Te}(n,xn)$ cross sections. The differing structure of the three cross sections indicates that the reactions on different isotopes are generating the same lines. For example, the 666 keV line is being produced through $^{126}\text{Te}(n,n'\gamma)$, $^{128}\text{Te}(n,3n)$, and $^{130}\text{Te}(n,5n)$. Note that the cross sections are for ^{nat}Te and have not been corrected for isotopic abundance. (The connecting lines are there only to guide the eye.)

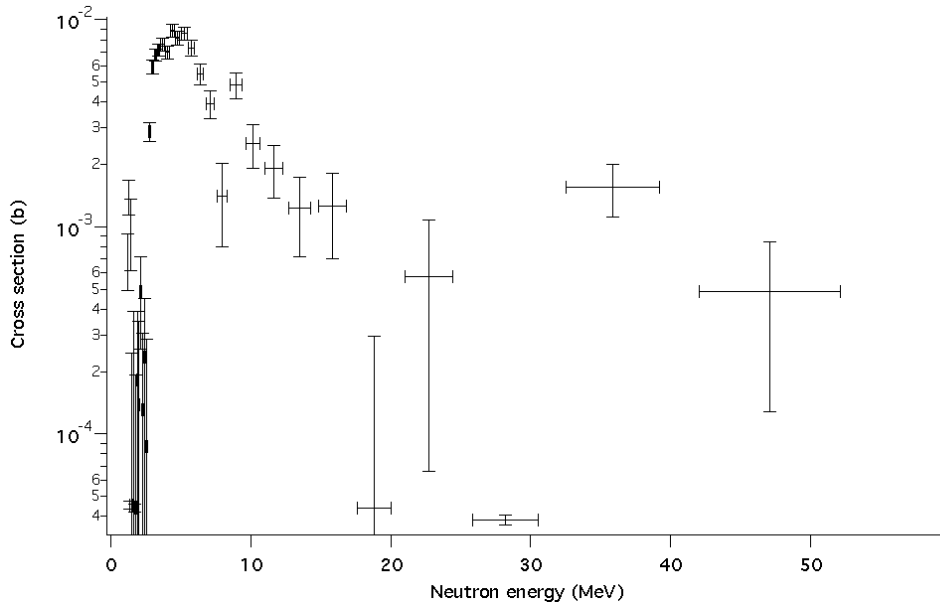


Figure 6.11. 2607 keV $^{130}\text{Te}(n,n'\gamma)$ γ -ray production cross section, from the ^{nat}Te experiment. This is the peak in the ^{nat}Te spectrum nearest to 2530 keV which cannot be attributed to beam-related backgrounds. The cross section has not been corrected for ^{130}Te natural isotopic abundance.

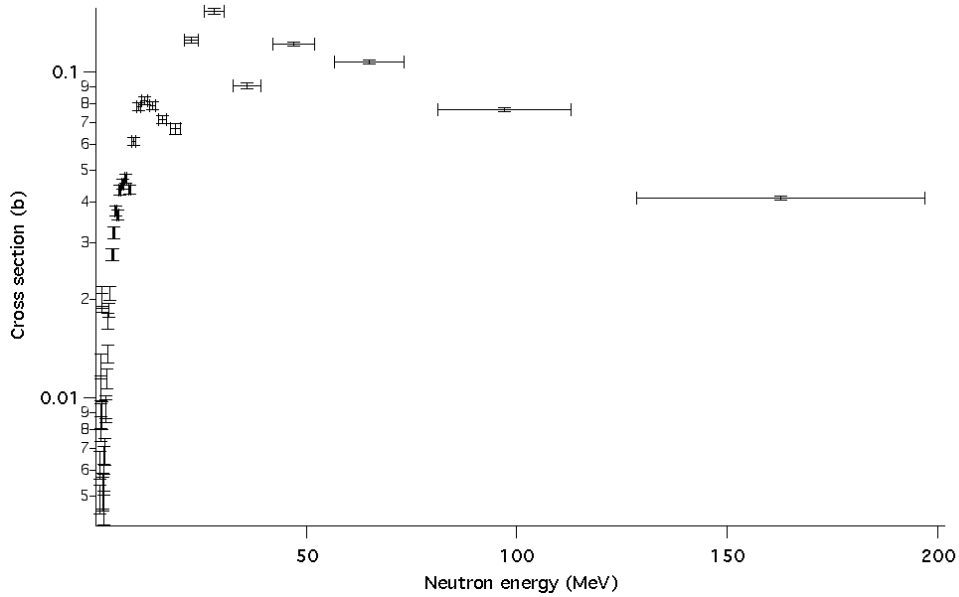


Figure 6.12. 646.1 keV $^{130}\text{Te}(n,\alpha)^{127}\text{Sn}$ γ -ray production cross section, from the ^{nat}Te experiment. At higher neutron energies above ~ 12 MeV, this γ -ray can also be produced by the $^{128}\text{Te}(n,2p)^{127}\text{Sn}$ reaction. The cross section has not been corrected for isotopic abundance.

Table 6.6. Total counts in the signal and background regions used to set the upper limit on the 2529 keV peak area.

	Signal region	Left background	Right background
Counts	6313	6260	6528
1σ	79	79	81

peak area was obtained by setting a 6 keV window centered at 2529 keV, and summing the counts in that window. In order to subtract the background, two equal 6 keV windows were set on the left and right sides of the signal window, and the average of the counts in these two windows was taken as the background. The procedure is summarized in table 6.6.

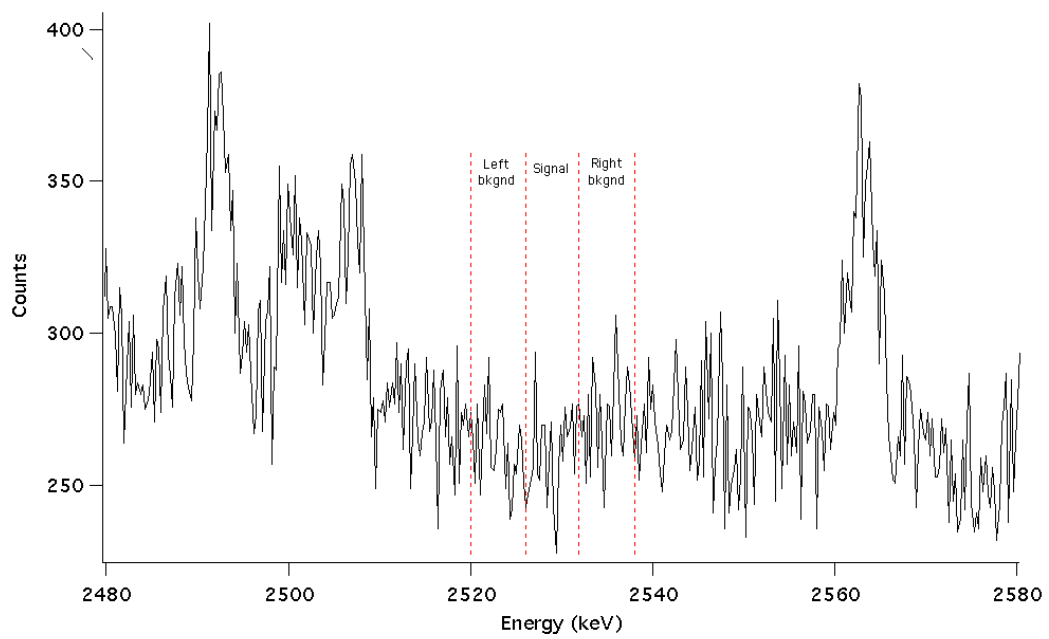


Figure 6.13. There is no evidence of the $^{126}\text{Te}(n,n'\gamma)$ line at 2529 keV, indicating that the cross section is small. The red dashed vertical lines indicate the three windows used to set the limit on the peak area.

Chapter 7

Conclusions

In this work, I have measured the partial γ -ray production cross sections for neutron reactions on Te isotopes. These reactions are potential sources of background for the CUORE experiment.

7.1 Cuoricino backgrounds

In order to test the compatibility of my cross section measurements with current Cuoricino data, I have searched for $(n,n'\gamma)$ transitions in the Cuoricino background spectrum. Most of this background would be rejected by the anti-coincidence veto, so the search was made in a spectrum without making the anti-coincidence cut. Looking at the Cuoricino spectrum, we can search for the largest expected neutron-induced peaks in the data with no anticoincidence cut (see figure 7.1). There is no evidence for the 666 keV transition in $^{126}\text{Te}(n,n'\gamma)$ or the 743 keV transition in $^{128}\text{Te}(n,n'\gamma)$. There is evidence of a feature at 839 keV, the first excited state transition excited by $^{130}\text{Te}(n,n'\gamma)$. However, this line can also be explained by ^{228}Ac decay, with a γ -ray at 840.2 keV (1% branching ratio).

In addition, I have looked for coincidences between the 666 keV transition in ^{126}Te and higher lying states. The spectrum of events coincident with the region [660,760] keV is shown in figure 7.2. In a search of Cuoricino data for the coincidence between the 666 keV

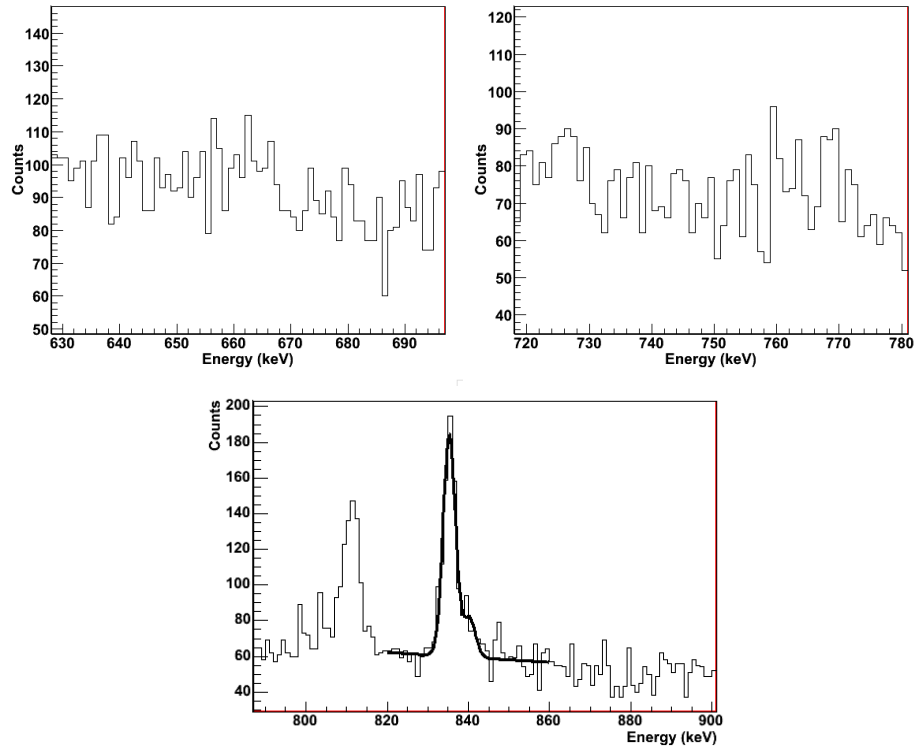


Figure 7.1. Cuoricino spectra for Run I, with no anticoincidence cut. The top two figures show the regions where the $^{126}\text{Te}(n,n'\gamma)$ and $^{128}\text{Te}(n,n'\gamma)$ first excited state transitions would be (666 keV and 743 keV, respectively). There is no evidence for these transitions. The bottom figure shows a similar search for $^{130}\text{Te}(n,n'\gamma)$ at 839.5 keV. While there is a feature near this location (on high energy side of large ^{54}Mn peak at 834.8 keV), this line can also be explained by ^{228}Ac decay, with a γ -ray at 840.2 keV (1% branching ratio).

transition (plus up to 100 keV of nuclear recoil energy) and the 2529 keV transition in ^{126}Te , no events were observed (see figure 7.2).

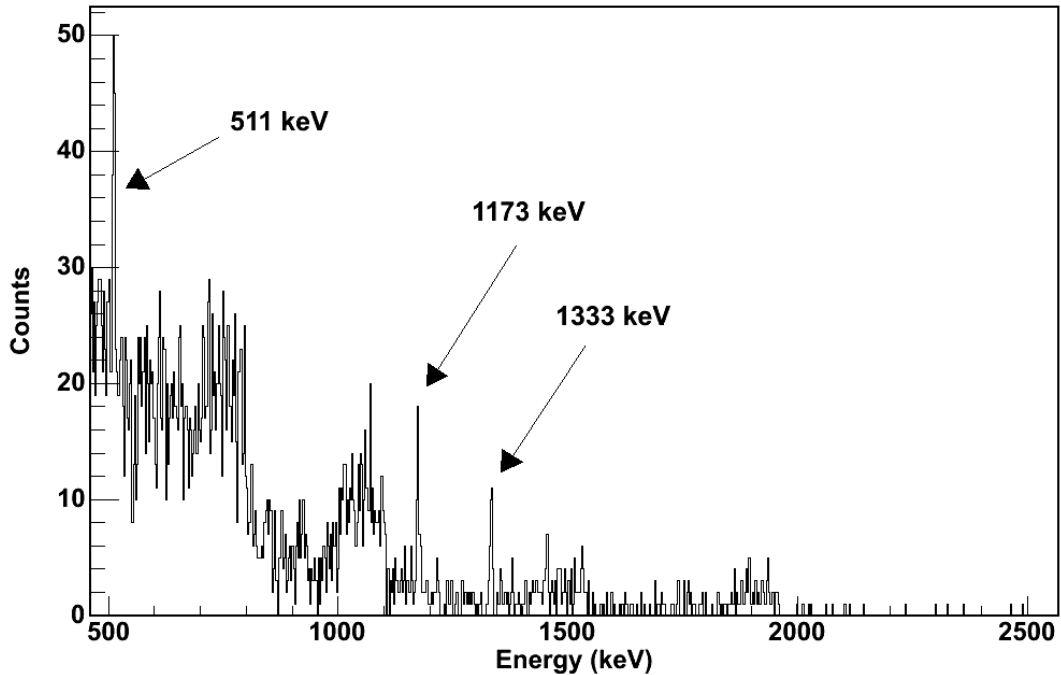


Figure 7.2. Cuoricino spectrum gated on [660,760] keV energy range. This represents a search for $^{126}\text{Te}(n,n'\gamma)$ 666 keV (+ recoil) events in coincidence with higher transitions, including the 2529 keV transition. The visible peaks in the spectrum are from the 511 keV annihilation peak and ^{60}Co decay. There is no indication of $^{126}\text{Te}(n,n'\gamma)$.

7.2 Implications for CUORE background

The results of this experiment will be combined with Monte Carlo simulations and Cuoricino data to place an experimental limit on the flux of muon-induced neutrons at LNGS. In addition, the cross-sections obtained from this measurement are necessary in order to study of the feasibility of the background requirements for CUORE in its planned location.

This technique is already being employed at GEANIE to measure the cross sections for possible neutron-induced backgrounds in the common shielding materials copper and lead. As $0\nu\text{DBD}$ experiments evolve toward larger masses and lower backgrounds, the neutron-

induced background will be an increasingly important concern for siting, shielding, and other experimental design considerations.

An initial estimate of the expected rate of neutron-induced events in the 2529 keV peak in CUORE can be made through a simple calculation. For this calculation, it is important to note that the neutron spectrum at GEANIE is similar to the underground neutron spectrum. The rate of 2529 keV events caused by the $^{126}\text{Te}(n,n'\gamma)$ reaction in the detector is given by equation 7.1:

$$R_{2529\text{keV}} = N_{126\text{Te}} \times \sigma_{2529\text{keV}} \times \phi_n / \delta / m_{\text{detector}}, \quad (7.1)$$

where $N_{126\text{Te}}$ is the number of ^{126}Te nuclei in the detector, $\sigma_{2529\text{keV}}$ is the upper limit on the $^{126}\text{Te}(n,n'\gamma)$ gamma production cross section for the 2529 keV line, ϕ_n is the total neutron flux expected inside the detector shielding, δ is the energy resolution at 2530 keV, and m_{detector} is the total detector mass of CUORE. The CUORE detector will contain approximately 112 kg of ^{126}Te , out of a total detector mass of approximately 750 kg, and will have an energy resolution of 5 keV FWHM in the $0\nu\text{DBD}$ region of interest. FLUKA simulations of the neutron flux reaching the CUORE detector give the neutron flux inside the cryostat as 3.4×10^{-11} neutrons/cm²/s for neutrons with energies of 3 MeV to 20 MeV [61]. I estimate a total rate of $< 10^{-6}$ counts/keV/kg/year in the 2529 keV peak from the $^{126}\text{Te}(n,n'\gamma)$ reaction. This is well below the goal background of 10^{-2} counts/keV/kg/year for CUORE, indicating that this particular source of background will be totally negligible in CUORE.

One concern is the full peak energy creating a false signal in the $0\nu\text{DBD}$ region of interest. For example, in order for the $^{126}\text{Te}(n,n'\gamma)$ reaction to deposit 2529 keV of energy in a crystal, the γ -ray will have to escape from the crystal in which it was produced (in coincidence with a 666 keV γ -ray and additional energy deposited by the nuclear recoil) and deposit its full energy in a neighboring crystal. Therefore, this rate will be further reduced by the low efficiency for this process and by the cut on coincident events in CUORE. However, lower energy neutron-induced γ -rays that occur in coincidence with a nuclear recoil are also potential contributors to the continuum background in the region of interest.

Using the calculated cross sections, detailed simulations will provide a full understanding of the neutron-induced backgrounds for CUORE.

7.3 CUORE outlook

The CUORE collaboration is scheduled to complete construction of the CUORE experiment at the end of 2012. This experiment will provide an independent check of the Heidelberg-Moscow KKCD result on its way to probing the inverse mass hierarchy. Achievement of the low background goal of 0.01 counts/keV/kg/year will represent a major technical accomplishment for the CUORE collaboration. As we enter a new regime of low background $0\nu\text{DBD}$ experiments, it is important to consider potential new sources of background. If CUORE has a positive result, it will be important to rule out sources other than $0\nu\text{DBD}$. In this work, I have ruled out one possible source of a false signal in the 2530 keV $0\nu\text{DBD}$ region of interest, the 2529 keV transition resulting from the $^{126}\text{Te}(n,n'\gamma)$ reaction. In addition, this work will help to improve our ability to accurately simulate and understand the background of the CUORE experiment.

Bibliography

- [1] C. L. Cowan, F. Reines, F. B. Harrison, H. W. Kruse, and A. D. McGuire. Detection of the free neutrino: A Confirmation. *Science*, 124:103–104, 1956.
- [2] C. Arnaboldi et al. Results from the CUORICINO neutrinoless double beta decay experiment. *Phys. Rev.*, C78:035502, 2008. Submitted to Phys.Rev.C.
- [3] Dongming Mei and A. Hime. Muon-induced background study for underground laboratories. *Phys. Rev.*, D73:053004, 2006.
- [4] W. Pauli. Dear radioactive ladies and gentlemen. *Phys. Today*, 31N9:27, 1978.
- [5] G. Danby et al. Observation of high-energy neutrino reactions and the existence of two kinds of neutrinos. *Phys. Rev. Lett.*, 9:36–44, 1962.
- [6] K. Kodama et al. Observation of tau-neutrino interactions. *Phys. Lett.*, B504:218–224, 2001.
- [7] Jr. Davis, Raymond, Don S. Harmer, and Kenneth C. Hoffman. Search for neutrinos from the sun. *Phys. Rev. Lett.*, 20:1205–1209, 1968.
- [8] W. Hampel et al. GALLEX solar neutrino observations: Results for GALLEX IV. *Phys. Lett.*, B447:127–133, 1999.
- [9] J. N. Abdurashitov et al. Measurement of the solar neutrino capture rate by the Russian-American gallium solar neutrino experiment during one half of the 22-year cycle of solar activity. *J. Exp. Theor. Phys.*, 95:181–193, 2002.

- [10] Q. R. Ahmad et al. Direct evidence for neutrino flavor transformation from neutral-current interactions in the Sudbury Neutrino Observatory. *Phys. Rev. Lett.*, 89:011301, 2002.
- [11] S. Fukuda et al. Tau neutrinos favored over sterile neutrinos in atmospheric muon neutrino oscillations. *Phys. Rev. Lett.*, 85:3999–4003, 2000.
- [12] K. Eguchi et al. First results from KamLAND: Evidence for reactor anti- neutrino disappearance. *Phys. Rev. Lett.*, 90:021802, 2003.
- [13] S. Abe et al. Precision Measurement of Neutrino Oscillation Parameters with KamLAND. *Phys. Rev. Lett.*, 100:221803, 2008.
- [14] S. Eidelman et al. Review of particle physics. *Phys. Lett.*, B592:1, 2004.
- [15] G. Drexlin. KATRIN: Direct measurement of a sub-eV neutrino mass. *Nucl. Phys. Proc. Suppl.*, 145:263–267, 2005.
- [16] E. Andreotti et al. MARE, Microcalorimeter Arrays for a Rhenium Experiment: A detector overview. *Nucl. Instrum. Meth.*, A572:208–210, 2007.
- [17] Rabindra N. Mohapatra and Goran Senjanovic. Neutrino mass and spontaneous parity nonconservation. *Phys. Rev. Lett.*, 44:912, 1980.
- [18] S. R. Elliott, A. A. Hahn, and M. K. Moe. Direct evidence for two-neutrino double-beta decay in Se- 82. *Phys. Rev. Lett.*, 59:2020–2023, 1987.
- [19] Frank T. Avignone, Steven R. Elliott, and Jonathan Engel. Double beta decay, majorana neutrinos, and neutrino mass. arXiv:0708.1033, 2007.
- [20] National Nuclear Data Center, BNL. Double beta ($\beta\beta$) decay data. <http://www.nndc.bnl.gov/bbdecay/>.
- [21] I. Ogawa et al. Search for neutrino-less double beta decay of Ca-48 by CaF-2 scintillator. *Nucl. Phys.*, A730:215–223, 2004.

- [22] H. V. Klapdor-Kleingrothaus, I. V. Krivosheina, A. Dietz, and O. Chkvorets. Search for neutrinoless double beta decay with enriched Ge-76 in Gran Sasso 1990-2003. *Phys. Lett.*, B586:198–212, 2004.
- [23] R. Arnold et al. First results of the search of neutrinoless double beta decay with the NEMO 3 detector. *Phys. Rev. Lett.*, 95:182302, 2005.
- [24] R. Arnold et al. Double beta decay of Zr96. *Nucl. Phys.*, A658:299, 1999.
- [25] Fedor A. Danevich et al. Search for 2 beta decay of cadmium and tungsten isotopes: Final results of the Solotvina experiment. *Phys. Rev.*, C68:035501, 2003.
- [26] R.B. Firestone and L.P. Ekström. WWW Table of radioactive isotopes. <http://ie.lbl.gov/toi/>, January 2004.
- [27] R. Bernabei et al. Investigation of beta beta decay modes in Xe-134 and Xe- 136. *Phys. Lett.*, B546:23–28, 2002.
- [28] A. A. Klimenko, A. A. Pomansky, and A. A. Smolnikov. Low background scintillation installation for double beta decay experiments. *Nucl. Instrum. Meth.*, B17:445–449, 1986.
- [29] J. Schechter and J. W. F. Valle. Neutrinoless double-beta decay in $SU(2) \times U(1)$ theories. *Phys. Rev.*, D25:2951, 1982.
- [30] Craig Aalseth et al. Neutrinoless double beta decay and direct searches for neutrino mass. *APS Neutrino Study*, 2004.
- [31] Steven R. Elliott and Petr Vogel. Double beta decay. *Annu. Rev. Nucl. Part. Sci.*, 52:115–151, 2002.
- [32] V. A. Rodin, A. Faessler, F. Simkovic, and P. Vogel. Assessment of uncertainties in QRPA 0nu beta beta-decay nuclear matrix elements. *Nucl. Phys.*, A766:107–131, 2006.
- [33] R. Ardito et al. CUORE: A cryogenic underground observatory for rare events. arXiv:hep-ex/0501010, 2005.

- [34] C. E. Aalseth et al. The IGEX Ge-76 neutrinoless double-beta decay experiment: Prospects for next generation experiments. *Phys. Rev.*, D65:092007, 2002.
- [35] M. Gunther et al. Heidelberg - Moscow beta beta experiment with Ge-76: Full setup with five detectors. *Phys. Rev.*, D55:54–67, 1997.
- [36] H. V. Klapdor-Kleingrothaus, A. Dietz, H. L. Harney, and I. V. Krivosheina. Evidence for neutrinoless double beta decay. *Mod. Phys. Lett.*, A16:2409–2420, 2001.
- [37] Alexander S. Barabash. NEMO 3 double beta decay experiment: latest results. arXiv:nucl-ex/0807.2336, 2008.
- [38] M. Danilov et al. Detection of very small neutrino masses in double-beta decay using laser tagging. *Phys. Lett.*, B480:12–18, 2000.
- [39] Stefan. Schonert. Status of the GERmanium Detector Array (GERDA) for the search of neutrinoless beta beta decays of Ge-76 at LNGS. *Prog. Part. Nucl. Phys.*, 57:241–250, 2006.
- [40] Richard Gaitskell et al. White paper on the Majorana zero-neutrino double-beta decay experiment. arXiv:nucl-ex/0311013, 2003.
- [41] P. Moon and L. R. Steinhardt. Dielectric bolometer. *Journal of the Optical Society of America*, 28(5):148–162, May 1938.
- [42] M. Pedretti. *The single module for Cuoricino and CUORE detectors: Tests, construction and modelling*. PhD thesis, Università degli Studi dell’Insubria, 2004.
- [43] E. Fiorini and T. O. Niinikoski. Low temperature calorimetry for rare decays. *Nucl. Instr. Meth.*, A224:83, 1984.
- [44] G. Audi, A. H. Wapstra, and C. Thibault. The Ame2003 atomic mass evaluation (II). Tables, graphs and references. *Nucl. Phys.*, A729:337–676, 2002.
- [45] A. Staudt, T. T. S. Kuo, and H. V. Klapdor-Kleingrothaus. Beta beta decay of Te-128, Te-130, and Ge-76 with renormalized effective interactions derived from Paris and Bonn potentials. *Phys. Rev.*, C46:871–883, 1992.

- [46] G. Pantis, F. Simkovic, J. D. Vergados, and Amand Faessler. Neutrinoless double beta decay within QRPA with proton- neutron pairing. *Phys. Rev.*, C53:695–707, 1996.
- [47] P. Vogel and M. R. Zirnbauer. Suppression of the two-neutrino double-beta decay by nuclear-structure effects. *Phys. Rev. Lett.*, 57:3148–3151, 1986.
- [48] O. Civitarese and J. Suhonen. Extracting information on the 0ν beta beta decays from the 2ν beta beta decays. *Nucl. Phys.*, A761:313–332, 2005.
- [49] T. Tomoda. Double beta decay. *Rept. Prog. Phys.*, 54:53–126, 1991.
- [50] C. Barbero, F. Krmpotic, A. Mariano, and D. Tadic. Nuclear moments for the neutrinoless double beta decay. II. *Nucl. Phys.*, A650:485–497, 1999.
- [51] F. Simkovic, G. Pantis, J. D. Vergados, and Amand Faessler. Additional nucleon current contributions to neutrinoless double beta decay. *Phys. Rev.*, C60:055502, 1999.
- [52] J. Suhonen, O. Civitarese, and Amand Faessler. Description of the $0^+ \rightarrow 0^+$ neutrinoless double beta decay transition in Ge-76: Particle number projected quasiparticle random phase approximation. *Nucl. Phys.*, A543:645–660, 1992.
- [53] K. Muto, E. Bender, and H. V. Klapdor. Nuclear structure effects on the neutrinoless double beta decay. *Z. Phys.*, A334:187–194, 1989.
- [54] S. Stoica and H. V. Klapdor-Kleingrothaus. Neutrinoless double- beta -decay matrix elements within the second quasirandom phase approximation method. *Phys. Rev.*, C63:064304, 2001.
- [55] Amand Faessler and Fedor Simkovic. Double beta decay. *J. Phys.*, G24:2139–2178, 1998.
- [56] J. Engel, P. Vogel, Xiang-Dong Ji, and S. Pittel. Double beta decay in the generalized seniority scheme. *Phys. Lett.*, B225:5–9, 1989.
- [57] M. Aunola and J. Suhonen. Mean-field effects on neutrinoless double beta decay. *Nucl. Phys.*, A643:207–221, 1998.

- [58] E. Caurier, F. Nowacki, and A. Poves. Nuclear structure aspects of the neutrinoless double beta decay. *Eur. Phys. J.*, A36:195–200, 2008.
- [59] C. Arnaboldi et al. A calorimetric search on double beta decay of Te-130. *Phys. Lett.*, B557:167–175, 2003.
- [60] I. Perlman and Frank Asaro. Pottery analysis by neutron activation. In Robert H. Brill, editor, *Science and Archaeology*, pages 182–195. MIT Press, 1971.
- [61] F. Bellini et al. MonteCarlo evaluation of external neutron and muon induced background in the CUORE experiment. Internal note CUORE/07-04/01, CUORE Collaboration, 2007.
- [62] F. Arneodo et al. Neutron background measurements in the Hall C of the Gran Sasso Laboratory. *Nuovo Cim.*, A112:819–831, 1999.
- [63] P. Belli et al. Deep underground neutron flux measurement with large BF-3 counters. *Nuovo Cim.*, A101:959–966, 1989.
- [64] H. Wulandari, J. Jochum, W. Rau, and F. von Feilitzsch. Neutron flux underground revisited. *Astropart. Phys.*, 22:313–322, 2004.
- [65] S. F. Hicks et al. Intruder structures observed in Te-122 through inelastic neutron scattering. *Phys. Rev.*, C71:034307, 2005.
- [66] J. R. Vanhoy et al. Lifetimes in Te-126 from in-beam (n, n-prime**gamma) measurements. *Phys. Rev.*, C69:064323, 2004.
- [67] R. Reifarth et al. (n, γ) measurements on radioactive isotopes with DANCE. *Nucl. Instr. Meth.*, B241:176, 2005.
- [68] D. Rochman et al. Neutron-induced reaction studies at FIGARO using a spallation source. *Nucl. Instr. Meth.*, A523:102, 2004.
- [69] B.W. Riemer et al. SNS target tests at the LANSCE-WNR in 2001 - Part I. *J. Nucl. Mater.*, 318:92, 2003.

- [70] B.E. Takala. The Ice House: Neutron testing leads to more-reliable electronics. *Los Alamos Science*, 30:96, 2006.
- [71] J.A. Becker and R.O. Nelson. . *Nucl. Phys. News Int.*, 7:11, 1997.
- [72] R.M. Diamond. The Berkeley HighResolution Ball. In D. Shapira, editor, *Instrumentation for heavyion research*, page 259. Harwood Academic, New York, 1985.
- [73] Walid Younes. The XGAM peak-fitting program. Manuscript in preparation.
- [74] W. Younes et al. The $^{235}\text{U}(n,2n\gamma)$ yrast partial gamma-ray cross sections: A report on the 1998 – 1999 GEANIE data and analysis techniques. Technical report UCRL-ID-140313, Lawrence Livermore National Laboratory, 2000.
- [75] W. Younes. GEANIE data usersub version 99-1.1. Software documentation, December 1999.
- [76] D.P. McNabb et al. Uncertainty budget and efficiency analysis for the $^{239}\text{Pu}(n,2n\gamma)$ partial reaction cross-section measurements. Technical report UCRL-ID-139906, Lawrence Livermore National Laboratory, 2000.
- [77] R.O. Nelson. Neutron-induced reactions and spectroscopy with GEANIE. In *Proceedings of the International Conference on Nuclear Data for Science and Technology*. American Institute of Physics, 2004.
- [78] M.J. Berger et al. XCOM: Photon cross sections database. <http://physics.nist.gov/PhysRefData/Xcom/Text/XCOM.html>, August 2005.
- [79] T-2 Nuclear Information Service, LANL. QTOOL: Calculation of reaction Q-values and thresholds. <http://t2.lanl.gov/data/qtool.html>, March 1997.

Appendix A

The XGAM software package

The XGAM package was developed by Walid Younes at LLNL specifically for processing GEANIE data [73]. The philosophy of the XGAM program is to define a continuous fit over the entire γ -ray spectrum, leading to a consistent background model. There are also additional programs to extract the cross sections as a function of neutron energy from the overall fit.

A.1 Fitting functions

The fit includes a polynomial background and a user-defined set of peaks. γ -rays are fit with global peak shape parameters. The peak shape is a combination of a Gaussian, with Gaussian asymmetry, a step function, and high energy tails. The width of the peaks (full-width half-maximum) is parameterized by $w(x)$, given in equation A.1.

$$w(x) \equiv \sqrt{w_0^2 + w_1^2 \left(\frac{x}{1000}\right) + w_2^2 \left(\frac{x}{1000}\right)^2}. \quad (\text{A.1})$$

The background and peak shape functions are detailed below.

A.1.1 Continuum background

$$f_{bkg}(x; x_c) \equiv \sum_{i=0}^r b_i (x - x_c)^i \quad (\text{A.2})$$

A.1.2 Intrinsic peakshape

$$f_{gauss}(x; x_0, \sigma) \equiv \frac{1}{\sqrt{2\pi}\sigma} e^{-\frac{(x-x_0)^2}{2\sigma^2}} \quad (\text{A.3})$$

A.1.3 Compton background

$$f_{step}(x; x_0, \sigma) \equiv \frac{1}{2} \text{erfc} \left(\frac{x - x_0}{\sqrt{2}\sigma} \right) \quad (\text{A.4})$$

A.1.4 High energy tails

$$f_{tail}^h(x; x_0, \sigma, \beta_h) \equiv \frac{e^{\frac{\sigma^2}{2\beta_h^2}}}{2\beta_h} e^{-\left(\frac{x-x_0}{\beta_h}\right)} \text{erfc} \left(-\frac{x - x_0}{\sqrt{2}\sigma} + \frac{\sigma}{\sqrt{2}\beta_h} \right) \quad (\text{A.5})$$

A.1.5 Gaussian asymmetry

$$f_{asym}(x; x_0, \sigma) \equiv f_{gauss}(x; x_0, \sigma) \left[p_3 \left(\frac{x - x_0}{\sigma} \right)^4 + p_4 \left(\frac{x - x_0}{\sigma} \right)^{12} \right], x < x_0 \quad (\text{A.6})$$

$$f_{asym}(x; x_0, \sigma) \equiv 0, x > x_0 \quad (\text{A.7})$$

A.1.6 Total peakshape

$$f_{peak}(x) \equiv H \left(1 - \frac{R_h}{100} - \frac{3}{2} p_3 - \frac{10395}{2} p_4 \right) f_{gauss} + H f_{asym} + \frac{H R_h}{100} f_{tail} + \frac{H S}{100} f_{step} \quad (\text{A.8})$$

Table A.1. Peakshape parameters for ^{130}Te fit.

Detector type	Parameter	Value
coax	w0	6.2154786376e+00
coax	w1	2.4752467438e+00
coax	w2	9.7378557190e-01
coax	R_h	2.1936156031e+01
coax	β_h	9.1898745260e+00
coax	Step	1.3488574472e-04
coax	p3	1.7293312016e-02
coax	p4	9.0934575372e-07
planar	w0	6.2950680336e+00
planar	w1	7.5019597226e+00
planar	w2	4.7597232489e-01
planar	R_h	2.0637649486e+01
planar	β_h	7.6616763539e+00
planar	Step	1.1158085386e-03
planar	p30	6.2386593132e-03
planar	p31	7.0857869645e-07
planar	p40	2.2487746801e-06
planar	p41	-7.7155681135e-13

A.1.7 Fits to ^{130}Te and ^{nat}Te data

Final fit parameters for the ^{130}Te and ^{nat}Te runs are listed in table A.1 and table A.2.

The coaxial spectra summed over all detectors for neutron energies in the range of 1 to 250 MeV are shown in figures A.1 to A.12.

A.2 Extracting cross sections

Once the fitting function is defined for the spectrum summed over all neutron energies, XGAMEX is used to slice the matrix into constant time of flight neutron energy bins. The program then automatically reruns the fit for each neutron energy slice, allowing for changes in background and peak height while keeping peak centroids and global peak shape parameters constant.

The XGAMYIELD program is used to generate cross sections as a function of neutron energy. It takes as inputs the individual neutron energy bin fits, the fission chamber time of flight spectrum, deadtime, and efficiency, the Ge detector dead times and efficiencies, and

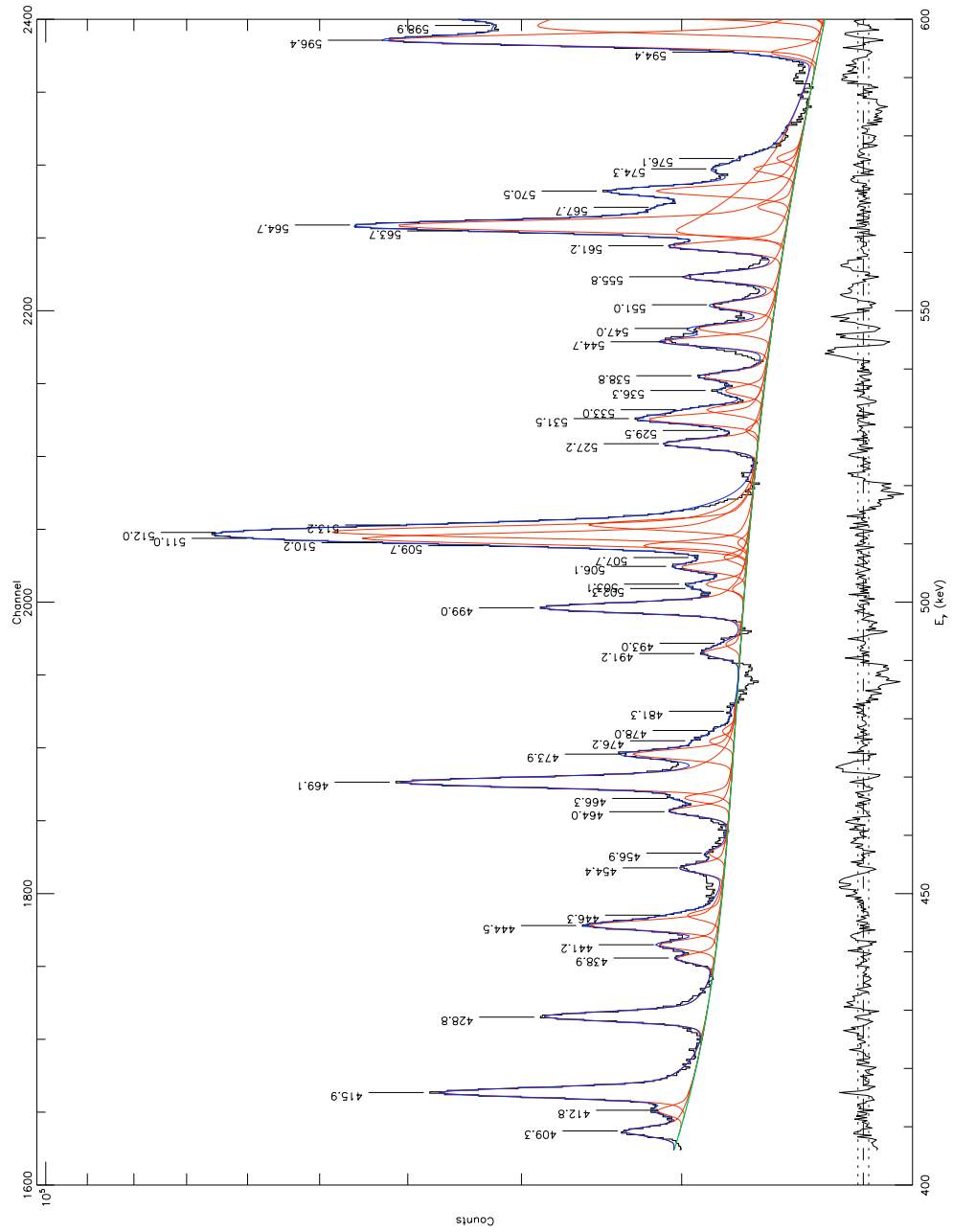


Figure A.1. ^{nat}Te coaxial sum spectrum with fit and residuals.

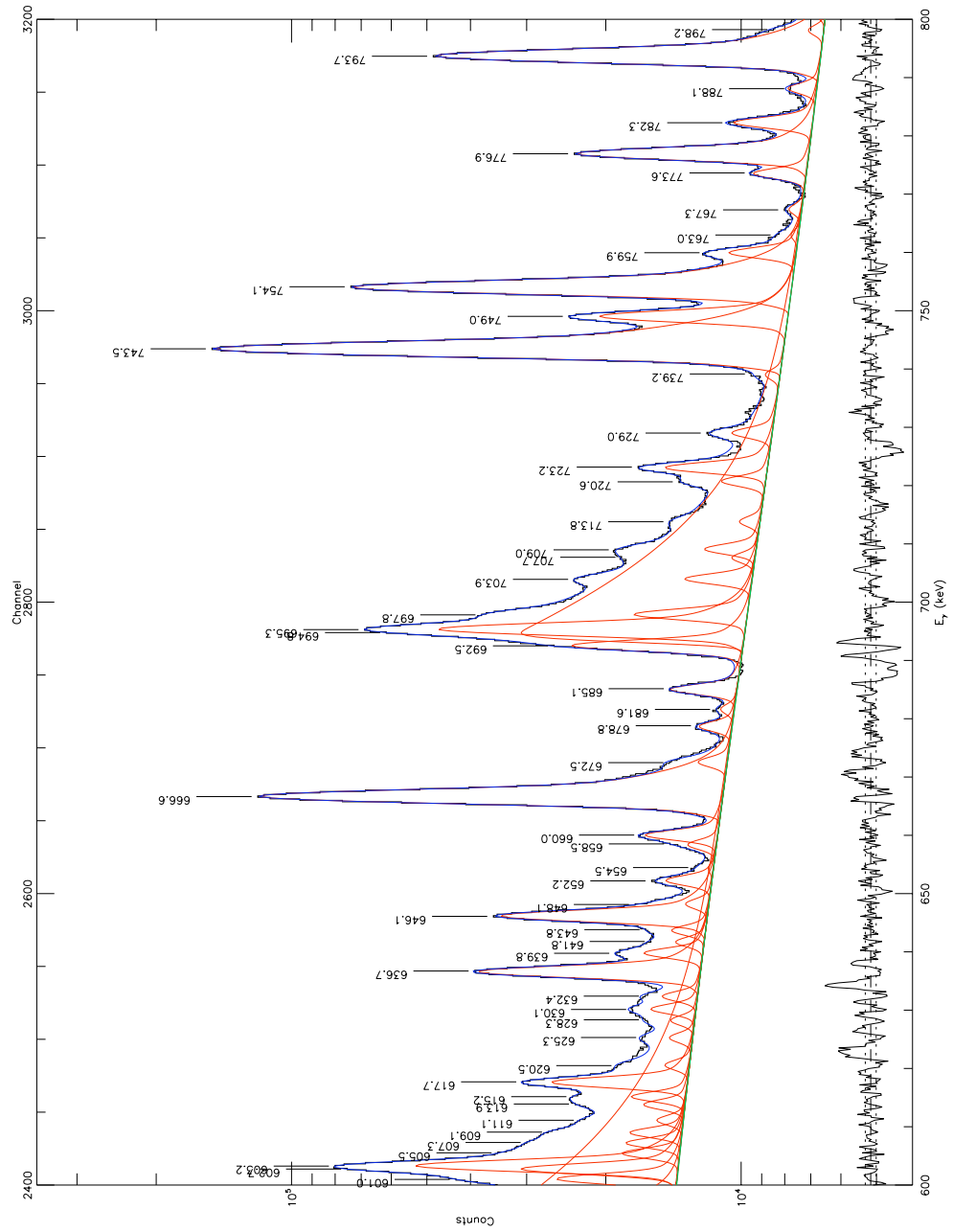


Figure A.2. ^{nat}Te coaxial sum spectrum with fit and residuals.

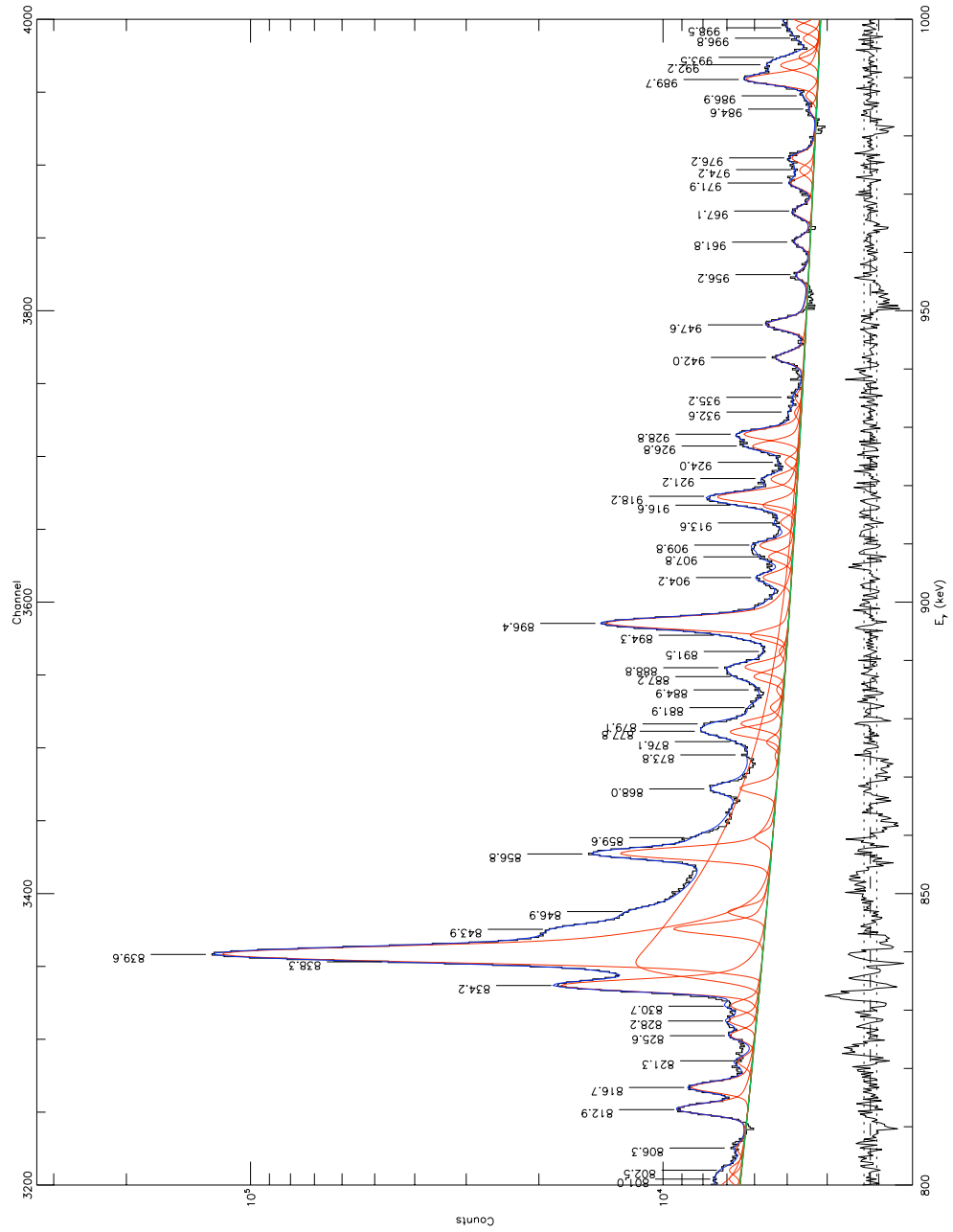


Figure A.3. ^{nat}Te coaxial sum spectrum with fit and residuals.

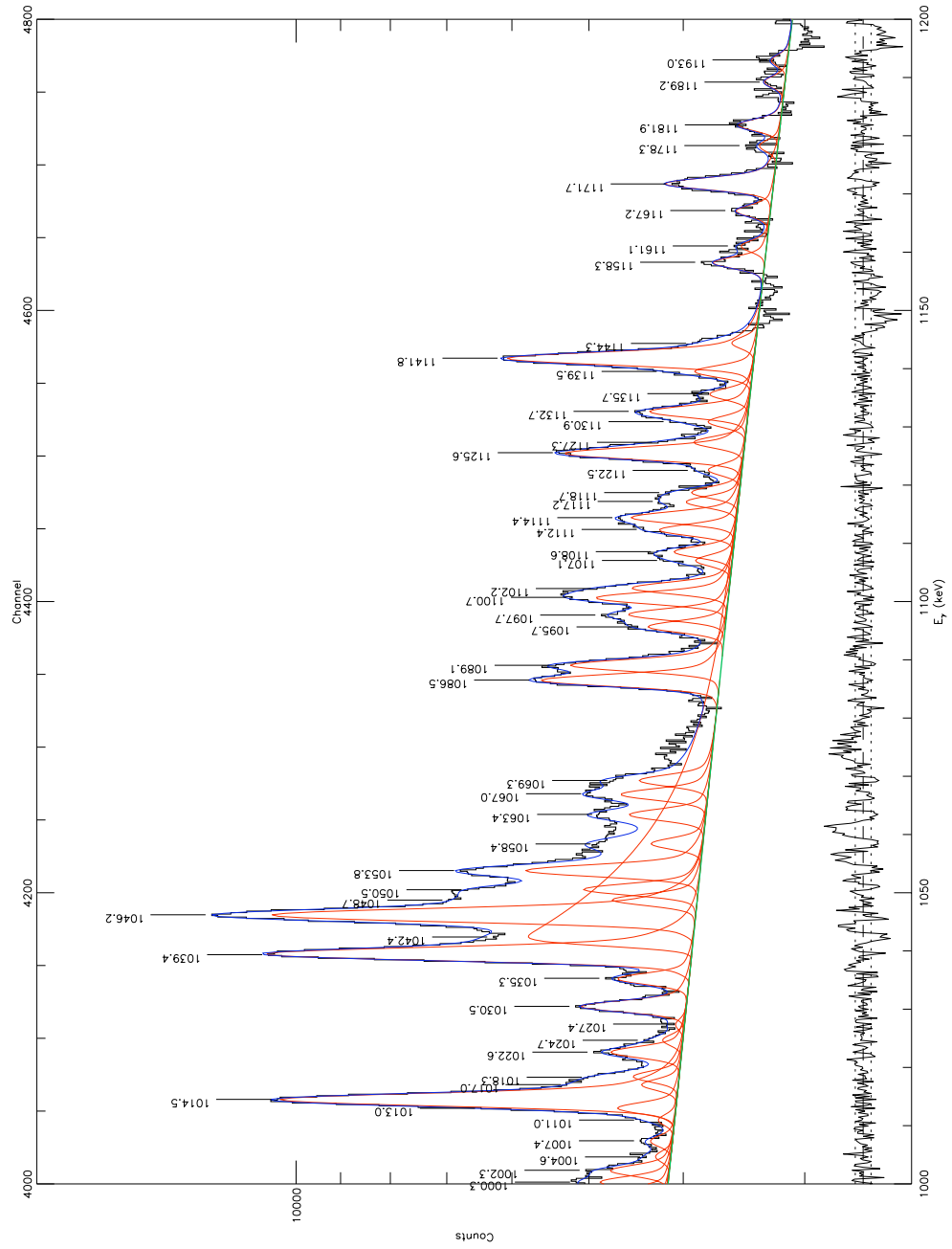


Figure A.4. ^{nat}Te coaxial sum spectrum with fit and residuals.

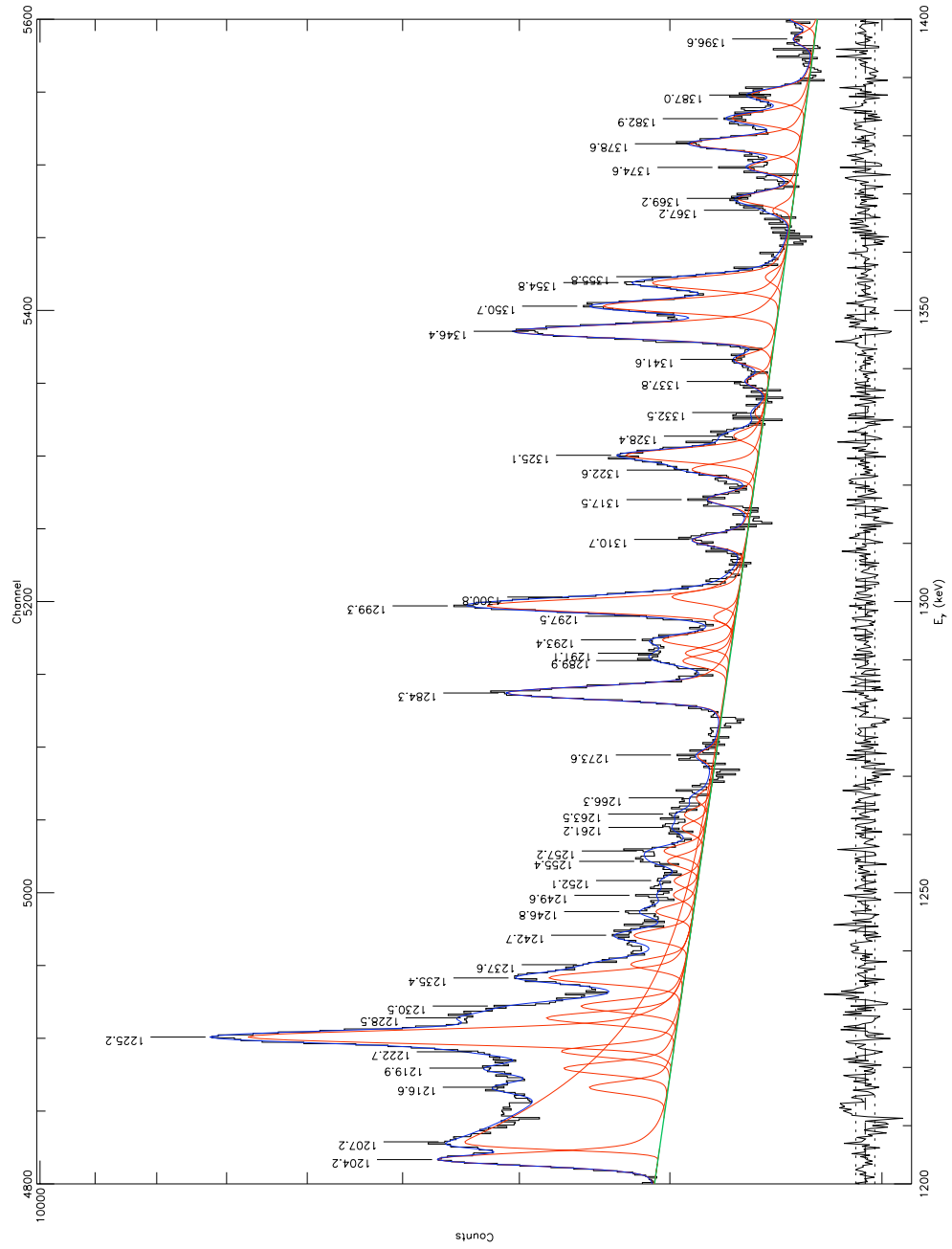


Figure A.5. ^{nat}Te coaxial sum spectrum with fit and residuals.

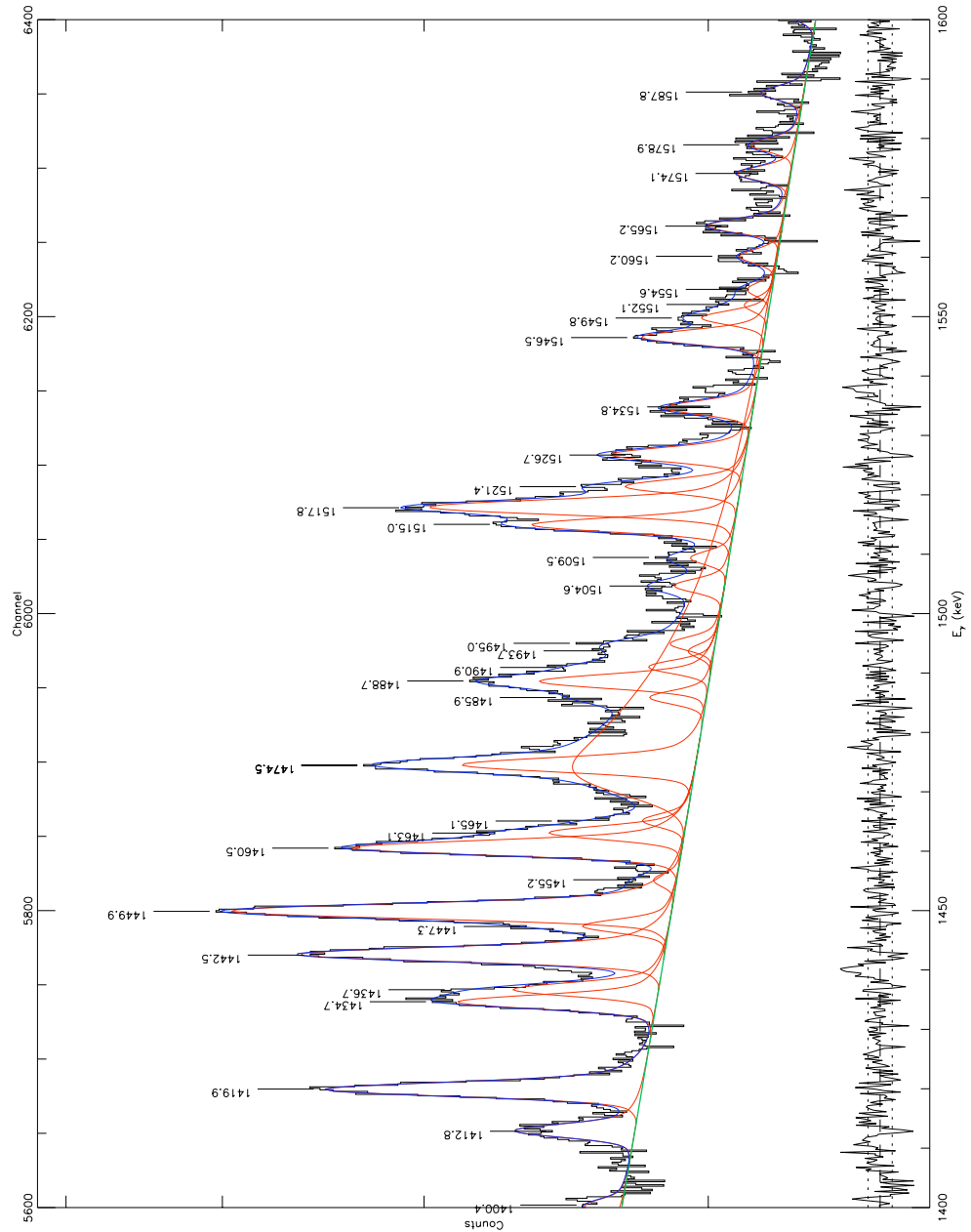


Figure A.6. ^{nat}Te coaxial sum spectrum with fit and residuals.

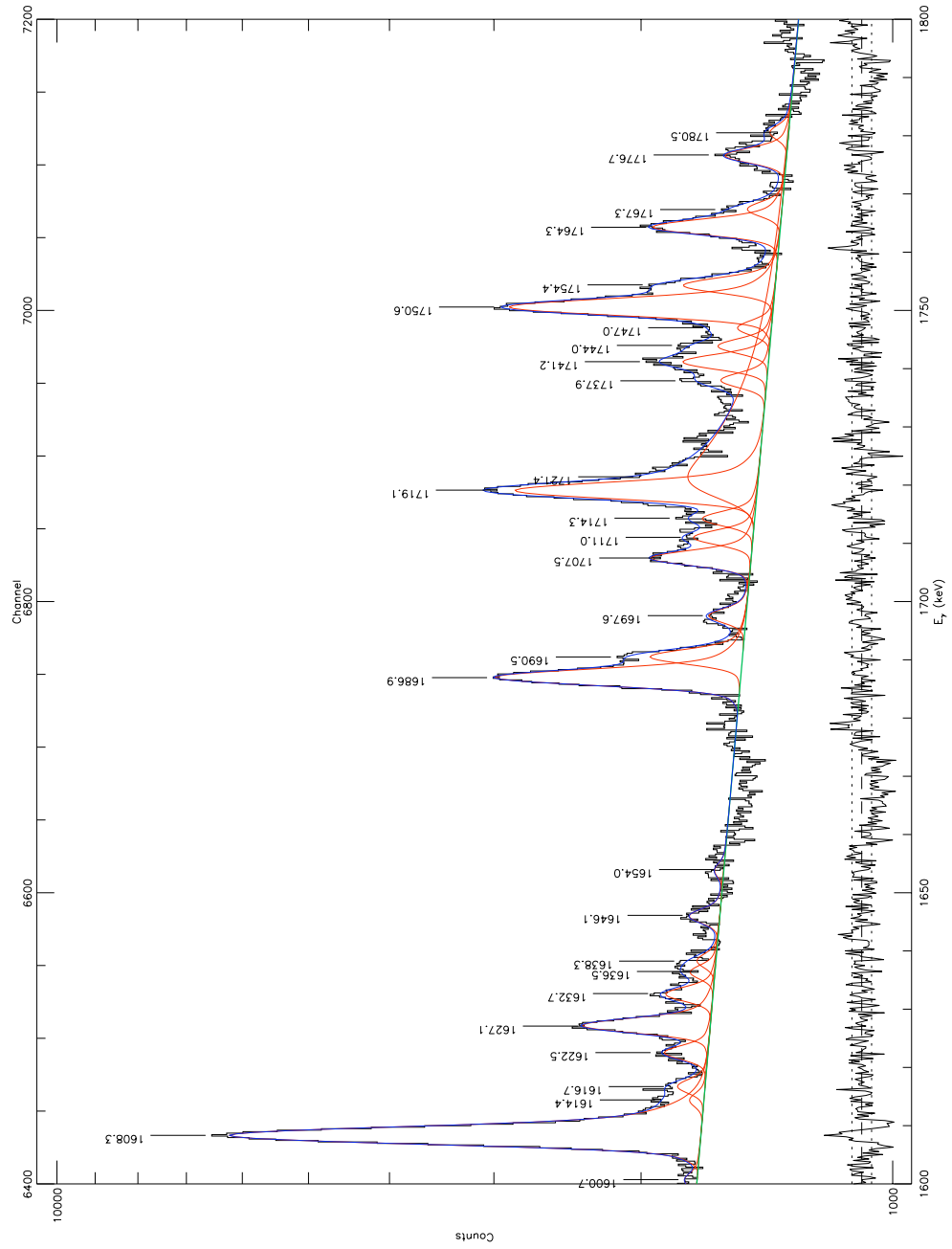


Figure A.7. ^{nat}Te coaxial sum spectrum with fit and residuals.

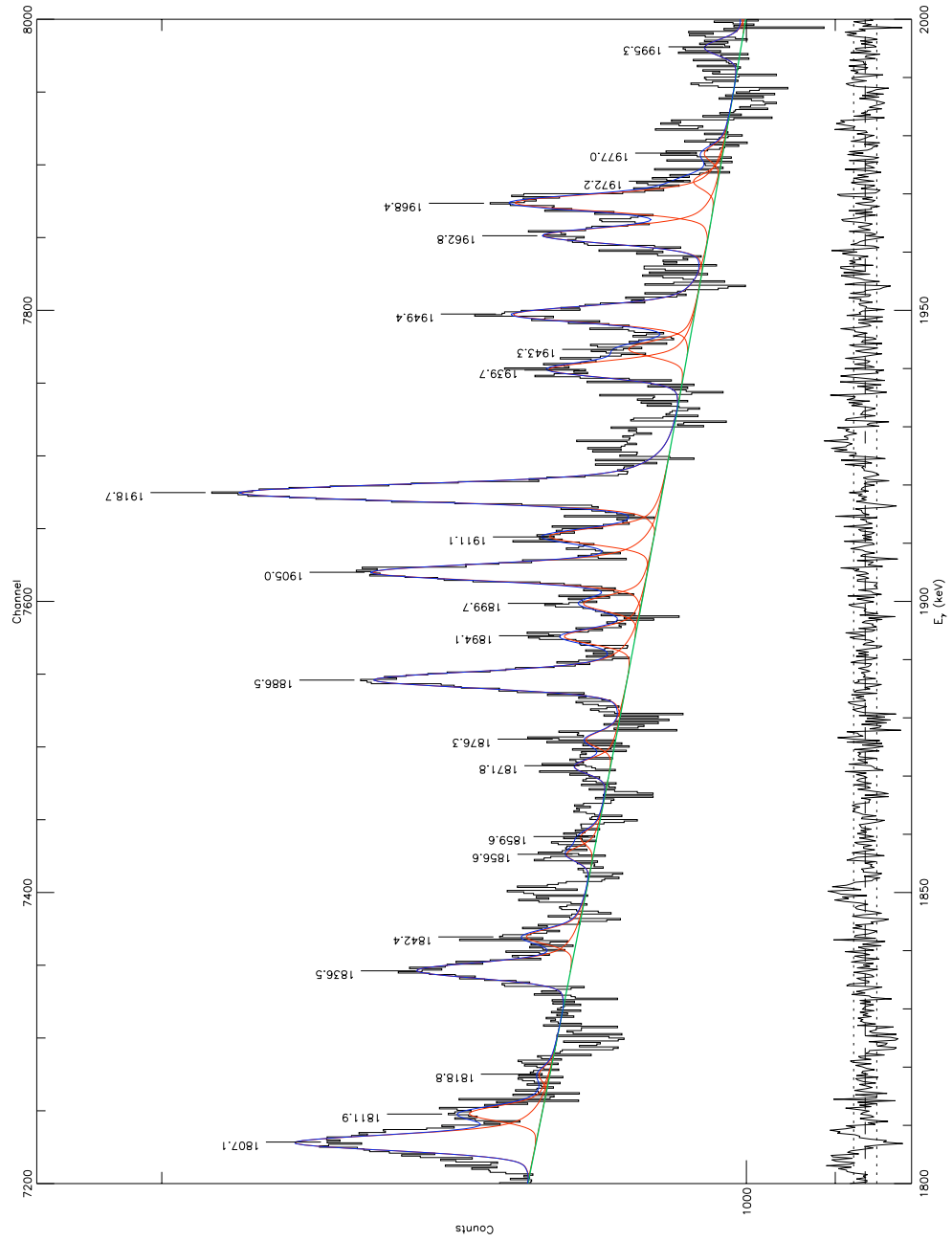


Figure A.8. ^{nat}Te coaxial sum spectrum with fit and residuals.

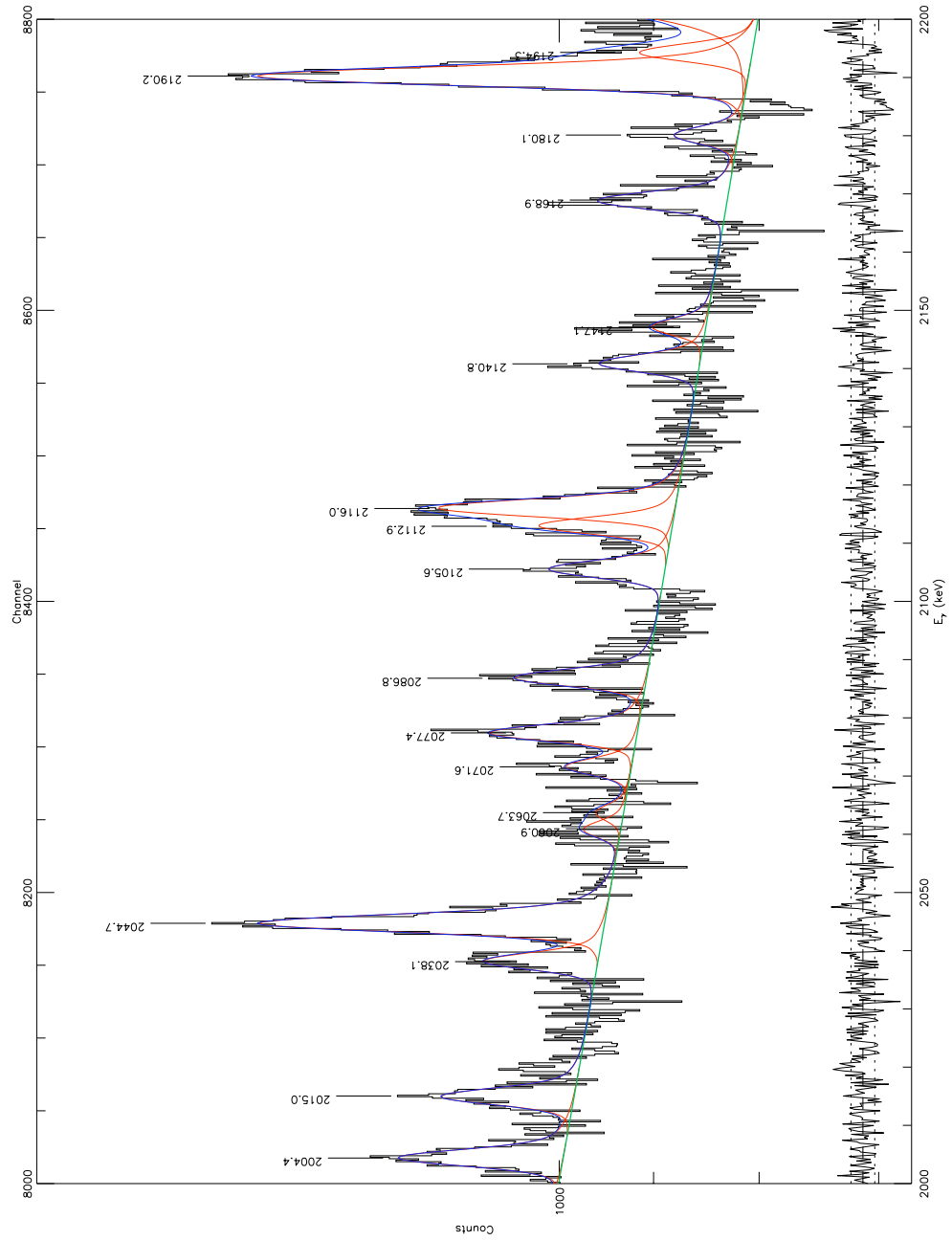


Figure A.9. ^{nat}Te coaxial sum spectrum with fit and residuals.

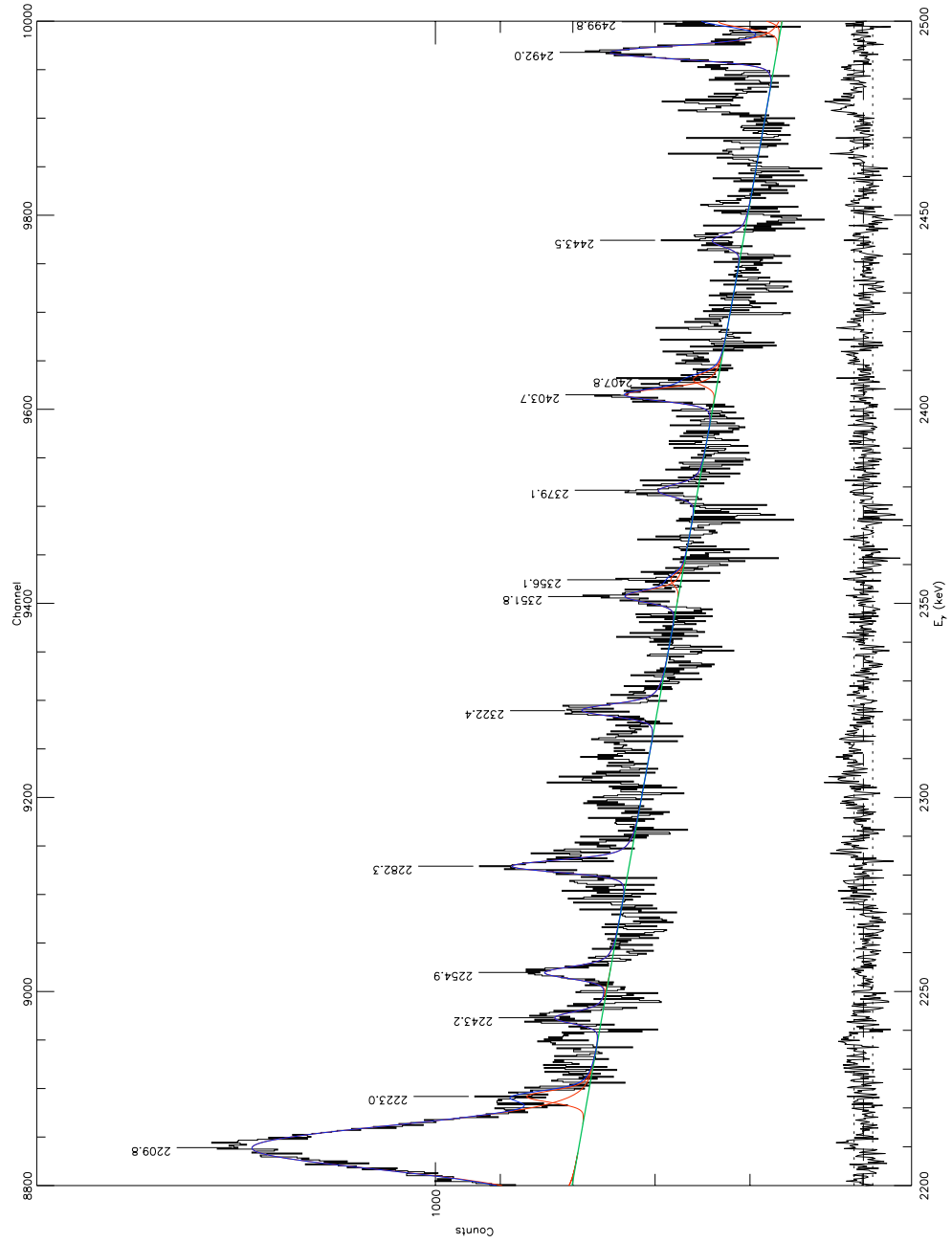


Figure A.10. ^{nat}Te coaxial sum spectrum with fit and residuals.

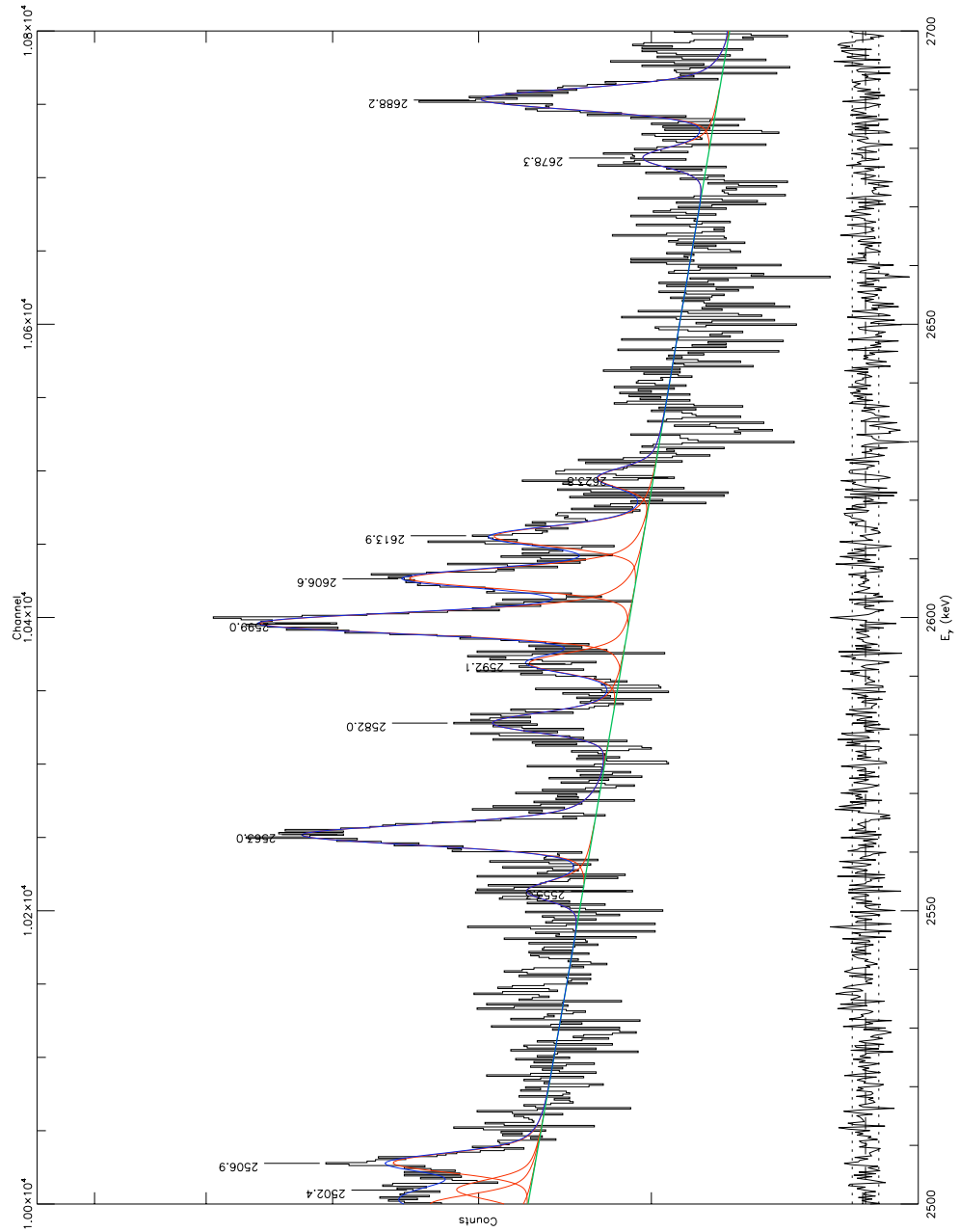


Figure A.11. ^{nat}Te coaxial sum spectrum with fit and residuals.

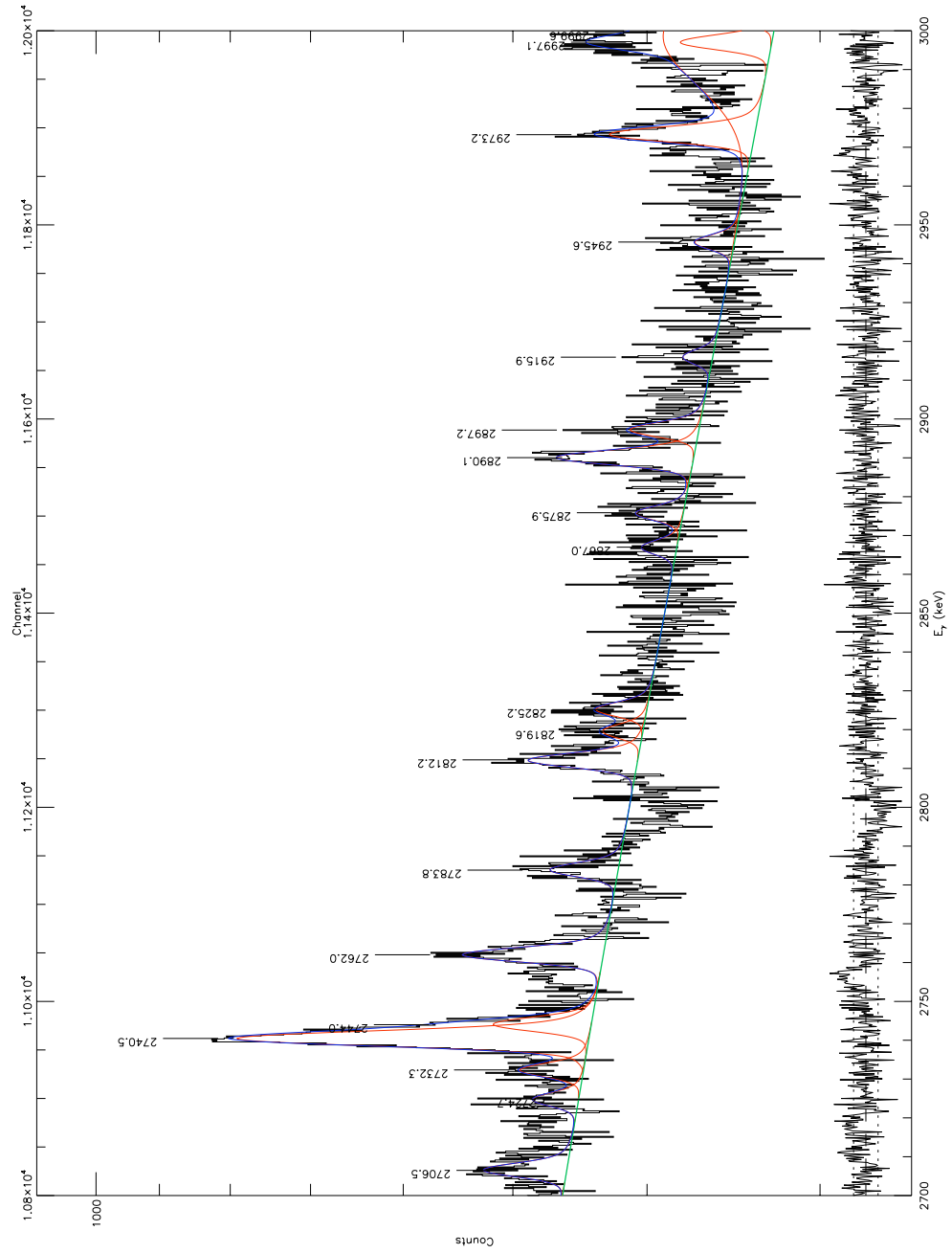


Figure A.12. ^{nat}Te coaxial sum spectrum with fit and residuals.

Table A.2. Peakshape parameters for ^{nat}Te fit.

Detector type	Parameter	Value
coax	w0	6.4904696929e+00
coax	w1	-1.3134333471e-04
coax	w2	1.2835388310e+00
coax	R_h	2.3924491004e+01
coax	β_h	8.9594067190e+00
coax	Step	2.1081392463e-06
coax	p ₃	1.3127730503e-02
coax	p ₄	1.3333749955e-06
planar	w0	1.0351133454e+01
planar	w1	6.4238199440e+00
planar	w2	-1.7101341729e-10
planar	R_h	1.5404307343e+01
planar	β_h	1.7378201415e+01
planar	Step	6.5284813921e-03
planar	p ₃	2.7310194161e-02
planar	p ₄	2.8247835321e-06

the areal number density of the target. Using this information, the program generates the cross section as a function of neutron energy for each γ -ray in the spectrum.

Appendix B

Additional γ -ray production cross sections

In this appendix are additional γ -ray production cross sections from the ^{nat}Te run. All cross sections in this appendix come from the coaxial detectors only and represent known neutron-induced transitions in the stable Te isotopes. These cross sections have not been corrected for isotopic abundances. In addition, the error bars do not include the normalization error or angular distribution errors discussed in section 6.5.

B.1 ^{130}Te excitations

The excitations in figures B.1 to B.9 are produced by the $^{130}\text{Te}(n,n'\gamma)^{130}\text{Te}$ reaction.

B.2 ^{128}Te excitations

The excitations in figures B.10 to B.12 are produced by the $^{128}\text{Te}(n,n'\gamma)^{128}\text{Te}$ and $^{130}\text{Te}(n,3n)^{128}\text{Te}$ reactions.

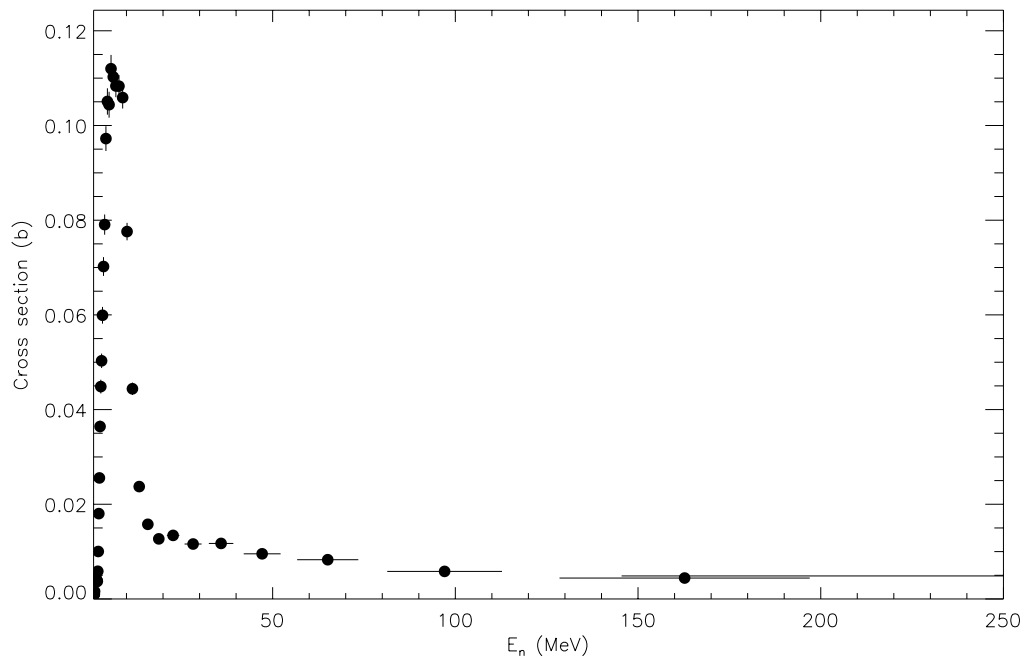


Figure B.1. Cross section for the 468 keV transition in ^{130}Te .

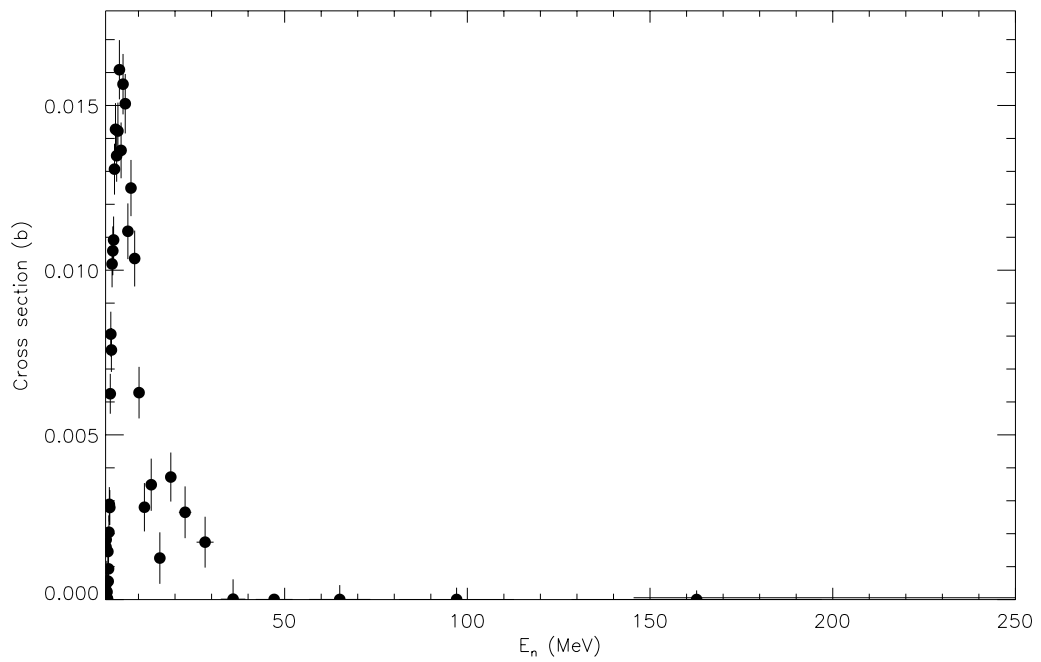


Figure B.2. Cross section for the 550 keV transition in ^{130}Te .

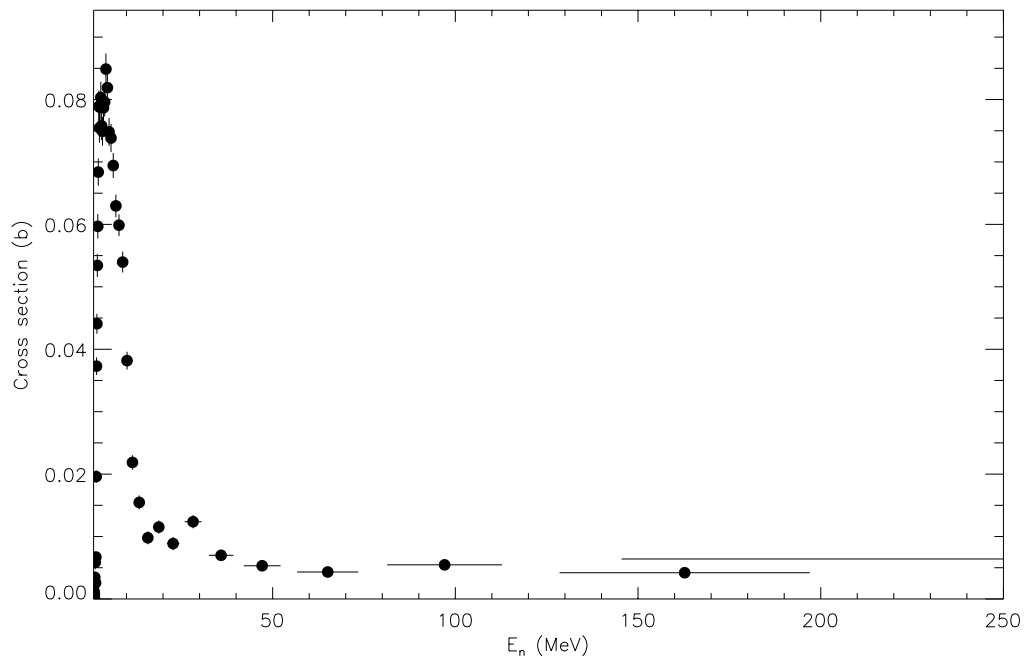


Figure B.3. Cross section for the 748 keV transition in ^{130}Te .

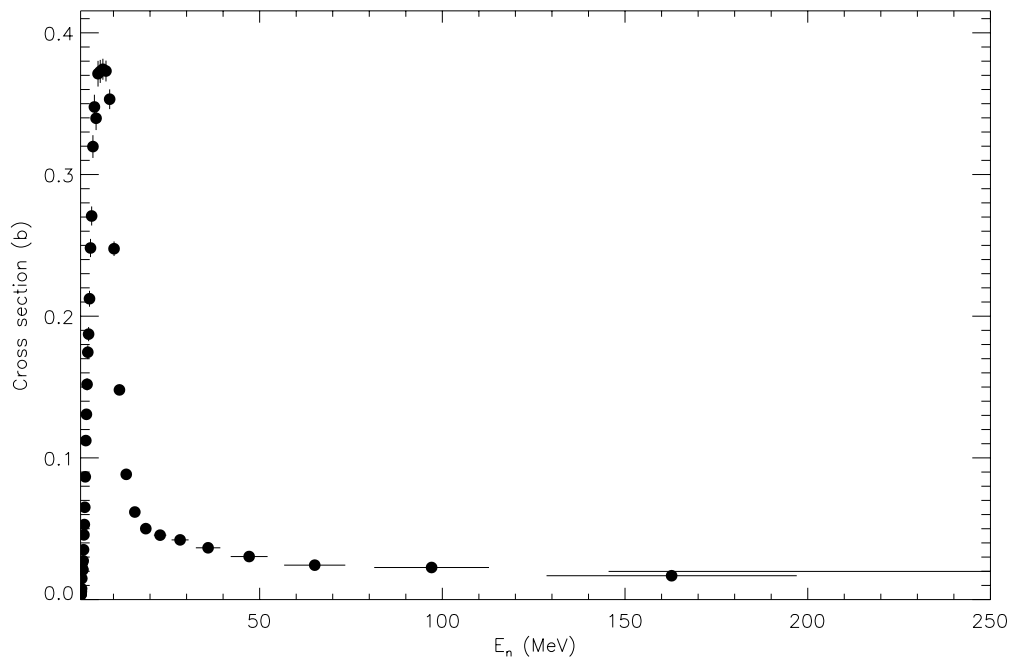


Figure B.4. Cross section for the 793 keV transition in ^{130}Te .

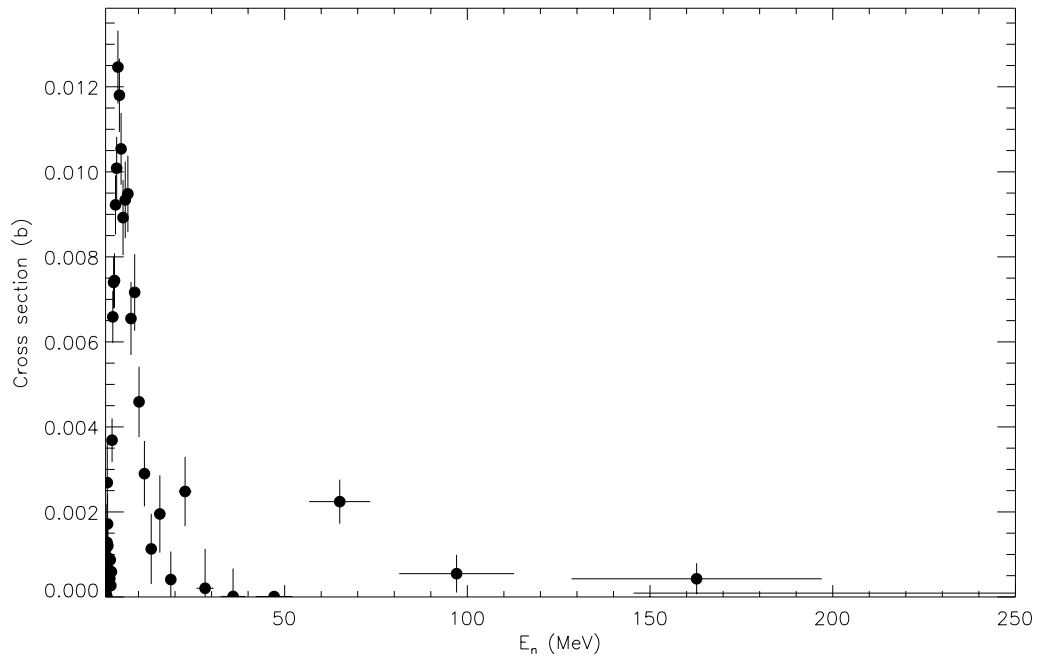


Figure B.5. Cross section for the 942 keV transition in ^{130}Te .

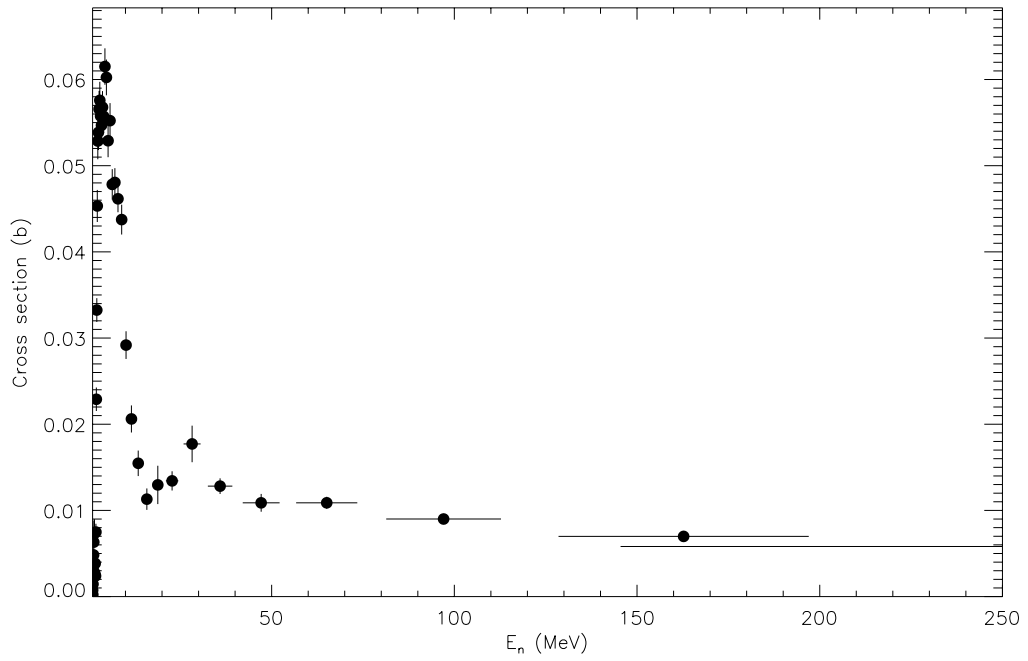


Figure B.6. Cross section for the 1046 keV transition in ^{130}Te .

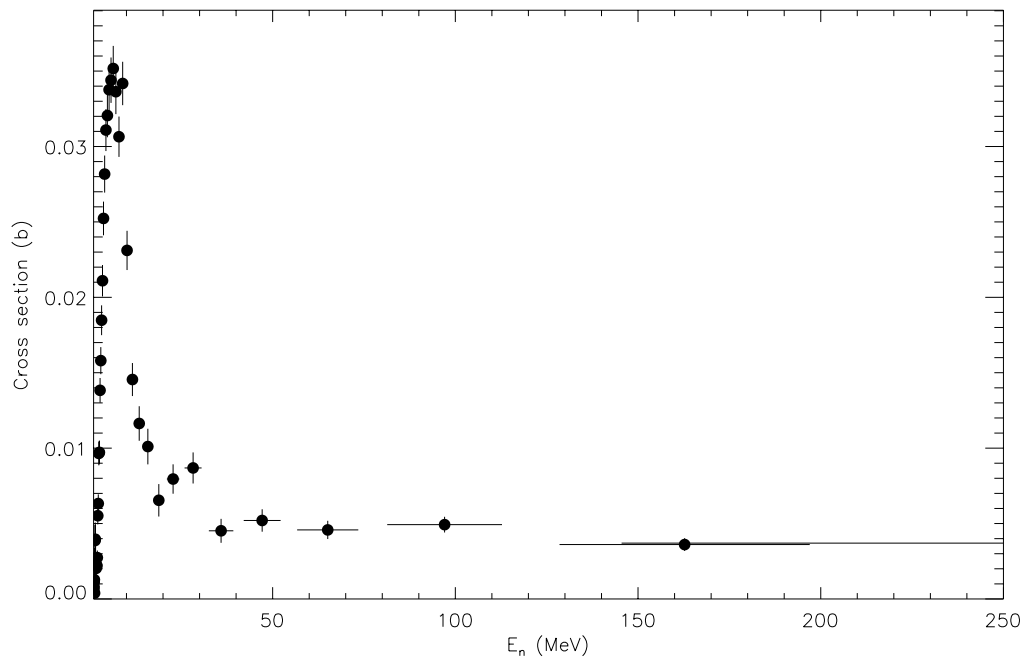


Figure B.7. Cross section for the 1142 keV transition in ^{130}Te .

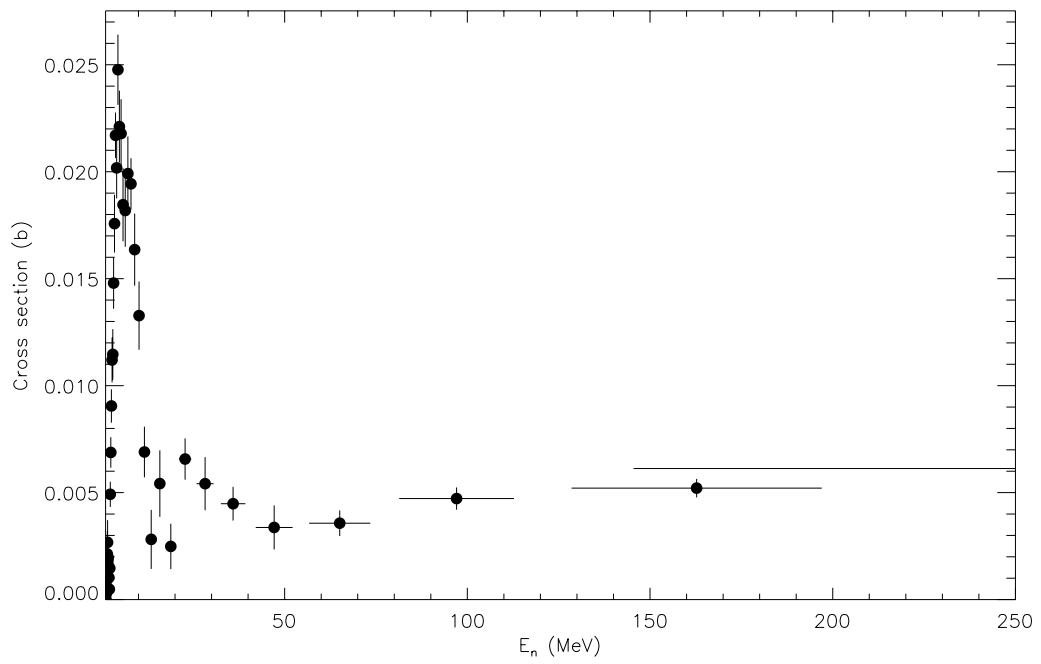


Figure B.8. Cross section for the 1299 keV transition in ^{130}Te .

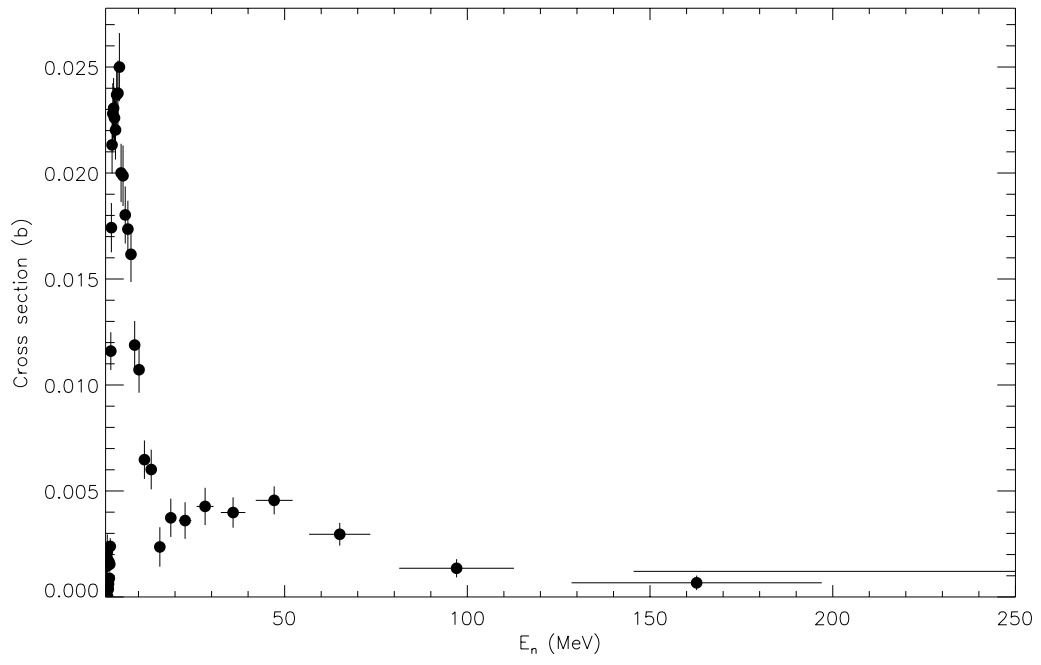


Figure B.9. Cross section for the 1443 keV transition in ^{130}Te .

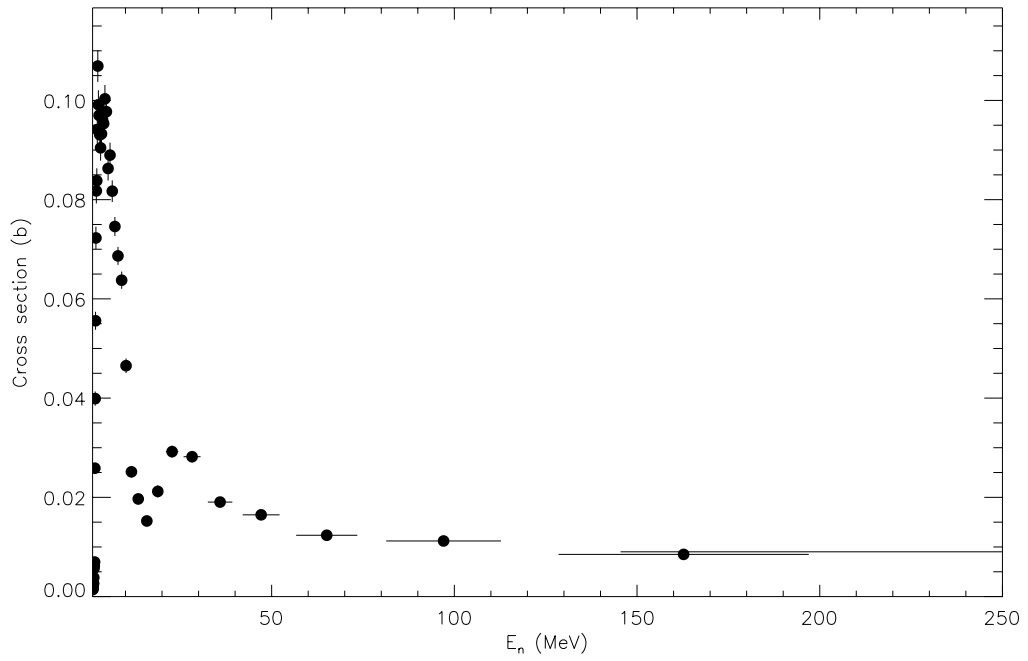


Figure B.10. Cross section for the 776 keV transition in ^{128}Te .

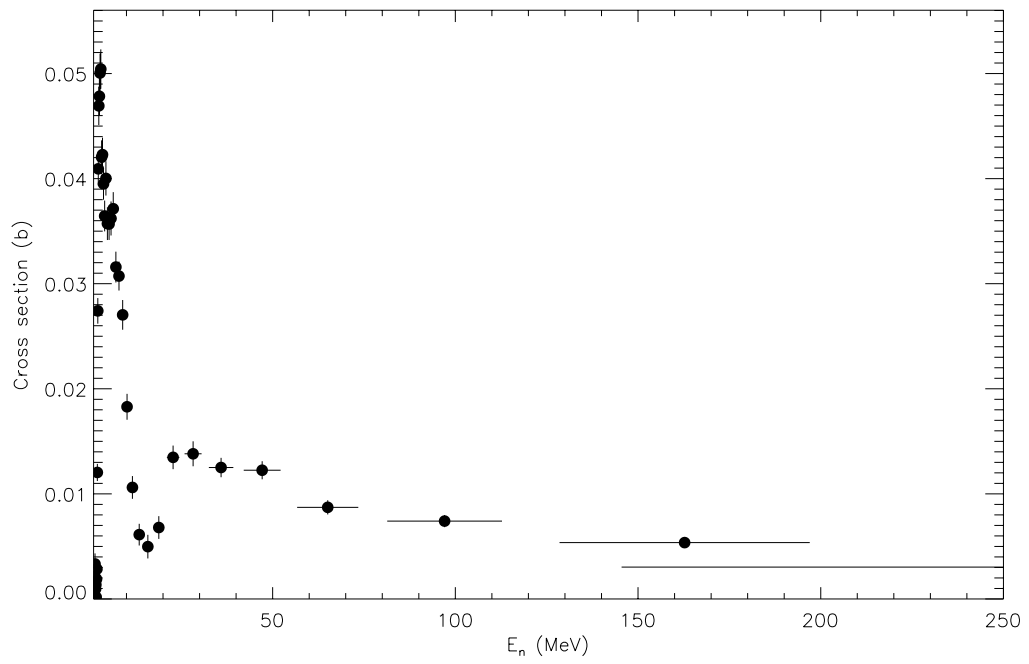


Figure B.11. Cross section for the 1225 keV transition in ^{128}Te .

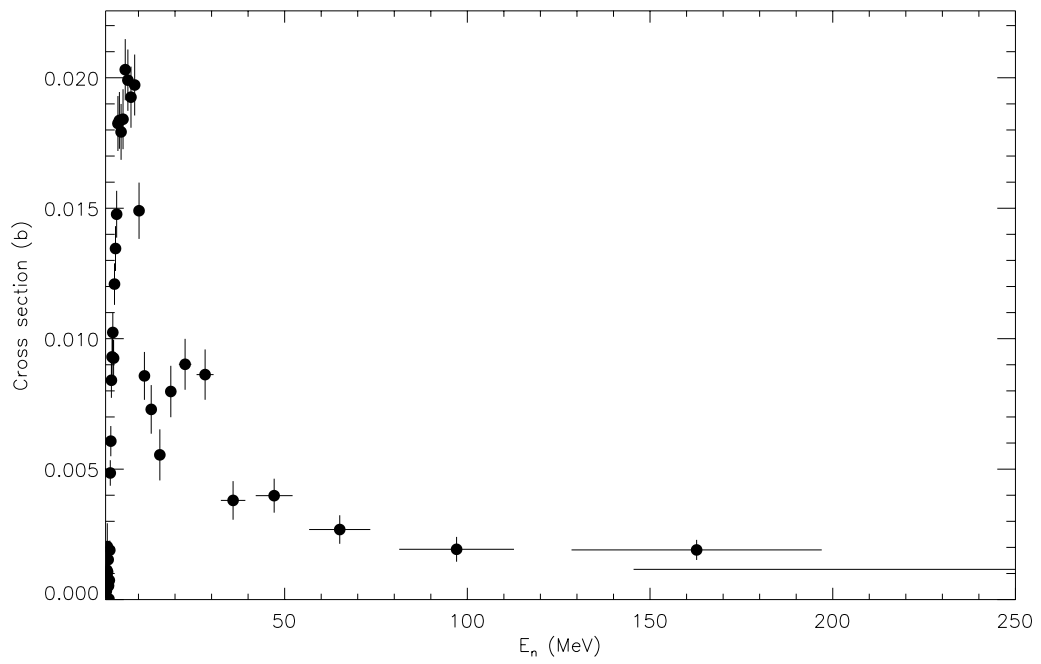


Figure B.12. Cross section for the 1284 keV transition in ^{128}Te .

B.3 ^{126}Te excitations

The excitations in figures B.13 and B.14 are produced by the $^{126}\text{Te}(n,n'\gamma)^{126}\text{Te}$, $^{128}\text{Te}(n,3n)^{126}\text{Te}$, and $^{130}\text{Te}(n,5n)^{126}\text{Te}$ reactions.

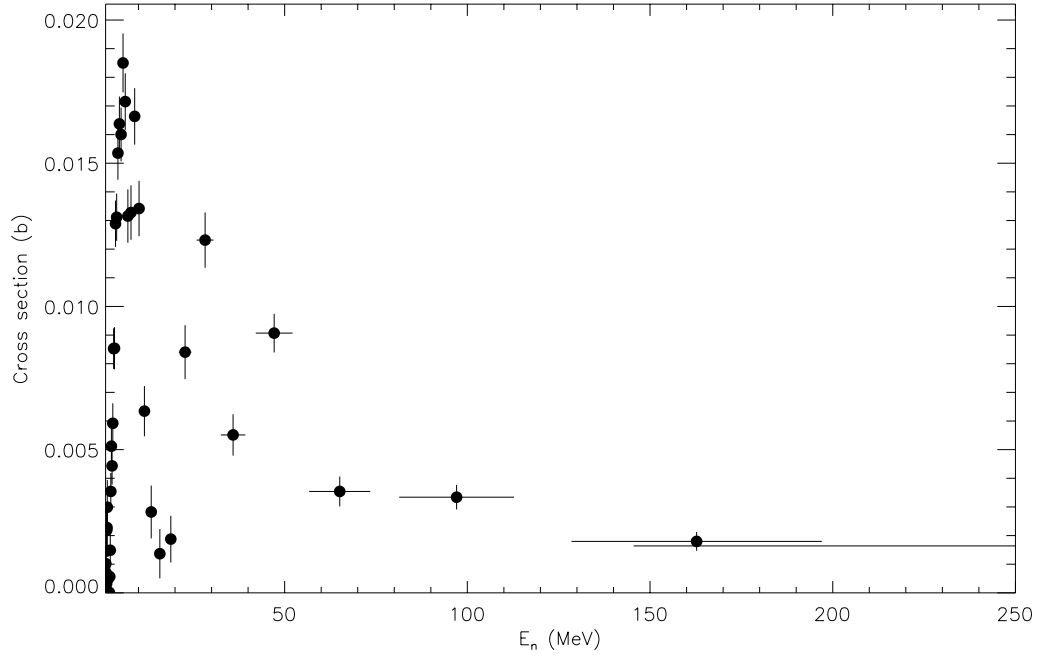


Figure B.13. Cross section for the 651 keV transition in ^{126}Te .

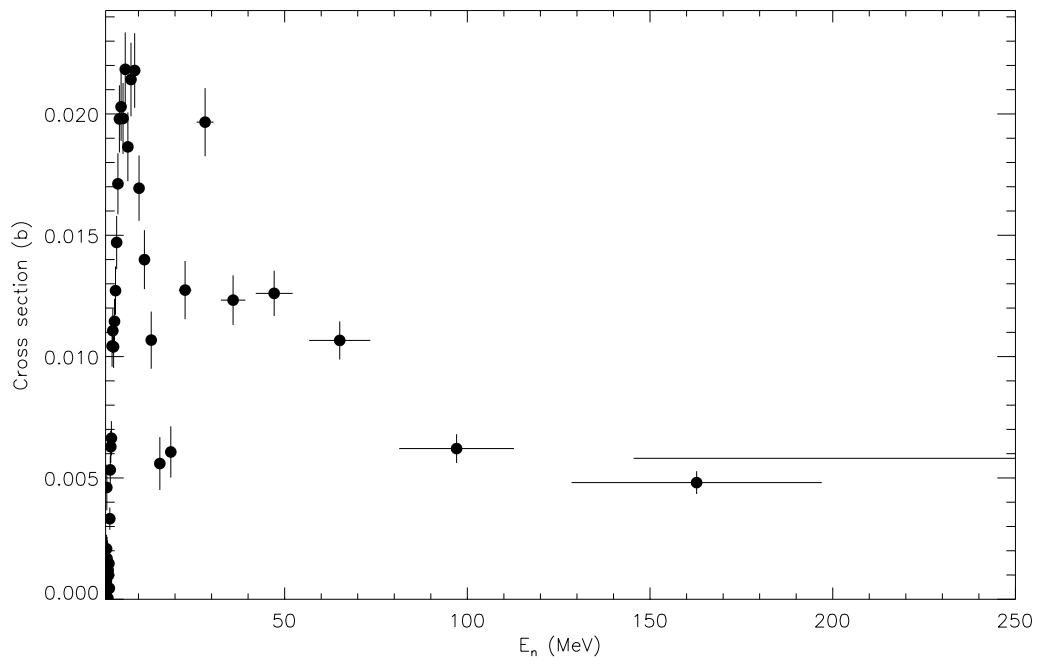


Figure B.14. Cross section for the 1346 keV transition in ^{126}Te .